Fall 2020

Acoustic and Ultrasonic Beam Focusing Through Aberrative and Attenuative Layers

Hossain Ahmed

ACOUSTIC AND ULTRASONIC BEAM FOCUSING THROUGH ABERRATIVE AND ATTENUATIVE LAYERS

By

Hossain Ahmed

Bachelor of Science
Bangladesh University of Engineering and Technology, 2004

Master of Aerospace Engineering
University of South Carolina, 2016

Submitted in Partial Fulfillment of the Requirements

For the Degree of Doctor of Philosophy in

Mechanical Engineering

College of Engineering and Computing

University of South Carolina

2020

Accepted By:

Sourav Banerjee, Major Professor

Victor Giurgiutiu, Committee Member

Austin Downey, Committee Member

Juan Caicedo, Committee Member

Susanta Ghosh, Committee Member

Cheryl L. Addy, Vice Provost and Dean of the Graduate School

DEDICATION

This dissertation is dedicated to my parents Mr. Md. Rafiqul Islam and Mrs. Skm Hasina Begum. I would also like to dedicate this work to my lovely wife Khaleda Akter and my loving children Ms. Sharrinah Irem Ahmed & Mr. Aariyd Ayan Ahmed.

ACKNOWLEDGEMENTS

I would like to thank my honorable advisor Dr. Sourav Banerjee for his cordial support and invaluable guidance and mentorship in my PhD studies. I am one of the blessed students who got this opportunity to work with a knowledgeable person like him. I would like to thank Prof. Victor Giurgiutiu, Prof. Juan Caicedo, Prof. Austin Downey and Prof. Susanta Ghosh, for being part of my Dissertation Committee and for careful review of this work. I also would like to thank all the previous and existing iMAPS members for their continuous support.

Financial support from NASA Langley Research Center, Department of Mechanical Engineering and Graduate School at the University of South Carolina are gratefully acknowledged.

Finally, I am grateful to my wife, Khaleda Akter Mukta for her sacrifice and selfless support throughout her existence in my life.

ABSTRACT

Ultrasonic nondestructive evaluation (NDE) is a well-established technique to assess material properties and material state in noninvasive way. However, conventional NDE technologies are limited by the thick top coatings over the structure and, therefore, require time consuming removal and replacement of the coatings to perform the inspection. In biological application, although ultrasonic NDE is a safer method in compared to other radioactive non-invasive techniques, aberration of acoustic beams is more common as it encounters multiple tissue layers of complex geometry with non-homogeneous properties. These limit the use of ultrasonic NDE in engineering and biological applications. To alleviate this problem, recently developed multifunctional metamaterials are studied and proposed as an ad-hoc metastructure to focus acoustic ultrasonic wave beam. One of the intriguing features of these metastructures is that it can be utilized along with conventional NDE transducers. In general, exotic acoustical features such as acoustic transparency, ultrasonic beam focusing, acoustic band gap and super lensing capabilities are extracted using metamaterial structures. While metamaterials can focus an ultrasonic beam at specific frequency, unwanted distortion of the output wave fields at neighboring sonic frequencies are obvious in the host medium. However, ultrasonic wave focusing by virtue of negative refraction and simultaneous transparency of the metamaterial at sonic frequencies are uncommon due to their frequency disparity. In this research, two metamaterial structures are proposed: 1) to

achieve acoustic beam focusing at ultrasonic frequency and keep the structure transparent to the sonic frequencies (<20 kHz)an array of butterfly-shaped thin ring resonators are proposed and 2) to achieve wave focusing and generating Bessel Beam propagation through a thick composite plate a novel high symmetry interlocking micro-structure is studied and proposed as an ad-hoc metastructure infront of the ultrasonic NDE transducers, .

1) The butterfly metamaterial with local ring resonators or butterfly crystals (BC) were previously proposed to create wide band gaps (~7 kHz) at ultrasonic frequencies above 20 kHz. However, in this research a unique sub-wavelength scale wave focusing capability of the butterfly metamaterial utilizing the negative refraction phenomenon is demonstrated, while keeping the metamaterial block transparent to the propagating wave at lower sonic frequencies below the previously reported bandgaps.
2) A novel high symmetry interlocking micro-structure is recently being investigated with optimized geometry for extracting improved mechanical properties such as high stiffness-high damping and high strength-high toughness. However, the study of elastic wave propagation through these high symmetry micro-structures is still in trivial stage. In this dissertation, the band structures, mode shapes and equifrequency contours at multiple frequencies are studied for this interlocking architecture and it was discovered that at specific ultrasonic frequency wave focusing and generating Bessel Beams are possible. Through modal analysis such phenomena are physically explained. The finite element simulations are performed for long distance wave propagation and the results are post-processed

to show the actual existence of Bessel Beam phenomenon at ultrasonic frequency ~271 kHz. A concluding simulation is performed using ad-hoc interlocking metastructure to propagate wave through a combination of attenuating epoxy and composite plate. Full penetration of wave inside thick composite plate is clearly observed.

To visualize the wave propagation in engineered materials, like composites and metastructures, a reliable but fast wave simulation tool is required. Wave propagation in Metastructure in conjunction with attenuative composite structure or aberrative biological surfaces, is difficult to accomplish. Traditional approach uses Finite Element Method (FEM) which is consistently known to be difficult at higher ultrasonic frequencies due to spurious reflection at element boundaries. Hence, to reduce the number of elements in the structure a new simulation tool using spectral information is necessary. In this dissertation, a computational tool based on higher order Spectral Element Method is developed from scratch to solve temporal wave propagation problem in three-dimensional composite structures. This tool will facilitate to understand the wave damage interaction and optimize the geometric dimensions to construct the metastructure in later times. There are multiple computational tools available now-a-days to simulate wave propagation problems. Among others, Distributed Point Source Method (DPSM), Finite Element Method (FEM), Semi Analytical Finite Element (SAFE), Local Interaction Simulation Approach (LISA), Peri-Elastodynamic (PED) are few of them. DPSM is frequency domain based computational tool which is unable to solve temporal problem proposed in this research. PED is suitable to solve wave propagation in metallic structure; however, it has not yet been implemented in composite structures. Although FEM is a

flexible method to implement for complex geometries, spurious reflection, lower accuracy and higher computational time make it less effective. To overcome the disadvantages encountered by FEM, Spectral Element Method (SEM) is recently proposed for its higher accuracy and fast convergence. Therefore, in this dissertation, SEM has been proposed to visualize high frequency ultrasonic wave in a range of 1 MHz to 7.5 MHz, which is not available in current literature. Various modules of the computer code using MATLAB are developed and simulation was performed for wave propagation through a 24-ply laminated composite plate. The simulation results were compared with experimental observations, and a good agreement of simulation and experiment was observed.

TABLE OF CONTENTS

LIST OF TABLES

LIST OF FIGURES

List of Symbols

λ	Wavelength
ρ	Density
E	Young's Modulus
υ	Poisson's Ratio
Π_p	Potential Energy
ψ_Ω	Volume Force Vector
ψ_Γ	Surface Force Vector
$\mathbb{C}^e$	Constitutive Property Matrix of an Element
σ_{ij}	Stress
ξ	Nondimensional coordinate in direction 1
ω	Weight factor

List of Abbreviations

BC ..... Butterfly Crystals

BZ ..... Brillouin Zone

CFRP ..... Carbon Fiber Reinforced Polimer

ESED ..... Elastic Strain Energy Density

FEM ..... Finite Element Method

FFT ..... Fast Fourier Transformation

NDE ..... Non-Destructive Evaluation

NDT ..... Non-Destructive Testing

PC ..... Phononic Crystals

PE ..... Pulse Echo

PMMA ..... PolyMethyl Methacrylate

SHM ..... Structural Health Monitoring

UT ..... Ultrasonic Transducer

CHAPTER 1

INTRODUCTION

1.1 PROBLEM STATEMENT

Ultrasonic Non-Destructive Testing (NDT) is a technique of evaluating the physical properties such as fracture toughness, ductility, ultimate tensile strength, impact resistance, ductility etc. of structural components. It is also a well-established method to use high frequency acoustic waves to detect and evaluate flaws or damages, measure dimensions and characterize materials in noninvasive way. As a driving NDT technology, the ultrasonic nondestructive evaluation (NDE) has become a powerful tool to use extensively in metal processing, manufacturing, oil and gas, aerospace and defense industries. Along with metals and alloys, the ultrasonic NDE has been successfully utilized in concrete, wood and composite structures, making it serviceable in the construction industry. The expansion of automobile industry and stringent safety regulations in structural health monitoring (SHM) for multiple industrial applications such as aerospace, civil and defense are playing a vital role for the growth of NDE applications. Exponential rise in urbanization and emergence of industrial revolution 4.0 have generated massive demand for advanced technology in various research disciplines which is one of the leading factors to the expansion of ultrasonic NDE market on the global scale.

To support these huge applications, a large group of researchers has been working for decades to improve these techniques. In the core of ultrasonic research, ultrasound waves are distributed in the material or object to be tested noninvasively. In a more common ultrasonic testing applications, short ultrasonic waves that have center frequencies in the range of 0.1 to 15 MHz, and in some cases up to 50 MHz, are transmitted into objects or materials to characterize materials or detect internal defects or flaws. The ultrasonic energy transmitted through and reflected from a defect contain a considerable information about the nature of the spread of the flaws or damage. Post-processing of these transmitted and/or reflected energy information are utilized to evaluate the material state condition.

One of the limitations of the current ultrasonic NDE technology is the inability to inspect composite substrates with inherent curvature located below attenuative topcoats with thicknesses ranging from 0.15-0.30 inches. Conventional NDE technologies are limited by the thick top coatings over the structure and therefore require time consuming removal and replacement of the coatings to perform these inspections. While the coatings of interest are highly attenuative to ultrasound, it is the most effective and safe NDE method with the desired resolution for damage detection, and it has always been a preferred method over others such as microwave and THz wave. However, the dissipation/attenuation of ultrasound waves and the aberration of focused ultrasound through the coated layer makes ultrasound ineffective to inspect composites below the topcoats without removing them. Additionally, ultrasound inspection through curved surfaces are also challenging using the flat head ultrasound transducers. Hence, a

significant opportunity exists to address this challenge while proposing a novel NDE solution to inspect the structures through the coating layer without removing them.

In biological applications, ultrasound NDE has been proven as a safer method to assess internal parts of a human body in compared to existing other techniques such as x-ray, MRI and CT scans. However, when using ultrasound in biomedical engineering applications, acoustic beams encounter multiple tissue layers of complex geometry with non-homogeneous properties. For instance, an accurate control of the focused beam is at the basis of focused ultrasound therapy techniques, e.g., as in high intensity focused ultrasound hyperthermia, thermal ablation or histotripsy, or in extracorporeal shockwave lithotripsy [1, 2]. Focusing directly into human soft tissues can efficiently be achieved by using conventional systems as ultrasound beam aberrations are typically small in these media [3]. However, when the target tissue lays behind high-impedance tissues, e.g., soft-tissue surrounded by bones, the beam experiences strong aberrations due to refraction, reflection and absorption processes [4]. Some applications make the use of existing acoustic windows by targeting tissues from specific locations. Nevertheless, in the case of transcranial propagation, skull bones are always present in the path towards the central nervous system (CNS). In this way, the precise control of acoustic focus into the CNS is mainly limited due to the strong phase aberrations produced by the refraction and attenuation of the skull [5]. Therefore, propagation of ultrasonic wave beam through aberrative biological surfaces remains a challenge for the researchers.

1.2 BACKGROUND

Despite the presence of attenuative and aberrative surfaces, many industries rely on ultrasonic NDE to assess structural integrity and evaluate structural health. The aerospace industry especially commercial aircraft operators and military aircraft operators follows stringent regulations imposed by the respective aviation authorities for the safety and reliability of the passengers and the aerospace products. In defense such as U.S. Air Force strives to maintain a very high operational availability of aircraft and has an ongoing need to reduce total ownership costs, increase reliability, and extend the lifecycle of equipment and systems to improve overall readiness of the fleet. The costs of inspection and maintenance for Air Force aviation alone increases every year and currently costs more than $24 billion per year [6]. Much of this cost is due to scheduled maintenance activities, which often require the removal of paint and coatings from an aircraft, or the complete disassembly of component parts for inspection. The current standard practice used during maintenance activities involve the complete stripping of an aircraft coating system to inspect the outer skin of the aircraft. These maintenance procedures are currently required to inspect for hidden damage that could compromise the structural integrity of the aircraft if left unchecked. Several studies have been conducted to evaluate the nondestructive inspection techniques to provide thru-coating inspection, to varying degrees of success. Except for the ultrasonic method, none of these techniques provided satisfactory results, and all are unacceptable to some degree.

Paints and coatings perform vital roles in protecting fuselage, wings, and other aircraft structures. In addition to aesthetics, image, and camouflage, there are several technical reasons for painting both metal and composite structures. For metals, coatings

help protect the structure from corrosion. For composites, the coatings primarily protect the structure from fluid damage, but are also sometimes needed for RF/EM shielding and lightning strike protection. Due to high strength-to-weight and stiffness-to-weight ratios, composite structures have seen a substantial increase of their use in the new generation of airplanes, where the entire fuselage and the wing structures are made of composites. But composite structures are susceptible to impact damage caused by hail, bird strikes, or accidental tool drops. The damage may be delamination, fiber breakage, and/or matrix cracking, or a combination of all the above. In addition, the damage may not be visible on the outer surface, and the thick topcoat limits the effectiveness of conventional nondestructive evaluation technologies to detect the damage. Therefore, the coatings are removed to perform the inspection and then reapplied afterwards. This process is prohibitively time consuming and increases inspection and/or maintenance downtime by up to 1000 times. Eliminating the need to remove the coatings would enable capabilities for long-life coating systems and condition-based maintenance practices resulting in significant reductions in hazardous waste generation, dramatic cost savings, and enhanced readiness levels for a wide variety of Air Force systems.

In 2007, Army Research Laboratory (ARL) studied the efficacy of performing fluorescent penetrant inspection (FPI) and magnetic particle inspection (MPI) over coatings to detect cracks in metal substrates [7]. ARL found that performing FPI of cracks over a coating proved futile. There existed no path for the penetrant to infiltrate and collect within the cracks, and the paint absorbed a great deal of penetrant, which led to high background fluorescence. Similarly, one layer of coating greatly reduced the effectiveness of MPI, and two layers completely masked the cracks. Air Force Research

Laboratory (AFRL) assessed various NDE methods for detecting hidden damage on metal substrates through thin (0.003-inch-thick) aircraft coating systems [8]. Example of these NDE methods are immersion ultrasound, laser ultrasound, passive thermography, film radiography and evanescent microwave NDE. In all cases, the major effect of the coatings was to add noise to the NDE measurement, which affects detection sensitivity levels. But all were still able to detect underlying damage on the metal substrate, albeit through a very thin coating (0.003-inch-thick), and also there were issues with thicker coatings and inspecting through specialized coatings.

1.3 Research Objectives

The key objective of this research is to develop an NDE technique to inspect graphite/epoxy composite substrates through thick specialty topcoats which is a major challenge in current ultrasonic NDE. There are many NDE methods used to inspect composite materials, including ultrasound, X-ray, thermography, and relatively new terahertz (THz) radiation technology [9]. THz radiation shows promising results for glass-fiber composites but has limited viability for graphite-epoxy composites because the conductive carbon fibers prevent penetration of the THz radiation [9]. Nevertheless, none of these NDE methods can currently inspect through the thick specialty coatings. Of all the currently used techniques, ultrasonic inspection is rated as the best overall evaluation method to detect various types of composite damages. Therefore, ultrasonic inspection would be a viable candidate, however, the coatings are highly attenuative to conventional ultrasound waves.

In attenuative and/or aberrative surfaces, gradual spatial spreading of the ultrasonic signals is generally caused by diffraction of the ultrasonic waves in the material. Dispersion of the wave happens due to the combined effect of structural and material properties, and manifests by temporal spreading of the ultrasonic wave signals. When the amplitude of the signal reduces over a length of the propagation distance, the signals are said to be attenuated. The ultrasonic stress wave partially converts its energy into heat, and it loses its amplitude. Hence, to avoid the above situations, acoustic energy needs to be concentrated or focused at a certain depth which will be suitable for ultrasonic NDE of composites underneath the coating layer and/or biological aberrative surface. Alternatively, an acoustic ultrasonic wave needs to be generated which is capable to propagate long distance with negligible amplitude attenuation. One solution could be to generate ultrasonic Bessel Beam which will not diffract or spread out as it propagates over a long distance. Such Bessel Beam can be utilized to penetrate through the attenuative coating layer and the composite structure.

1.4 Solution Approaches

NDE of composite substrates underneath a coating layer or through a biological aberrative layers is a persistent problem, which many researchers have attempted to address through various techniques. Till today, it remains a challenging problem without a viable solution. Although ultrasonic NDE, being the most effective noninvasive inspection method, is used for most cases to perform NDE of composites, it requires removal of the topcoat to penetrate deep inside the composite. Moreover, in biological applications, the aberrative nature of the skulls, bones and soft tissue surrounded by the bones makes ultrasonic NDE less effective. Hence, although ultrasound is a valuable

NDE method, it suffers from diffraction, dispersions and attenuation through the coating layers and aberrative surfaces. Therefore, a technique needs to be developed for ultrasound waves to pass through the topcoat and/or aberrative surfaces and focus or propagate the wave inside the composite. This will eliminate the need for the removal of the coating layer.

To solve this problem, we are proposing two approaches in this research work. In the first approach, (1) we are proposing to adopt a metastructure in front of the traditional transducer to focus ultrasonic waves. Because of the exotic nature of the added structure, wave propagation inside the combined structure will be unknown. Hence, to visualize the unknown wave propagation behavior in the metastructure and the host substrate, in the second approach, (2) we are proposing to select Spectral Element Method (SEM) as a wave propagation computational tool for a frequency range up to 7.5 MHz.

THE FIRST APPROACH

In the first approach, two metamaterial structures are proposed. The reason behind proposing these two metamaterials are stated below.

(1) The first metamaterial is proposed to understand and achieve acoustic beam focusing at ultrasonic frequency and keep the structure transparent to the sonic frequencies (<20 kHz). In designing this acoustic metamaterial, a butterfly shaped engineered metamaterial consists of an array of stainless steel split ring resonators of different sizes embedded in epoxy matrix [10] is envisioned for the wave modulations. This structure has been analyzed for multifunctional design objectives. Just by manipulating one meta structure orientation and number of unit

cells, the proposed butterfly structure can induce multiple acoustic features such as band gap, acoustic transparency, wave focusing and superlensing. To achieve the acoustic features and create the dependencies at multiple frequencies, individual split resonators that creates the local anisotropy at multiple scales is introduced in a butterfly shape. The shape and the orientation of the proposed model are purposefully designed for acoustic wave bifurcation and focusing of the wave field, when the geometrical configurations (e.g. ring thickness) and the number of repeating unit cells are constructed for low frequency acoustic transparency. One of the intriguing properties of the proposed structure is the negative refraction which has been analyzed and utilized to extract the behavior of acoustic lens.

(2) The second metamaterial, a novel high symmetry interlocking micro-structure, is studied and proposed as an ad-hoc metastructure infront of the ultrasonic NDE transducers to achieve wave focusing and generating Bessel Beam propagation through a thick composite plate. Initially, an interlocking micro-architecture design was reported for the extraction of improved mechanical properties. The acoustic responses of this micro-structure show the existence of band gap and near isotropic behavior which are suitable for wave trapping and attenuation. Recently, this structure is being investigated with optimized geometry for extracting improved mechanical properties such as high stiffness-high damping and high strength-high toughness. The optimized metastructure, which is proposed in this research, has the capability to focus ultrasonic wave and to

generate Bessel Beam where the amplitude of the propagating wave does not diffract or spread out as it propagates through a long distance.

THE SECOND APPROACH

In second approach, we intend to develop a computational tool that can effectively solve wave propagation problem when multiple interphase layers are combined. This computational tool will visualize the wave propagation behavior when the ad-hoc metastructure is present in between traditional transducer and coated composite structure or biological aberrative surfaces. In later times, this tool will provide an understanding how propagating wave interacts with the defects present in coated composite or assess the biological parts at normal and abnormal conditions. Moreover, practical construction of metastructures and/or transducers to propagate ultrasonic waves through coated composite structures requires optimization of geometry parameters which can be determined by utilizing this computational tool. To simulate wave propagation problems, there are multiple computational tools available now-a-days. Distributed Point Source Method (DPSM), Finite Element Method (FEM), Semi Analytical Finite Element (SAFE), Local Interaction Simulation Approach (LISA), Peri-Elastodynamic (PED) are few of them. However, each of the methods has its disadvantages. For example, DPSM is frequency domain based computational tool which is unable to solve temporal problem proposed in this research. PED is suitable to solve wave propagation in metallic structure; however, it has not yet been implemented in composite structures. Although FEM is a powerful method, spurious reflection, lower accuracy and high computational time make it less effective. To overcome the disadvantages of these techniques, we are proposing a recently developed computational technique, Spectral Element Method (SEM), for its

higher accuracy and fast convergence. The developed tool will simulate wave propagation in non-coated laminated composite with a frequency range of 1MHz to 7.5 MHz. Further, it will also simulate wave propagation in coated-composite along with the ad-hoc metastructure that has been proposed in the first approach. The experimental validation of simulation results is proposed with 1 MHz to 7.5 MHz transducers with and without coated-composite substrate.

1.5 Dissertation Outline

This research demonstrates design of two acoustic metamaterials capable of focusing acoustic energy and generating Bessel Beam. It also presents a computational tool to facilitate wave propagation inside multilayered composite structure. Moreover, an experimental validation of the results obtained by the computational tool is demonstrated herein. This dissertation is organized as follows:

Chapter 1: Explains the problem and the objectives of this study. The approaches adopted to achieve these objectives with the inherent motivations are outlined in this chapter.

Chapter 2: Butterfly structured acoustic metamaterial design and the demonstration of acoustic focusing phenomenon is presented. An exotic acoustic feature, negative refraction, has been designed and analyzed with band structure, mode shape and transmission coefficients.

Chapter 3: Investigation of high symmetry interlocked structured metamaterial is presented here to demonstrate the wave trapping and attenuation behavior by utilizing modal analysis and wave transmissibility.

Chapter 4: Investigation and integration of optimized interlock structured metamaterial as an ad-hoc metastructure is demonstrated here. Wave focusing and generation of Bessel Beam are utilized to propagate wave through a combination of attenuating epoxy and composite structure.

Chapter 5: A fundamental difference between FEM and SEM, and applicability of SEM in wave propagation problem are presented in this chapter. Wave propagation in multilayered composite specimen has been formulated in 3D and a simulation of displacement behavior is presented by varying input parameters.

Chapter 6: Implementation of Spectral Element Method to solve wave propagation in multilayered composite structure has discussed in this chapter. Simulation results with computer code has been presented, and an experimental validation of the simulation results are discussed herein.

Chapter 7: Summarizes the work presented in this dissertation and outlines a scope of future works.

CHAPTER 2

A MULTI-MODE ACOUSTIC METAMATERIAL ARCHITECTURE FOR EXTRACTING ACOUSTIC TRANSPARENCY, WAVE FOCUSING AND SUPERLENSING BEHAVIOR

2.1 ABSTRACT

Exotic acoustical features such as acoustic transparency, ultrasonic beam focusing, acoustic band gap and super lensing capability using a single metamaterial architecture is unconventional and unprecedented in the literature, demonstrated herein. While metamaterials can focus an ultrasonic beam at specific frequency, unwanted distortion of the output wave fields at neighboring sonic frequencies are obvious in the host medium. However, ultrasonic wave focusing by virtue of negative refraction and simultaneous transparency of the metamaterial at sonic frequencies are uncommon due to their frequency disparity. To circumvent this problem and to avoid the unwanted distortion of wave at sonic frequencies, metamaterial with an array of butterfly-shaped thin ring resonators are proposed to achieve the beam focusing at ultrasonic frequency (37.3 kHz) and keep the structure transparent to the sonic frequencies (<20 kHz), while resulting local anisotropic material behavior. The butterfly metamaterial with local ring resonators or butterfly crystals (BC) were previously proposed to create wide band gaps (~7 kHz) at ultrasonic frequencies above 20 kHz. However, in this study a unique sub-wavelength scale wave focusing capability of the butterfly metamaterial utilizing the

negative refraction phenomenon is demonstrated, while keeping the metamaterial block transparent to the propagating wave at lower sonic frequencies below the previously reported bandgaps.

2.2 Introduction

The last two decades have witnessed unique and careful design of several artificially engineered composite materials called metamaterials. The composite metamaterials are envisioned for various practical applications to manipulate the acoustic waves [11-19] in a unique way. Periodic structures both in photonics and phononics, are capable of significantly alter the wave propagation phenomena in the host media. Thus it inspired a large group of researchers to realize several mechanisms for wave front modulation [20-23] using the periodic structures. However, most of the research were performed to manipulate the acoustical waves at specific and/or predefined frequencies [24, 25]. The presence of periodic metamaterial structures not only generates unique feature at the designed frequency, it also alters the wave fields inside and outside the metamaterial at off-designed frequencies (outside the band of specific designed frequency), in an unintended/uncontrolled way. Eventually, this limits the application of the metamaterials for wide frequency applications.

To solve this issue, here in this article it is proposed that the periodic structures need to be designed in such a way that the metamaterial system should not affect the propagating wave field until the designed frequency is reached. That means that the metamaterial system should behave as a acoustically transparent media, except at the desired frequency at which it is expected to behave as metamaterial and demonstrate a

specific designed phenomenon. The range of frequencies where the incident waves can transmit without any distortion can be called 'Acoustically Transparent Range'.

On the other hand, the possibilities of focusing the elastic waves through metamaterials, led the researchers to design acoustic phononic [26] lenses embedding intricate geometrical variations in host materials. Similar approaches were also adopted for photonic lenses [27, 28] in electromagnetic applications. Many researchers have successfully demonstrated the acoustic flat lenses using phononic crystals in a periodic fashion. Fascinating wave propagation phenomena such as single and double negative refraction [29], orthogonal wave transportation [17], non-diffracting Bessel beam [30], sub-wavelength scale wave focusing [30] and multiple wave scattering etc., were demonstrated by various periodic structures. Recently, a topologically optimized [31] two-dimensional acoustic lens was successfully implemented in underwater imaging. While the applications of these metamaterials are fully realized, acoustic wave focusing may have larger impact with ultrasonic frequencies in biomedical imaging and surgery [32]. It is established that the resolution of the conventional flat lens is limited by its diffraction limit due to the diminishing evanescent component of the propagating waves [33]. Hence, the possibility of achieving the subwavelength information is a topic of interest, if can be achieved by the metamaterials. So far, one of the promising method that has been proposed is to utilize the negative refraction property of the meta structures with constituent phononic crystals to construct the Super-lenses [34]. Although the concept of Super-lenses was first coined in photonics, it is now also exploited in acoustical studies.

In this chapter, a butterfly shaped engineered metamaterial consists of an array of stainless steel split ring resonators of different sizes embedded in epoxy matrix [10] is

envisioned for the wave modulations discussed above. Just by using one meta structure orientation, Butterfly metamaterial is proposed to simultaneously demonstrate multiple acoustic features such as acoustic transparency, wave focusing and superlensing at respective different frequencies. To achieve the acoustic features and create the dependencies at multiple frequencies, individual split resonators that creates the local anisotropy at multiple scales is introduced in a butterfly shape. To achieve the transparency at lower frequencies it is necessary to have near isotropic behavior of the meta structure in global scale whereas, to achieve other phenomena discussed above can be achieved by creating the local anisotropy. Hence, the shape and the orientation of the proposed model are purposefully designed for acoustic wave bifurcation and focusing of the wave field, when the geometrical configurations (e.g. ring thickness) and the number of repeating unit cells are constructed for low frequency acoustic transparency. Furthermore, the presence of wave focusing capability dictates the negative refraction property of the structure which resulted superlensing phenomenon.

This chapter is divided into four sections. Initially, eigenfrequency analysis is performed to identify the dispersion behavior of the proposed butterfly structure within the first Brillouin zone. In section two, a frequency domain study is performed to validate the simulated configuration. As no wave should pass through the bandgaps, a material block constructed with butterfly structure shows that indeed the wave was totally blocked at the band gap frequencies. Also, acoustic transparency behavior of the proposed structure and a frequency domain study below ~18 kHz are demonstrated in this section. In section three, the modal behaviors around ~37 kHz was identified and a possible wave bifurcation and wave focusing capabilities are predicted in the structure. A frequency

domain study is performed to confirm the wave focusing phenomenon, and subsequently the range of focusing frequencies are identified. The last section of this article identifies the negative refraction phenomenon and the superlensing capability of the proposed butterfly structure.

2.3 Dispersion Curve of The Butterfly Structure

Since the mode shapes and the respective group velocities are crucial parameters to understand the wave propagation through a structure, a dispersion relation for the proposed unit cell (Figure 2.1a) is obtained by performing an eigenfrequency analysis of the structure proposed. The geometric dimensions and the material specifications reported in reference [10] are used in this article and are summarized in table 2.1.

Table 2.1. Geometric dimensions and material properties.

Component Name	Outer Dimension (mm)	Material
M1	Diameter – 5.387	Epoxy E = 2.35 GPa ρ = 1110 kg / m^3 ν = 0.38
M2	Major Radius – 10.2 Minor Radius – 5.08	
M3	2 X 2 Square	
R1	Diameter – 3.591	Stainless Steel E = 205 GPa ρ = 7850 kg/m^3 ν = 0.28
R2, R3	Diameter – 7.183	
R4	Major Radius – 11.05 Minor Radius – 5.969	

One of the objectives of selecting this unique butterfly structure is the presence of local geometric anisotropy at the material level and geometry level as shown in Figure 2.1(b) but possess the near isotropic behavior at the global scale. While performing the eigenfrequency study, a rectangular periodicity of the unit cell is assumed. Using Comsol

Multiphysics V4.3 software, the dispersion relation is obtained by performing eigenfrequency analysis for different wave vector directions. The dispersion band structure shown in Figure 2.1(c) is computed for the MΓXM boundary of the first Brillouin zone [35] (ref Fig 2.1(d)) using the Bloch-Floquet periodic boundary condition [36].

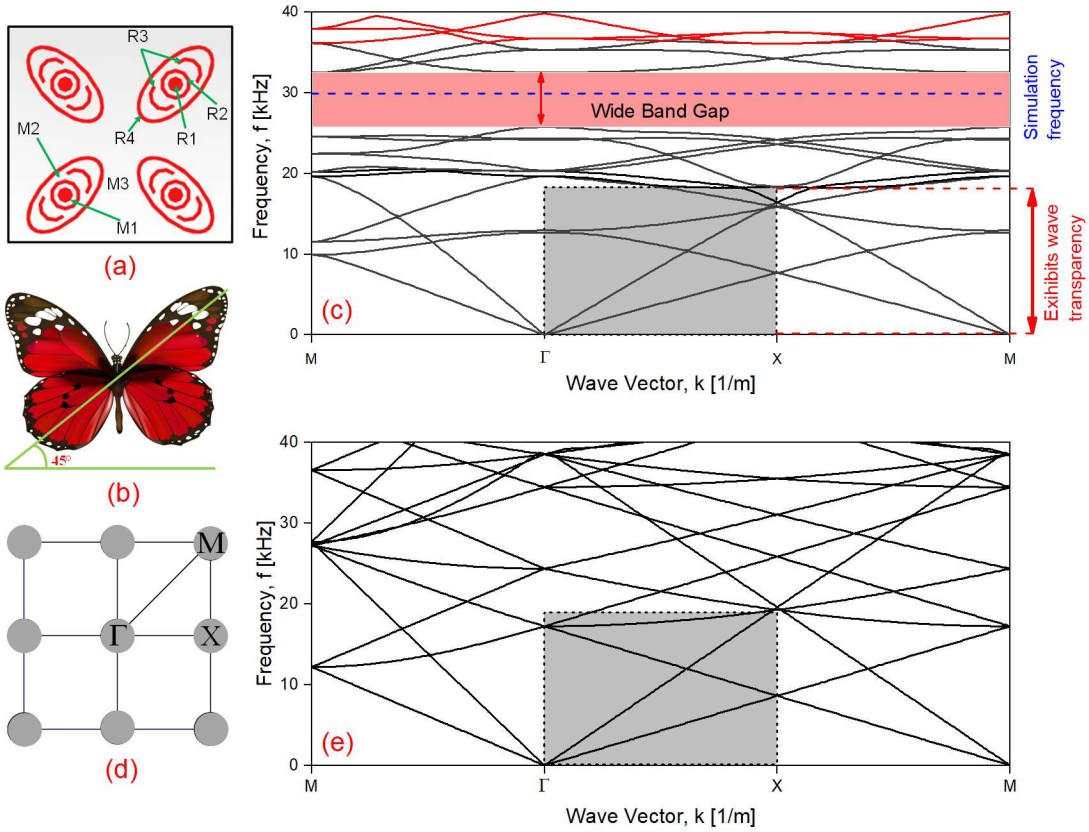

Figure 2.1: Dispersion relationship of the proposed butterfly design and the epoxy base material; (a) proposed unit cell consisting of steel-balls and elliptical steel rings in Epoxy, (b) the idea of anisotropic butterfly structure, (c) Dispersion relation of the

While investigating the Figure 2.1(c), a large band gap from ~26 kHz to ~32 kHz was evident which is also reported previously in reference [10] . A further investigation

of the Figure 2.1(c) reveals the near linear dispersion (frequency vs normalized wave vector) relation below ~18 kHz, irrespective of ΓX (dashed window) or XM directions. This demonstrates the near isotropic behavior which is found in classical bulk isotropic materials [37]. Applying similar Bloch-Floquet periodic boundary condition on the base Epoxy material (i.e. without the butterfly constituents), dispersion relation was computed at the MΓXM boundary of the first Brillouin zone (Figure 2.1(e)). Upon comparing the dispersion relation in ΓX (dashed window) or XM direction for both the butterfly structure and the base Epoxy material, it is evident that both geometries have similar dispersion behavior. Hence an infinitely repeated butterfly unit cell placed in a 2D epoxy medium can act as a single isotropic material, and the presence of these unit cells will almost be unrealized below the ~18 KHz. Since the linear dispersion behavior is an indicative of spherical wave fronts in isotropic materials, it can be assumed that the proposed butterfly structure will disperse the transmitted waves linearly and will result nearly undisturbed wave fronts below ~18 KHz. As a result, the proposed structure will be acoustically transparent within this frequency range.

2.4 Simulation Setup to Prove The 'Acoustic Transparency'

To concrete the possibility of introducing 'Acoustic Transparency' using the proposed butterfly metamaterial model, a frequency domain simulation is performed. However, to verify the simulation model, initially a frequency domain study is performed choosing an arbitrary frequency from the bandgap region. Since incident plane waves from any direction do not propagate through the material made of butterfly shaped crystals (BC) at the band gap frequencies, a frequency domain study should reveal this phenomenon and would simultaneously verify the accuracy of the model. To achieve this

objective, a 112 mm x 100 mm epoxy plate is modeled using COMSOL Multiphysics V4.3. A butterfly crystal (BC) region, designed by an array of unitary cells identical to the one considered in Figure 1(a), is placed in the base plate. In particular, the BC arrangement consists of 22 rows and 6 columns of butterfly unit cells. A plane wave front is generated by the periodic displacement of a rectangular source with a dimension of 127x12.7 mm^2. A perfectly matched layer boundary condition is considered at all the boundaries of the base plate domain to approximate negligible wave reflection from all the edges. Figure 2.3(a) shows the geometric configuration of the setup before the rectangular exciter are actuated. Figure 2.3(b) shows the simulation outcome performed between the frequency ranges ~26 kHz to ~32 kHz (only one frequency at 30 KHz in shown in the Figure 2.3(b)). It is clearly evident that no displacement is observed neither at the BC nor at the Epoxy and the host material on the right. This confirms that no wave is transmitted through the BC within the band gap region.

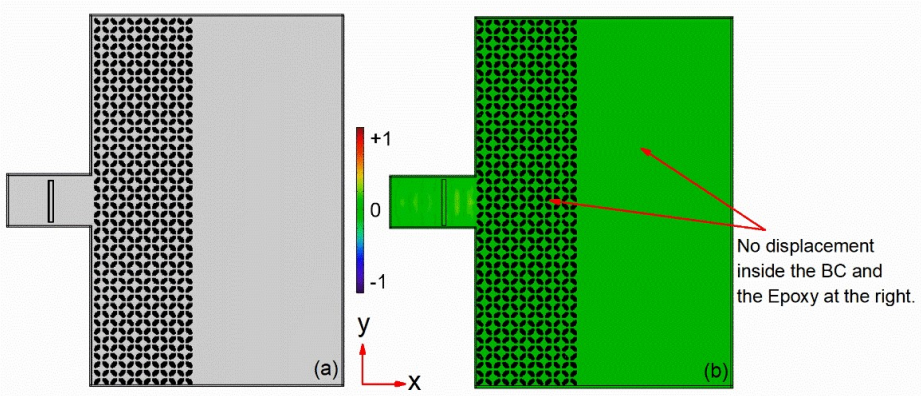

Figure 2.2: (a) Geometric configuration without excitation, (b) Simulation of wave field at a frequency from the band gap at a frequency of 30 kHz.

Next, to demonstrate the acoustic transparency, plane crested wave is generated at the audible frequency range in Γ-X direction (along x-direction). Additionally, the unit

cells made of base Epoxy material having the butterfly structure is considered. Simulation was performed between 0 and ~20 kHz frequency within the audible frequency range. Results of these two simulations are presented in Figure 2.3 to have a visible comparison between the wave fields generated in the base material with and without the presence of the BC. Normalized total displacement amplitudes are plotted in Figure 2.3. Figure 2.3 shows the wave fields (total normalized displacement) at four acoustic frequencies with and without the BC arrangements.

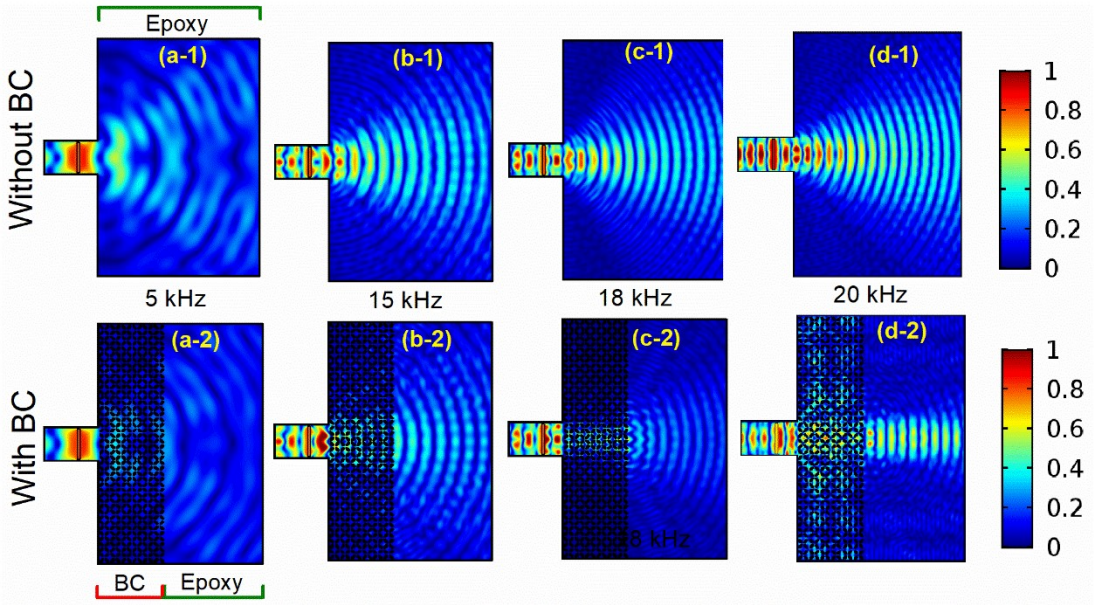

Figure 2.3: Normalized total displacement comparing the wave propagation at 5 kHz, 15 kHz, 18 kHz and 20 kHz with and without BC region.

Comparing Figure 2.3(a-1) and 2.3(a-2), at frequency ~5 kHz, it is evident that very similar circular wave fronts are generated in the base material and in the material with the BCs. This indicates that the presence of BC region does not affect the wave propagation at ~5 kHz. Similarly, at ~15 kHz and ~18 kHz, transmission of the circular wave fronts is also visible. Despite the presence of the BCs, patterns in the wave fields

are unaffected which are shown in Figure 2.3(b) and 2.3(c), when the microstructures are comparable to the respective wave lengths at respective frequencies. While the presence of the butterfly metamaterial region is unrealized by the incident waves at or below ~18 kHz, circular wave front starts to alter due to the presence BCs at or beyond the ~19 kHz, i.e. towards the end of the audible frequency range. At ~20 kHz, the effect (Figure 2.3(d-1) & (d-2)) of BC is strongly realized. Therefore, the proposed structure acts as an acoustically transparent media throughout the 90% of the audible frequency range but demonstrate meta structure features beyond ~20 KHz. It is designed such a way that the individual resonant frequencies of the steel-balls, split rings and the closed elliptical steel rings are achieved at frequencies higher than ~20 kHz, which resulted in acoustic transparency feature below the ultrasonic range. In ultrasonic frequency range (> 20KHz), the propagation of the wave fronts and the wave fields are significantly affected by the BC region and, as an example, a large band gap region is shown in Figure 2.1(b). The acoustic transparency feature is particularly important in such cases where the effect of BC is desirable only in the ultrasonic frequency ranges when the material block is undetectable at the audible ranges.

2.5 Analysis of Mode Shapes for Wave Bifurcation And Wave focusing

In this section higher order dispersion curves, i.e. frequencies beyond the complete band gap, are studied along the ΓX and MΓ direction inside the first Brillouin zone. During this analysis, the concept of acoustic energy of a propagating elastic wave which directly depends on the group velocity was utilized, qualitatively. It is well known that higher group velocity of a propagating wave results higher acoustical energy [38]. To understand the qualitative measure of the acoustic energy, the mode shapes at different

points on the dispersion curves at the frequency ranges between ~37.085 kHz and ~37.43 kHz were analyzed. In Figure 2.4, a portion of the dispersion curve in ΓX direction along with the mode shapes at ~37.3 kHz is presented. In the top section of Figure 2.4, mode shapes at points 'a' through 'f' are shown next to the frequency vs normalized wave vector plot in ΓX direction. Here, three distinct types of mode shapes are identified. Mode shapes at points 'a', 'b' and 'c', located on mode 18, have the same type of particle displacement at the unit cell level. Similarly, points 'd' and 'e' are marked on mode 17 and have the similar displacement pattern. The last point 'f' which is on the mode 16 has different mode shape than that of all the other points. While points 'a', 'c' and 'e' are located outside the intended frequency range, identifying the mode shapes at these points is required to understand the influence of the dispersion behavior found in mode 16, 17 and 18. It can be noted that points 'b', 'e' and 'f' are located on three different modes around at equal frequency level. The assumption that the mode shape patterns of these points are the determinant of the wave propagation direction, can be deduced from the respective acoustic energy requirement. Since the measure of the group velocity directly depends on the slope of the dispersion curve, it can be observed that

$$\frac{dw}{dk}_b > \frac{dw}{dk}_f > \frac{dw}{dk}_e$$

i.e., $$C_g^b > C_g^f > C_g^e$$

in other words, $$E_b > E_f > E_b$$

Therefore, it is indicative that the point 'e' possesses lower resonant energy compared to other two points. While the influence of three different mode shapes exists

at this frequency point, to propagate the wave with mode shape other than point 'e' requires higher acoustic energy. Considering this argument, mode shape of point 'e' can be taken into consideration for wave to be propagated in ΓX direction. A closer observation of the lowest energy mode shape at point 'e' reveals that the two non-oscillating region exists alternatively among three higher-order oscillating regions; and all these oscillations are aligned along a line parallel to the ΓX direction. At point 'e', the strength of the oscillating region found at the middle of the unit cell is lower than that of the oscillations found at the top and bottom section of the unit cell. The displacement patterns of this mode shape indicate that the transmitting wave needs to be propagated in orthogonal direction to ΓX. Therefore, the mode shape of point 'e' directs the propagating wave to transmit in both +y and -y direction locally. However, the transmitting wave from the first unit cell to its adjacent second unit is again dominated by the mode shape of point 'e'. Therefore, the second unit cell locally bends the transmitting wave orthogonally while maintaining the global wave propagation in ΓX direction. The lower part of Figure 2.4 (boxed part) explains this feature where 'E' and 'P' indicates the 'Excitation' and 'Propagation' direction respectively. Since the butterfly unit cell can shift the transmitting wave orthogonally, incident plane wave is bifurcated into upward (+y direction) and downward (-y direction) directions locally while preserving the global wave propagation direction (i.e. the wave vector) in x-direction. Therefore, there exists three principle propagation direction of the transmitted waves; one along x-direction and the other two along the +y and -y directions. Resultant of the two principle directions, i.e., x and +y directions, enables the wave to follow in +45° direction. Similarly, resultant of other two driving directions, i.e., x and -y directions, enables the wave to follow in -

45° direction. Hence, in a global case scenario, it is necessary that the transmitted wave should bifurcates inside the BC structure.

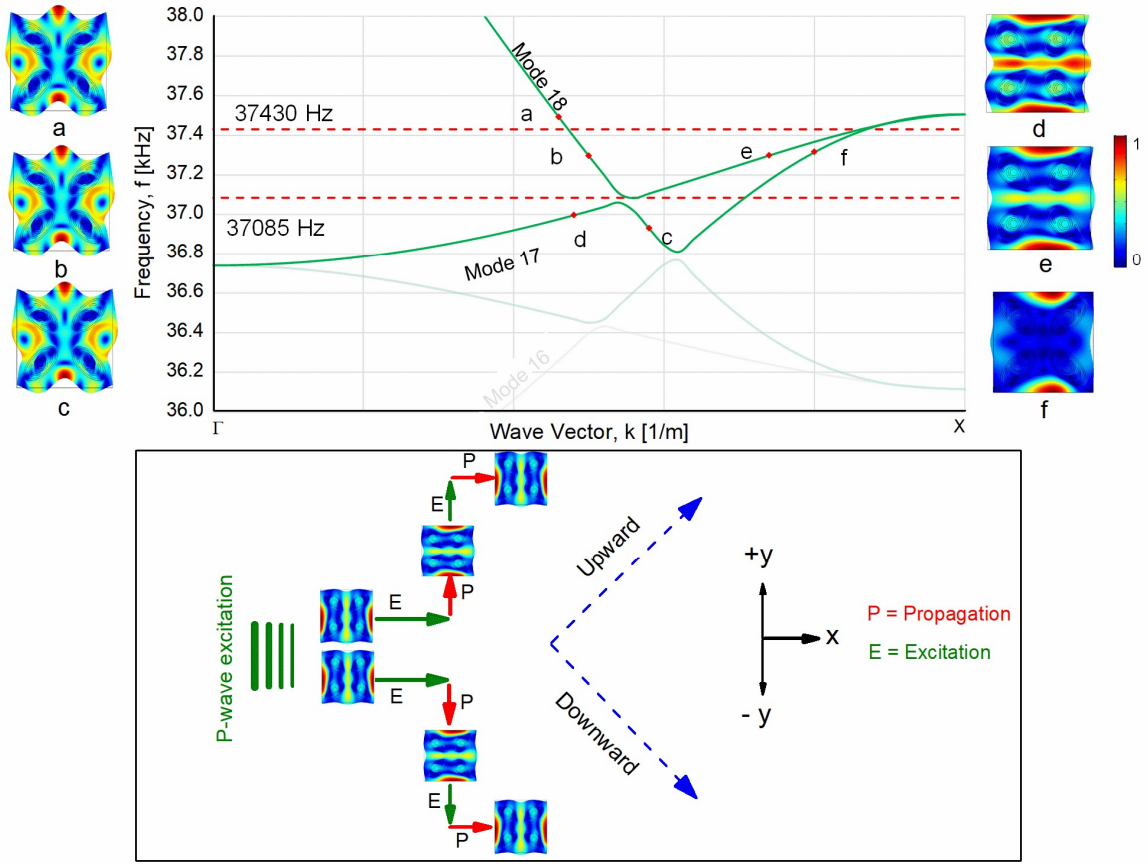

Figure 2.4: Analysis of mode shape and possible wave propagation direction.

To verify the above claim, a frequency domain study is performed for a frequency range of ~37.085 kHz to ~37.43 kHz. The dimension and the rectangular arrangements of the unit cells are kept similar as described in earlier section. At ~37.3 kHz, a remarkable wave focusing phenomenon was observed which is shown in Figure 2.5. This makes the proposed butterfly structure to act as a flat lens so as it can focus the incident plane wave in a single focal point. In Figure 2.5(a), it can be observed that the excited plane wave

initially bifurcates into two wave directions inside the BC, and afterwards these two waves converge into a single point at the outside of the BC.

Inside BC region: At this frequency, when a plane wave excited at zero-degree angle impinges on Epoxy-BC interface, the first lobe of the transmitted wave is strongly dominated by the mode shape of point 'e' (Figure 2.4). The consecutive onward lobes of the transmitted waves show the displacement mode shape pattern as described earlier. However, these lobes consist of both rotated and non-rotated mode shapes of point 'e' which prevent them from nested bifurcation of the transmitted wave. In Figure 2.5(a), the zoomed-in image of the first lobe of the transmitted wave clearly identifies the dominated mode shapes. The particle mode shapes at the first and second columns of the BC region are exactly similar to the mode shape found at point 'e' which is in consistent with the hypothesis of lowest acoustic energy requirement. When these bifurcated waves come out of the interface formed by the BC and the epoxy, the transmitted waves (dashed red arrow) cross each other to make a prominent focus point as shown in Figure 2.5(a).

AT BC and Epoxy interface: At this interface, incident waves are impinged at MΓ direction (in both +45° and -45° direction to x-axis). Therefore, the mode shapes are largely influenced by both x and y components of the wave vectors. To identify the dominant mode shapes, the portion of dispersion curve related to MΓ direction is analyzed. At 37.3 kHz, the mode shapes of mode 16, 17 and 18 are presented in Figure 2.5(b). Slope at point 'a' on mode 16 has lowest value which indicates the lowest group velocity compared to the points 'b' and 'c'. Therefore, the mode shape at the point 'a' possess lowest acoustic energy. Thus, propagating wave requires lowest energy to propagate with the mode shape similar to the point 'a'. Hence, mode shape at point 'a' is

the dominant mode shape in MΓ direction. The complex oscillation pattern of the dominating mode shape at point 'a' can be utilized to explain the wave propagation direction. Considering the displacement pattern of the mode shape at the point 'a', it can be observed that the displacement of the particles along the two diagonals have different values. While the displacement along one diagonal is zero, the displacement of another diagonal is positive. The diagonalized displacement pattern creates 45° local wave propagation direction indicated by negative 45° black arrows in Figure 2.5(b). Therefore, any wave incident at positive 45° at BC-Epoxy interface, transmits at negative 45° direction. By symmetry, waves incident at negative 45° at the BC-Epoxy interface, transmits at positive 45° direction. As the waves come out of the BC region and transmit through the isotropic epoxy media, the wave propagation direction remains same and eventually cross each other to form a circular focal region.

Determination of frequency at maximum focal point intensity: At this point, the intensity of the focal points is calculated in terms of particle displacement for the intended range of focusing frequencies. It is determined that the focal points are located approximately 125 mm away from the PC region and, therefore, the total surface integral of the particle displacement is numerically calculated at these points. These displacements are plotted against increasing frequency as shown in Figure 2.5(c). A maximum oscillating displacement of $6x10^{-5}$ m^2 is found at 37.28 kHz which is where all the mode shape patterns are analyzed.

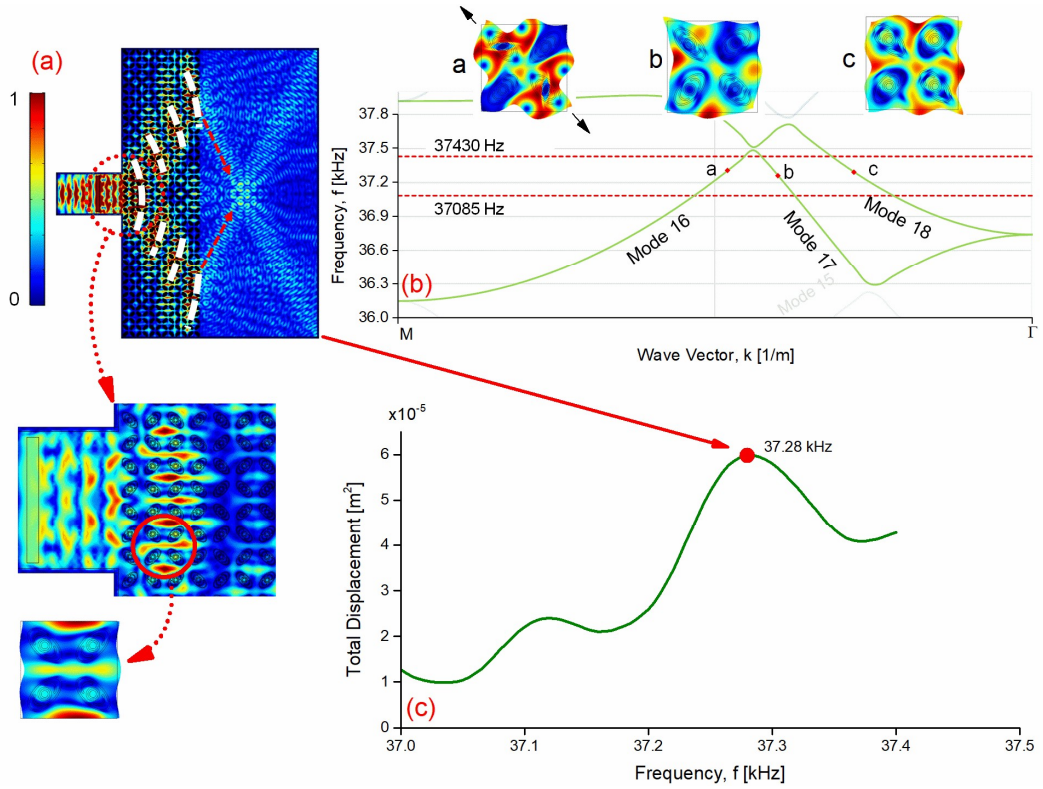

Figure 2.5: (a) Determination of dominant mode shape in wave bifurcation, (b) Mode shape of points 'a', 'b' and 'c' in MΓ direction, (c) Identification of maximum total displacement at the focal point over the focusing frequency range.

2.6 Superlensing: Beyond The Diffraction Limit

The formation of acoustic focal points indicates the existence of negative refraction property of the proposed butterfly structure. While forming an acoustic image, the smallest feature that a conventional acoustic flat lens can form is limited by the spatial frequency. As the acoustic waves emitted from a source includes evanescent waves that conveys the subwavelength information, focusing waves into spot sizes smaller than the wavelength is almost impossible using conventional methods. To overcome this diffraction limit, a structure having negative refraction property can be utilized as a super lens. To investigate the possibility of superlensing capability of the

BCs, two different simulation configurations is designed. First, only one rectangular exciter of 12.7 mm x 12.7 mm (Figure 2.6a-1) is excited in the host media with a frequency of 37.285 KHz. Next, two exciters (Figure 2.6b-1) of similar size placed in the base Epoxy medium at a distance of 0.7λ are excited at the same frequency of 37.285 kHz. The distance, d, between two extreme points of two exciters was kept smaller than the wavelength of the base Epoxy material. To calculate the p-wave velocity in Epoxy, p-wave elastic modulus, M, is used in the following equation:

$$V_P = \sqrt{\frac{M}{\rho}} \text{ where, } \mathrm{M} = \frac{E(1-\vartheta)}{(1+\vartheta)(1-2\vartheta)}$$

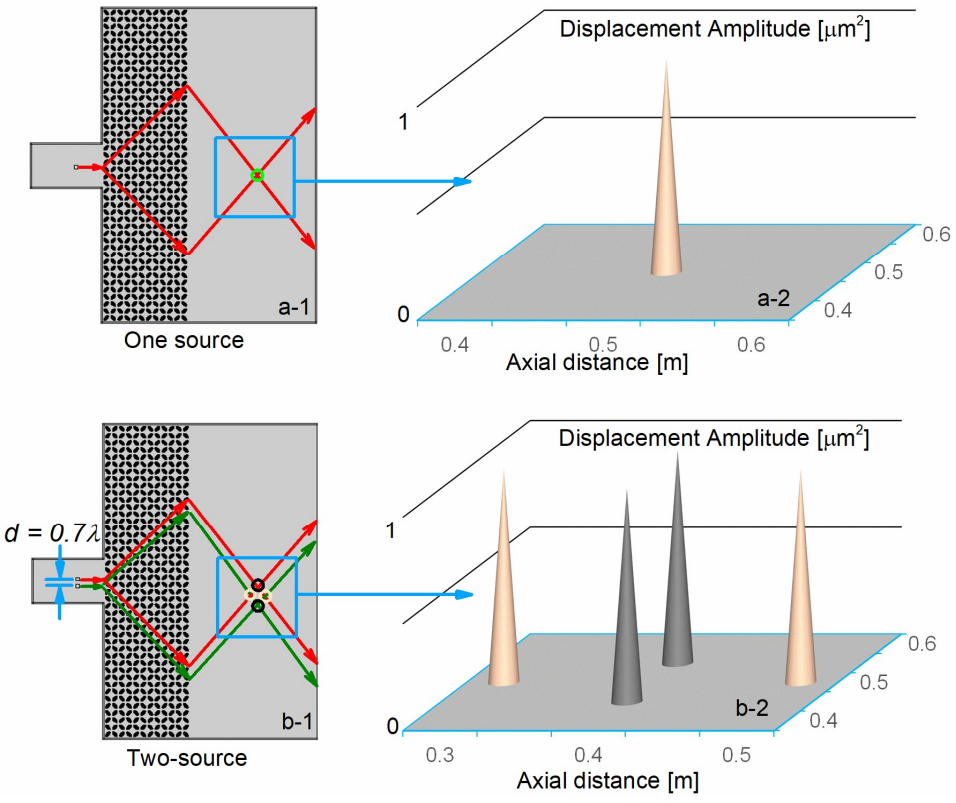

Figure 2.6: Demonstration of superlensing capabitity of Butterfly structure, (a) design configuration with one exciter, (b) design configuration with two sources.

At f = 37.285 kHz, the calculated wavelength is found to be 53.34 mm., and in simulation, the distance d = 38.1 mm is used which is about 0.7λ as shown in Figure 2.6(b-1).

The simulation results of displacement amplitudes at the focusing area are presented in Figure 2.6(a-2) and 2.6(b-2). Any focal point measured a displacement amplitude greater than 100 μm^2 has been presented as 1 μm^2 in Figure 6. In case of one source configuration, a prominent single focal point is found with a displacement amplitude of 228.6 μm^2, and in Figure 2.6(a-1), this amplitude has been shown as 1 μm^2 . However, for the two-source configuration, clearly four focal points are generated as shown in the schematic diagram in Figure 2.6(b-1). From the simulation results, total displacement amplitudes of these four points are calculated numerically which are 198.12 μm^2, 178.6 μm^2, 177.78 μm^2 and 101. μm^2. Since the displacement amplitudes of these focal points are greater than 100 μm^2, they are presented as 1 μm^2 in Figure 2.6(b-2). It is clear that the BC can create focal points of acoustic sources that are separated by less than one wavelength of the base Epoxy material.

2.7 CONCLUSION

In summary, a butterfly shaped engineered metamaterial consisting of an array of steel resonators at multiple-length scales embedded in Epoxy matrix has been analyzed which was previously proposed for creating wide band gap. The numerical analysis shows that the structure remains acoustically transparent to the propagating wave below ~18 kHz. A comparison of wave propagation simulation along with the dispersion curves confirms this feature with or without the repeating structure. To verify the simulation

configuration, wave propagation behavior is presented in the band gap region where no displacement is found for the particles located in and out of the butterfly crystals. In a frequency range of ~36.9 kHz to ~37.43 kHz, mode shapes are analyzed to understand the wave propagation behavior by establishing the relationship between the acoustic energy and the group velocity. Based on this analysis, the dominant mode shape in the resultant displacement field is identified which predicts an apparent wave bifurcation phenomenon inside the BC. In accordance with this concept, negative refraction feature of the unit cell arrangement is observed which attributed to the formation of acoustic focal point. The numerical results are shown to illustrate the predicted wave bifurcation and wave focusing phenomena. Thus, it has been established that the proposed structure is capable of focusing plane wave front which is incident at the normal direction to the BC interface. In this focusing frequency range, the maximum displacement of the focusing points is found as $6x10^{-5}$ m^2 at ~37.28 kHz. By understanding this focusing mechanism, negative refraction property of the BC has been illustrated. Two acoustic sources are placed at a distance smaller than the wavelength of the Epoxy base material at ~37.28 kHz. By measuring the displacement amplitude at the focal points created by these two sources, the superlensing capability of the BC structure has been demonstrated. In brief, the capability of creating multiple acoustic features such as acoustic transparency, wide acoustic band gap, acoustic flat lens and superlensing phenomenon can make this butterfly structure a suitable candidate for biomedical ultrasonic imaging, wave guiding and marine transportations.

CHAPTER 3

INVESTIGATION OF WAVE TRAPPING AND ATTENUATION PHENOMENON FOR A HIGH SYMMETRY INTERLOCKING MICRO-STRUCTURE COMPOSITE METAMATERIAL

3.1 ABSTRACT

Extracting improved mechanical properties such as high stiffness-high damping and high strength-high toughness are being investigated recently using high symmetry interlocking micro-structures. On the other hand, development of artificially engineered composite metamaterials has significantly widen the usability of such materials in multiple acoustic applications. However, investigation of elastic wave propagation through high symmetry micro-structures is still in trivial stage. In this work, a novel interlocking micro-architecture design which has been reported previously for the extraction of improved mechanical properties has been investigated to explore its acoustic responses. The finite element simulations are performed under dynamic wave propagation load at multiple scales of the geometry and for a range of material properties in frequency domain. The proposed composite structure has shown high symmetry which is uncommon in fiber-reinforced polymer composites and a desirable feature for isotropic behavior. The existence of multiple acoustic features such as band gap and near-isotropic behavior have been established. An exotic wave propagation feature, wave trapping and

attenuation has shown energy encapsulation in a series of repeating structures in a frequency range of 0.5 kHz to 2 kHz.

3.2 Introduction

Design and construction of multifunctional materials is one of the challenging research fields due to the requirement of improved overall performance of artificial materials. Incorporating intricate geometry structure at multiple length scales provides highly promising techniques to improve the performance of constituent materials [39]. Some of the intricate design methodologies to improve mechanical properties such as stiffness and/or damping are summarized by [40-44]. Quantifying the material properties of composite materials is significant in several filed of sciences for example damage modeling [45], energy harvesting [46-50], vibration analysis systems [51-53], and wave field modeling [54, 55]. It has been found that combination of hard and soft phase material to design unit cell can induce multiple properties of a material system [56]. Estrin et. al. [57] have utilized the concept of topological interlocking structure which introduces an unusual property such as negative stiffness within a material without damaging or buckling stem. Thus, interlocking structure has been considered as a promising research field in material science. On the other hand, unit cells of a periodic structure are the building block of most of the artificially engineered materials. Periodic crystals [26] comprise of regular lattices of scattering unit cells. Among them, Phononic (PnCs) and photonic crystals (PCs) are periodic composite materials, widely studied for last few decades in many sectors of wave propagation. One of the prime findings of periodic metamaterials is Bragg scattering, which ultimately gives rise to acoustic bandgap [58-60]. Exploiting the bandgap phenomena, many novel wave-control

applications have been proposed [61-64], especially in electromagnetic and acoustic noise control [65], acoustic collimation [66] and acoustic imaging [32, 67]. Several acoustic wave tools such as equifrequency contour [68, 69], determination of effective properties, acoustic emission [70, 71], propagation of guided Lamb wave etc. have been successfully applied to analyze the wave propagation phenomenon. Lately, energy trapping and absorbing has been one of the application fields using acoustic bandgap [72-76]. Energy can be confined inside the periodic media by inserting a defect into the lattice by altering any of the scattering elements, which helps the energy to get trapped inside [77-79]. Energy getting trapped inside the PnCs within the frequency bandgap yields a high-quality factor cavity, having dimensions of about half the wavelength. However, to achieve acoustic energy trapping, the periodicity of the phononic crystals need to be broken by inserting defect or irregularities within the matrix. This reduces the wave-guiding capabilities of the crystals that minimizes the applicability of the metamaterial.

In this chapter, we have proposed a combination of interlock architecture along with the concept of phononic crystal arrangement. micro-structure, yielding a phononic crystal, which is capable of trapping acoustic wave within the periodicity within bandgap frequency, without inserting any artificial defect. Trapping energy within periodic media keeping the crystals unchanged has never been reported before. We propose to numerically study the occurrence of acoustic trapping in an interlock structure comprised of two different materials. The originality of this study lies in the wave field distribution inside the resonators, having an excitation located in the far-field of the metamaterial. This study can be of interest in the field of seismic hazard evaluation from geophysical point of view, for complicated structures clustered together.

3.3 Design Considerations And Band Diagram

Designing an interlock structure requires careful consideration of physical parameters and desired outcome. The motivation and design considerations of the proposed interlock structure are based on the near-isotropic nature of planar hexagonal geometry described by [80]. Moreover, the isotropic features of planar graphene were recently proved as a result of regular hexagonal geometry in its lattice organization.

3.4 Unit Cell Geometry And Its Materials

The geometry of the interlock structure unit cell has two distinct entities – a triangular block and a circular gear block. The first building block of the unit cell is designed as triangular shaped having circular shaped vertices which eventually contribute to the formation of interlock when positioned into the second block. The second block is designed to hold six triangular shaped blocks. These two types of block keep a distance of 0.25 mm. A schematic diagram is shown in Figure 3.1a. The sides of the base hexagon are considered as the unit cell length 'a' and the length of each side of the isosceles triangle is a/2 located at the mid-point of each side of the hexagon. Finally, the diameter of the circular heads of the triangle is designed as a/8. While considering the constituent materials, emphasis was given on the commercial availability of the material and the ease of manufacturability. Therefore, polymetrhyl methacrylate (PMMA) is chosen as the stiffer material for both triangular and circular gear elements. In the design of unit cell, the space between these two elements are connected and make only one route. This space is filled up with locally available soft Silicone Rubber (SR). The properties of these two materials are listed in the following table.

Table 3.1. Material properties.

	PMMA	**Silicone Rubber**
Young's Modulus	3 *(GPa)*	0.9942 (*MPa*)
Poisson's ratio	0.35	0.47
Density	1180 (kg/m^3)	1600 (kg/m^3)

3.5 Band Diagram And Feature Extraction

To understand the physics behind the wave propagation phenomenon through phononic crystal arrangement, group velocities and the mode shapes at multiple eigenfrequencies are the initial requirement. Hence, the dispersion behavior of the proposed structure is obtained using finite element base commercial package COMSOL Multiphysics. Utilizing eigenfrequency study, by varying the wave vector in reciprocal space of a hexagonal lattice structure the band structure of the unit cell is obtained. In this analysis, Floquet periodicity is assumed at all boundaries of the hexagonal cell. The dispersion band structure shown in Figure 3.1c is numerically computed for ΚΓΜΚ boundary of the first Brillouin zone of Figure 3.1b. Clearly, a large bandgap is located between ~7kHz to 8.5 kHz. In this study, the interested range of frequency is 0.5 kHz to 2 kHz as the band diagram shows a linear dispersion in this region.

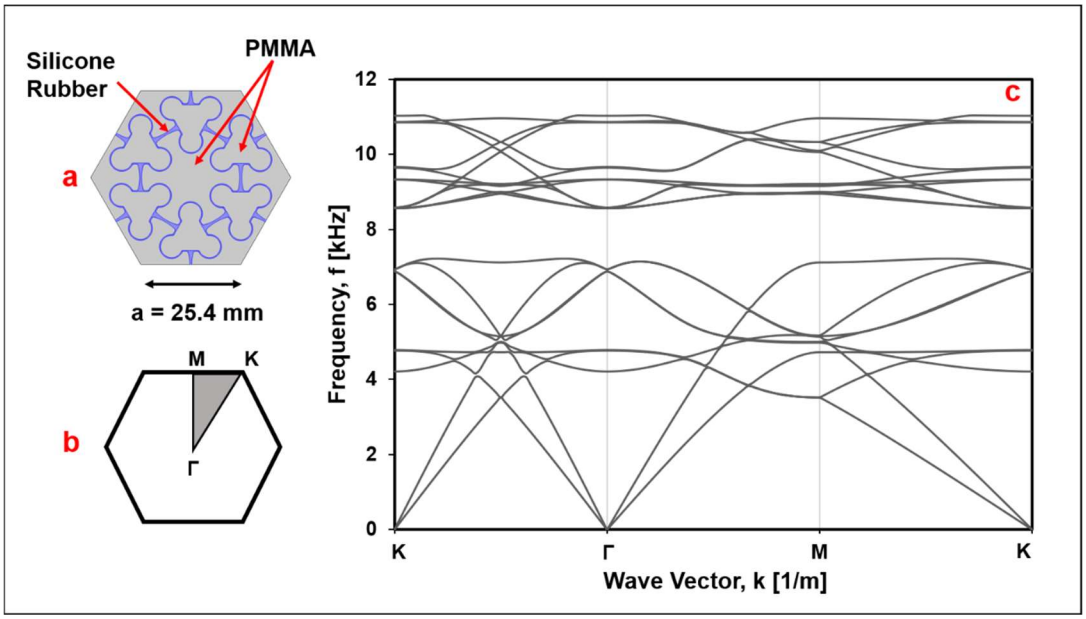

Figure 3.1: a) Geometry of the unit cell and materials used, b) Reduced Brillouin Zone, c) Band diagram of the proposed interlock structure.

3.6 Simulation Setup

The objective of the simulation setup in this study is to demonstrate wave trapping and attenuation phenomenon. A total of three configuration geometries are designed by repeating the hexagonal lattice structure. First and second configurations have a guided wave displacement excitation at the left side of the crystal matrix. Both configurations have same height, however, the width of first configuration is double than the other. Third configuration has same height and width of the first configuration; however, a circular excitation source is placed at the center point by removing adjacent unit cells. All these configurations are surrounded by base PMMA material. To avoid boundary reflection, a 50 mm thick perfectly matched layer is assumed at all boundaries of all geometric configurations. Frequency domain analysis is performed using structural mechanics module of COMSOL Multiphysics for a frequency range of 500 Hz to 2 kHz.

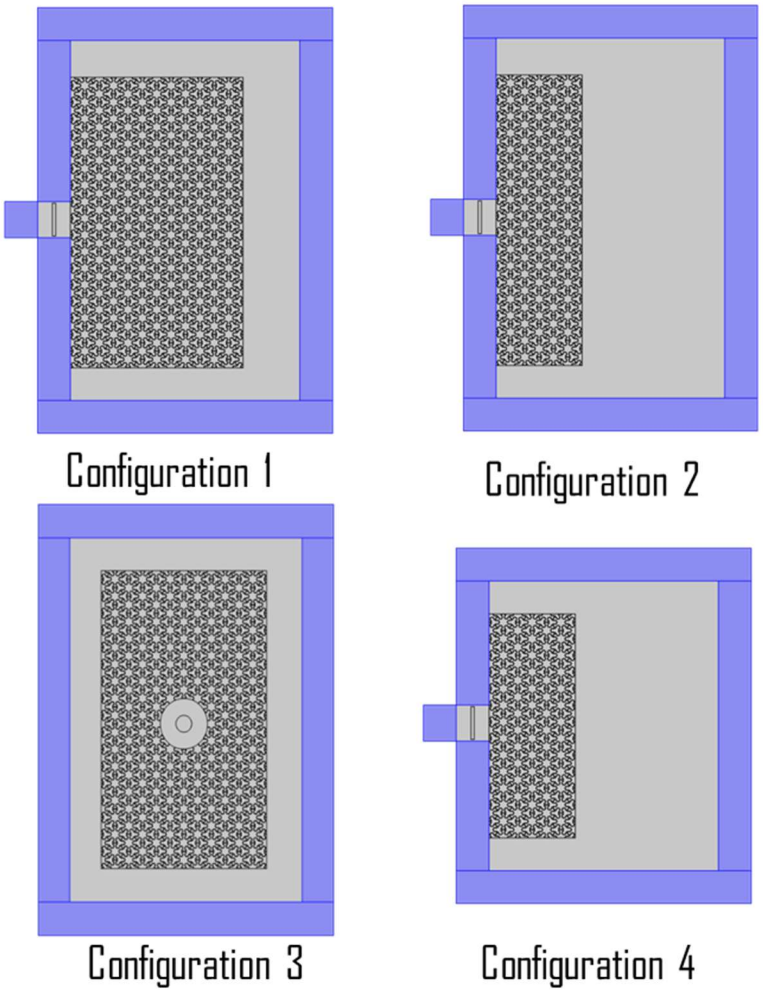

Figure 3.2. Simulation configurations. Configuration 1: full width and height of PnCs, Configuration 2: half width and full height of PnCs, Configuration 3: full width and height with central excitation, Configuration 4: reduced width and height. Configuration 1, 2 and 4 have left side plane wave excitation.

3.7 Results And Discussion

Wave trapping phenomenon: Displacement amplitudes at these frequencies are shown in Figure 3.2. Clearly, all these geometric configurations show increase of displacement amplitudes as the frequency increases to 1.35 kHz and then follows a decrement until 2kHz. Figure 3.2a shows displacement amplitudes of first configuration

where propagated wave has been trapped inside the phononic crystal arrangement. At these frequencies, the boundaries of the crystal matrix remain unperturbed and displacements of the unit cells are confined within the matrix.

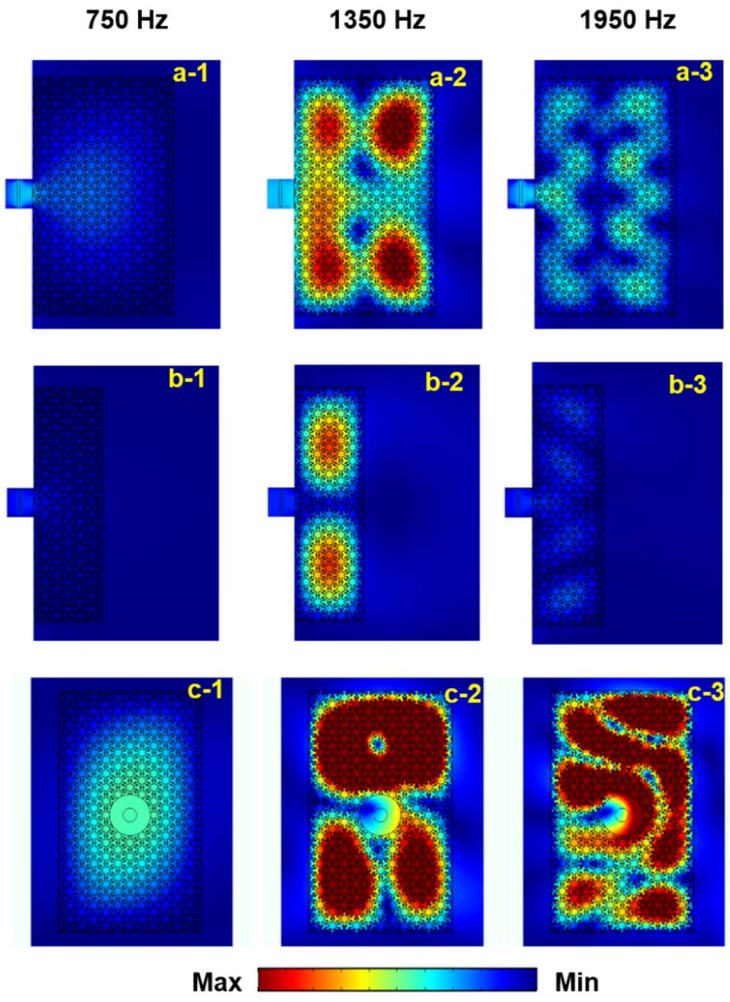

Figure 3.3: wave displacement amplitudes (a) first, (b) second and (c) third configurations at 750 Hz, 1350 Hz and 1950 Hz demonstrating wave trapping and attenuation phenomenon.

To isolate the effect of matrix width, the width of the matrix geometry of second configuration is reduced by half of first configuration. It has been found that the wave transmission pattern follows the same behavior as the first configuration, confinement of

wave inside the matrix bounded by the matrix boundaries. The interphase between the phononic matrix and the base PMMA does not allow the wave to propagate outside of the matrix boundaries. To demonstrate further, third geometric configuration is utilized to excite wave inside the crystal matrix in 45º direction with MK. Clearly, as the frequency increases, the magnitude of the total solid displacement increases and form specific displacement pattern. However, irrespective of the wave displacement amplitudes pattern, the propagated waves are trapped and do not transmit through the matrix boundaries. The wave propagation phenomenon using the third geometric configuration also demonstrates that the change of excitation direction does not affect the wave trapping capability of the proposed structure.

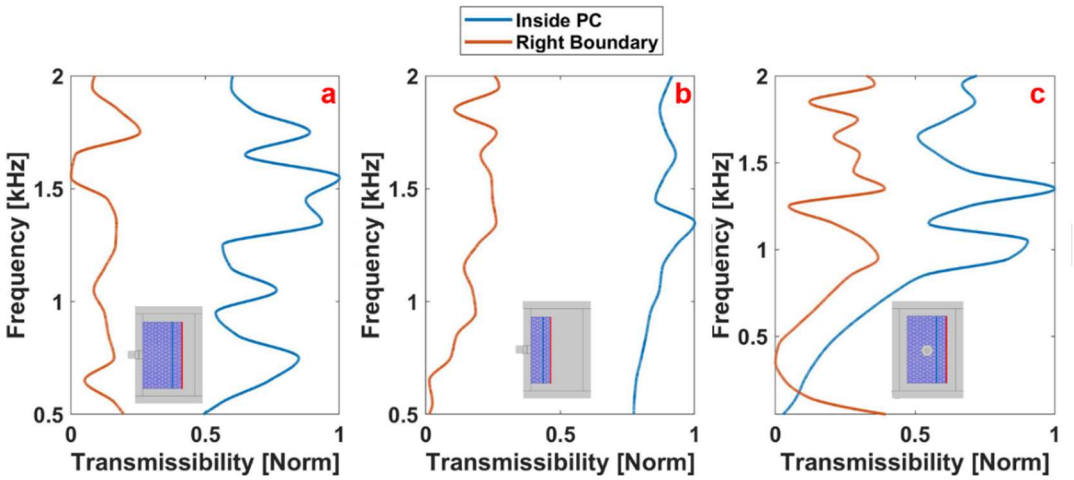

Figure 3.4: Transmissibility of (a) first, (b) second and (c) third configurations at right boundary and inside phononic crystal matrix.

Wave attenuation phenomenon: Wave attenuation phenomenon is observed in this interlock structure which is a complementary effect of wave trapping behavior. As most of the incident wave is trapped inside the phononic crystal matrix, a sudden attenuation is observed at the interphase between the crystal matrix and the base PMMA. To

demonstrate this behavior, magnitude of the wave transmission is measured at the boundaries. Two lines are chosen, one at the right boundary and the other at 75% of the width inside the matrix. A line integral of total displacement amplitude of the respective line is calculated which is termed as transmitting wave. Thereafter, the line integral of total displacement amplitude of the incident wave at the incident boundary is calculated and termed as incoming incident wave. Finally, the ratio of transmitting wave at one line to the incoming incident wave is calculated. These ratios are graphically shown in Figure 3.3 corresponding to respective geometric configurations.

It can be clearly seen from Figure 3.4 that the transmissibility at the boundaries of the matrix is much lower than that of matrix inside. This explains the trapping of wave energy inside the phononic crystal matrix and the attenuation of wave energy at the boundaries. This phenomenon has been demonstrated from 500 Hz to 2 kHz. As the frequency increases, the wave transmissibility pattern inside the PC and at the boundaiesy follows each other. Around 1.35 kHz the wave transmissibility is the highest compared to other frequencies which is in line with the displacement amplitude found in Figure 3.3.

Analysis of mode shape in three principal direction in Figure 3.5 indicates that excitation of incident wave in ΓM direction yields a wave propagation in the direction of excitation. Notably, solid displacement around the center of the unit cell is higher than that of top and bottom region. This behavior of wave propagation forms excitation to neighboring other unit cells which then follow the mode shapes of KΓ and MK directions. Combination of these three mode shapes creates a rotational wave displacement inside the phononic crystal matrix which prevents wave to transmit out of the matrix boundary.

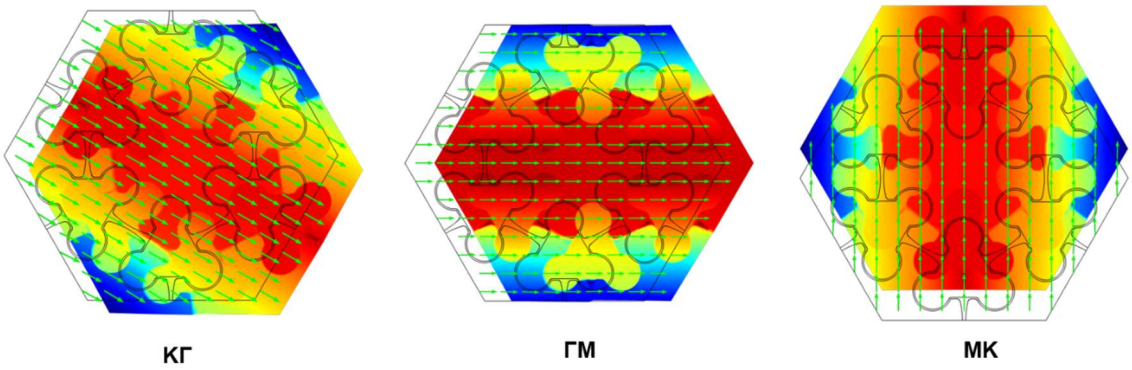

Figure 3.5: Mode shape with direction of energy propagation

3.8 Strength Optimization of Interlock Structure

Inspired by the fascinating mechanical and acoustic features, the proposed interlock architecture is studied further to increase mechanical strength by varying geometric parameters. An optimization scheme is adopted to analyze a characteristic Representative Volume Element (RVE) with the accurate boundary conditions. The constituent materials of the RVE are PMMA (E = 3 GPa, ρ = 1180 kg/m^3 and υ = 0.35) and Polyrethane (E = 45 MPa, ρ = 1200 kg/m^3 and υ = 0.35). In this optimization process, tie contact and friction contact are considered between PMMA and PU. The optimized geometry with tie contact shows ~10% improvement in yield strength as shown in the stress-strain diagram in Figure 3.6.

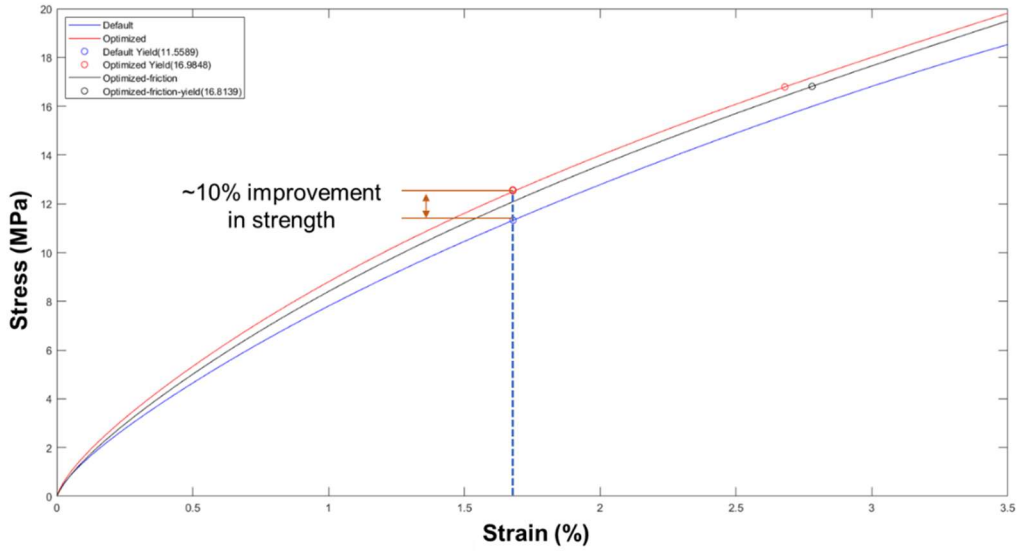

Figure 3.6: Stress-strain diagram of original and optimized interlock geometry [81].

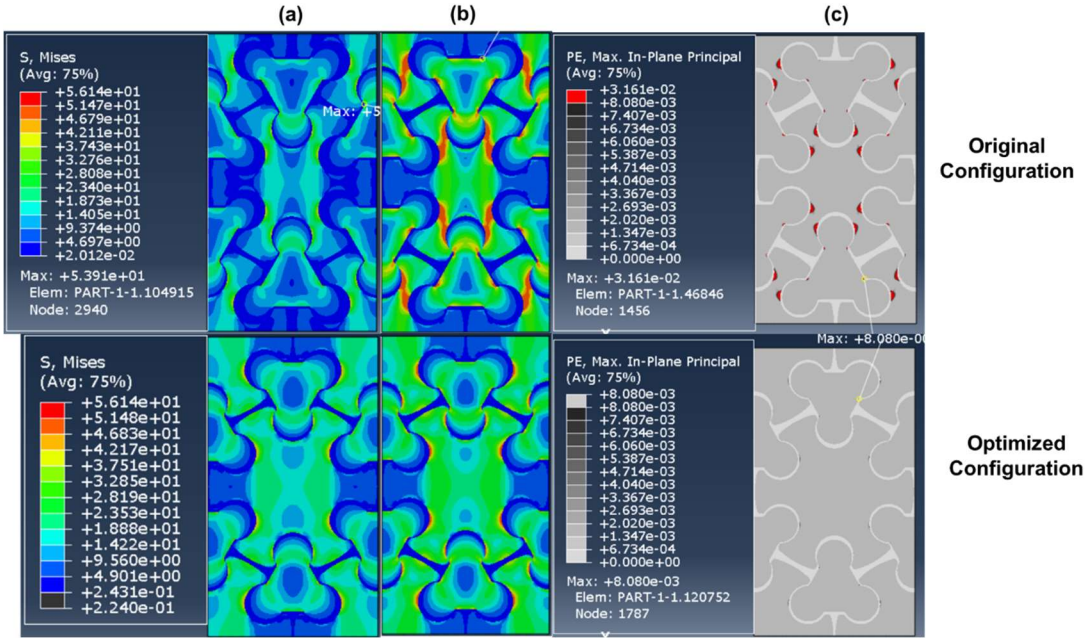

Figure 3.7: Simulation results of Von-mises stress of RVE (a) onset yield, (b) 3.5% strain and (c) plastic strain [81].

Balabadhruni [81] also demonstrated Von-mises stress comparison of the original and optimized geometry for onset of yield strain, 3.5% of yield strain and plastic strain. The results are as shown in Figure 3.7. The simulation results show that the higher stresses are developed across the top and bottom triangular PMMA structure through the central gear shaped PMMA structure. With introduction of friction and cohesive contact, a small drop in stiffness is observed, however, the yield strain practically remains same. As PU behaves like a gel, the value of friction coefficient doesn't have any visible effect. Simulation results with friction coefficients are shown in Figure 3.8.

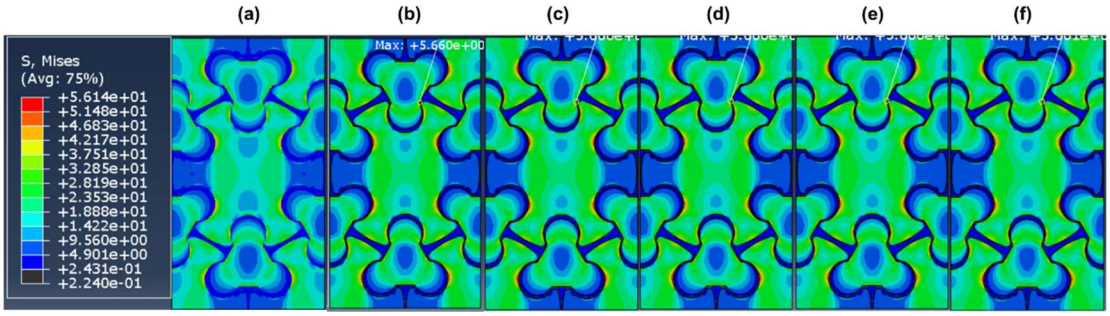

Figure 3.8: Simulation of Von-mises stress with (a) Tie contact, (b) frictionless, (c) friction coefficient = 0.05, (d) friction coefficient = 0.1, (e) friction coefficient = 0.2 and (f) friction coefficient = 0.5 [81].

Due to the improved mechanical strength of this optimized geometry, a further investigation is required to identify its acoustic properties. Therefore, this optimized interlock geometry will serve as the input geometry of the next chapter.

3.9 Conclusion

In this article, an interlock architecture repeating structure has been proposed which was previously studied for improved mechanical properties such as combined

stiffness and damping. By determining the band structure using a hexagonal lattice arrangement, a band gap and a linear dispersion behavior are observed and analyzed for wave propagation phenomenon. In a frequency range of 0.5 kHz to 2 kHz, wave trapping and attenuation behaviors are demonstrated. As the frequency increases, the solid displacement amplitude inside three geometric configurations increases until 1.35 kHz and then decreases until 2 kHz. Additionally, wave transmissions at the boundaries of the matrix structure have been calculated and compared with the incident wave displacement. Transmission of wave shows a significant attenuation through the matrix boundaries. Finally, a research conducted at Michigan State University is mentioned. In this research an optimization scheme is demonstrated to determine the optimized geometric parameters that provides higher mechanical strength. This optimized geometry is an input for Chapter 4.

CHAPTER 4

INVESTIGATION AND INTEGRATION OF OPTIMIZED INTERLOCK STRUCTURED METAMATERIAL AS AN AD-HOC METASTRUCTURE

4.1 ABSTRACT

Integration of metamaterial along with conventional NDE transducer is investigated and a design of ad-hoc metastructure is proposed in this chapter. The interlock metamaterial described in Chapter 3 is primarily adopted as the working metastructure. This metastructure is recently being investigated with optimized geometry for extracting improved mechanical properties such as high stiffness-high damping and high strength-high toughness. In this Chapter, the band structures, mode shapes and equifrequency contours at multiple frequencies are studied for this interlocking architecture to achieve wave focusing and generating Bessel Beam. The finite element simulations are performed for long distance wave propagation and the results are post-processed to show the existence of Bessel Beam phenomenon at ~271 kHz. A concluding simulation is performed using ad-hoc interlocking metastructure to propagate wave through a combination of attenuating epoxy and carbon fiber reinforced polymer composite plate. Full penetration of wave inside thick composite plate is clearly observed.

4.2 Introduction of Optimized Interlock Architecture And Band Structure

A brief introduction of interlock structure has been provided in chapter 3 where the interlock structure was studied for wave trapping and attenuation. This structure has been studied further for increase mechanical strength by varying geometric parameters. An optimization scheme was adopted to analyze a characteristic Representative Volume Element (RVE) with the accurate boundary conditions. The constituent materials of the RVE were PMMA (E = 3 GPa, ρ = 1180 kg/m^3 and υ = 0.35) and Polyrethane (E = 45 MPa, ρ = 1200 kg/m^3 and υ = 0.35). Since the optimized geometry has different geometric parameters compared to its original counterpart, the band structure and wave propagation behavior need to be studied considering it as a new geometry. A comparison of geometric parameters of the original and optimized unit cell is shown in Table 4.1 and the optimized geometry is shown in Figure 4.1.

Table 4.1: Comparison of geometric parameters of original and optimized unit cell.

Parameter	Original Value (mm)	Optimized Value(mm)
R_g Radius of gear	0.49	0.495
L_t Length of triangle Edge	0.5	0.5
R_t Radius of Triangle head circle	0.22	0.22
h-offset (between Triangle vertex and head center)	0.03	0.10
R-fillet: Fillet radius, Same for all the corners	0.02	0.02
t (thickness of PU)	0.01	0.01

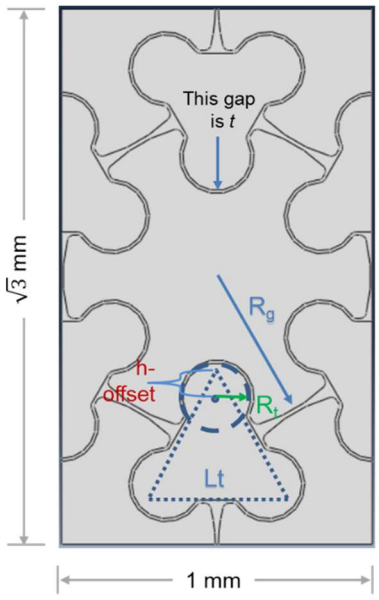

Figure 4.1: Geometric parameters of the optimized unit cell

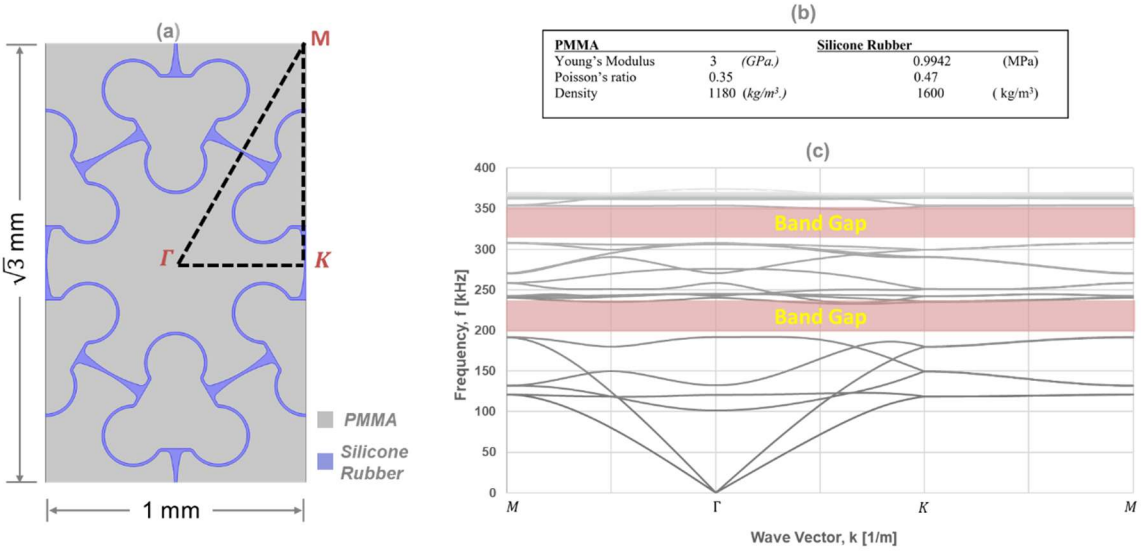

Figure 4.2: (a) Unit cell of interlock metastructure, (b) Material properties used for this metastructure and ((c) Frequency vs. k-space band structure.

In determining the band structure of this metastructure, a new set of material properties is assumed. Instead of PMMA and polyurethane, in this research, PMMA and

silicone rubber is assumed. The reason for choosing silicone rubber in place of polyurethane is that it provides band structures that contain bang gap. The dispersion behavior of the optimized structure is determined by considering the unit cell of the metastructure shown in Figure 4.2(a). While estimating the frequency vs k-space band structure of the unit cell, the ΓKM boundary of the Brillouin zone is identified and shown in Figure 4.2(a) with dotted black line. It can be noted that the ΓM line makes 60° with ΓK. The unit cell is made up of two materials namely polymetrhyl methacrylate (PMMA) and Silicone Rubber. The material properties are shown in a table in Figure 4.2(b). Using eigenfrequency module of commercial FEM based package COMSOL Multiphysics, by varying the wave vector in reciprocal space of the rectangular unit cell, the frequency vs. k-space band structures are obtained and shown in Figure 4.2(c). It can be noted that the Floquet periodic boundary conditions are assumed along boundaries of the rectangular unit cell. Clearly, two band gap regions are visible which are in the frequency range of ~200-240 kHz and ~310-350 kHz.

4.3 Validation of Simulation Parameters

The objective of the simulation setup is to identify the wave propagation behavior which will help to focus incident energy and subsequently propagates waves through epoxy coated composite structure. The first step of this simulation setup is to identify the simulation parameters and validating its result. In this study, one of the frequencies, 225kHz, from the first band gaps region is selected to explore the wave propagation behavior to indicate the validity of the simulation parameters. Before running the simulations, the unit cell is repeated in x and y directions and formed a repeating

structure or interlock phononic crystal (IPC) with an overall dimension as 8.66 mm X 4 mm.

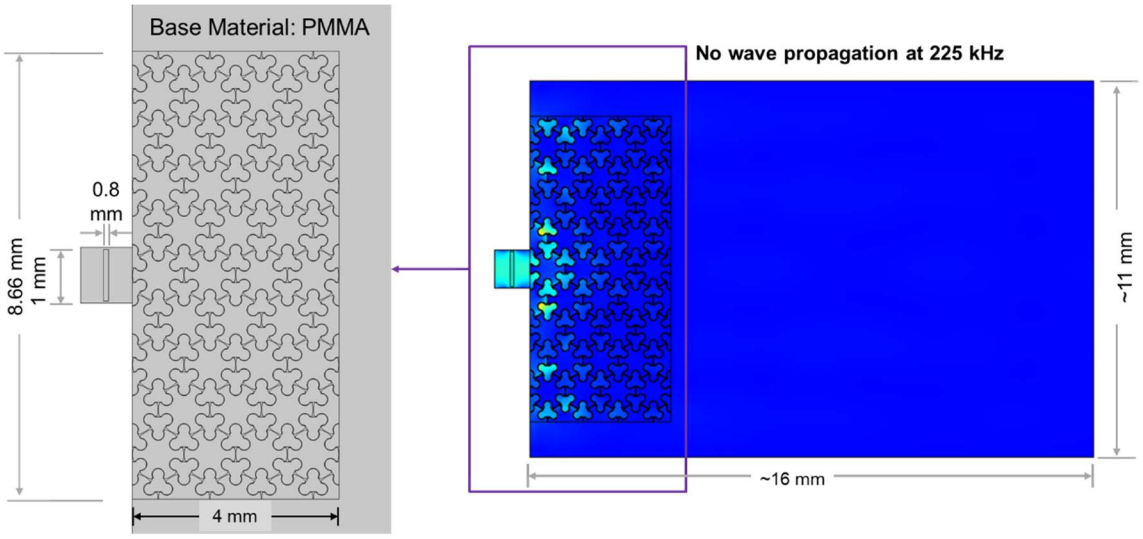

Figure 4.3: Simulation parameters (left) and result at 225 kHz showing no wave propagation through the repeating structure and the base PMMA.

This crystal is then placed in once end of the base PMMA which has a dimension of ~16 mm X 11 mm. A frequency domain simulation is performed at 225 kHz considering perfectly matched layer around the entire structure as an absorbing boundary condition. An excitor placed in PMMA is excited at 225kHz to generate plane wave at zero-degree orientation. It can be clearly seen that no wave is propagated trough the IPC and the base PMMA structure. This simple simulation proves the validity of the simulation parameters and the IPC is then selected for rest of the study. It can be noted that the initial dimensions of the IPC are assumed with an underlying assumption to use it as an ad-hoc structure with conventional NDE transducers.

4.4 Identification of Mode Shapes for Wave Focusing

The interlock architecture shows promising band structure and mode shapes at varying frequencies. Therefore, multiple frequency ranges are investigated for wave propagation behavior so that the wave focusing phenomenon can be achieved. As the primary interest is to excite plane wave in ΓX direction, ΓX part of the dispersion curve is analyzed for mode shapes. After a rigorous investigations of mode shapes at multiple frequency ranges, two range of frequencies are selected for wave propagation analysis. These two ranges are 120 kHz to 135 kHz and 265 kHz to 275 kHz.

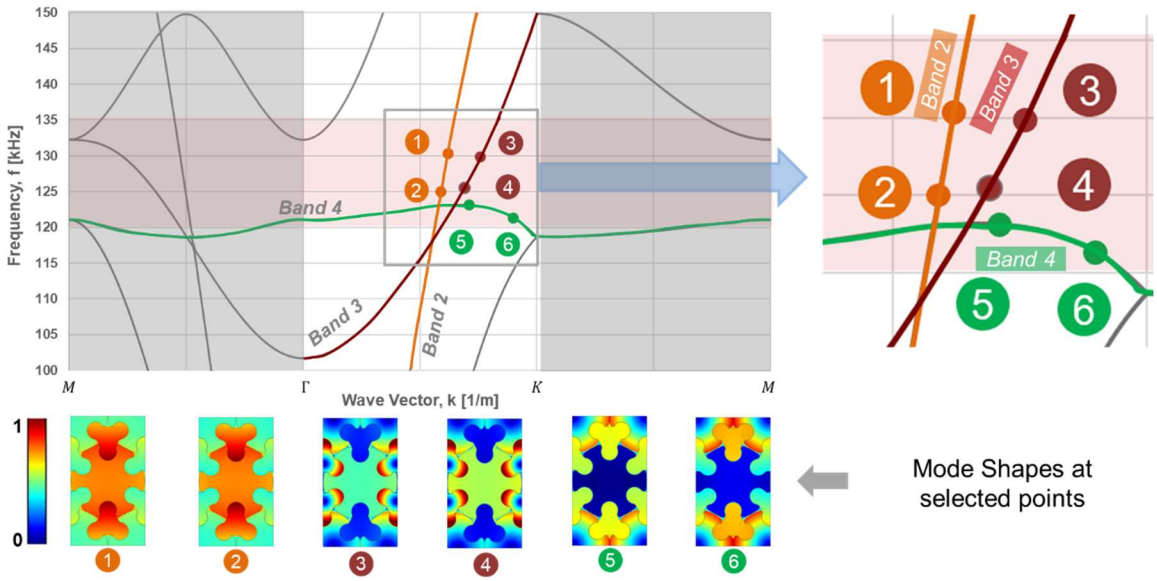

Figure 4.4: Part of the Band structure of the unit metastructure ranges from 100 kHz to150 kHz. Zoomed in figure shows band 2, 3 and 4. Mode shapes numbers at the bottom correspond to the respective selected points on these bands.

Between 120 kHz to 135 kHz, three bands fall in ΓX direction and these bands are band 2, 3 and 4. Figure 4.4 shows the band structure in this frequency range. The zoomed in image shows the pattern of these bands where two points from each band are selected

for mode shape identification. Points 1 and 2 are on band 2, points 3 and 4 are on band 3, and points 5 and 6 are on band 4. The mode shapes corresponding to the selected points are shown at the bottom row of Figure 4.4.

At ~ 121 kHz, the mode shape of point 6 in ΓX direction dominates the wave propagation as only band 4 has the contribution to it. Similarly, at ~123 kHz, the mode shape of point 5 will dominate the wave propagation behavior. On the other hand, at ~125 kHz and ~130 kHz, the mode shape of band 3 and band 4 will dominate the wave propagation. However, as band 3 has lower slope compared to band 2, the mode shapes of band 3 will dominate the wave propagation as explained in Chapter 2. An explanation of wave propagation direction, discussed in next paragraphs, is derived using equifrequency contour at ~121 kHz and ~130 kHz.

Investigation of wave propagation direction using equifrequency contour

Equi-frequency or iso-frequency contour is supplementary in analyzing behaviors of photonic crystals, which is the intersection of a constant frequency ω-plane to a dispersion surface [82, 83]. However, this concept can be utilized in phononic crystals as well. Construction of an equifrequency contour requires eigen frequency solution of k-space in all possible directions. After determining the solutions for a range of frequencies which includes all bands of the dispersion curve within the frequency range, equi-frequency contour can be constructed where each contour would represent a single frequency. Figure 4.5 shows the wave propagation behavior using equi-frequency line ranging from 120 kHz to 122 kHz. It has been established that group velocity at a point on the equifrequency line coincides with the direction of the normal to the equifrequency

surface and the group velocity points towards the increase of frequency. Since PMMA is considered as an isotropic material, its equi-frequency contour can be represented by circular lines. In Figure 4.5(a), the plane wave is excited from the PMMA and impinges on PC region. After propagating through the PC, the wave again propagates through the PMMA. Figure 4.5(b) shows the Equifrequency contour of PMMA. When a plane wave is excited from base PMMA in ΓX direction, it impinges on the PC and propagates omnidirectionally. If the wave passes inside the PC at an angle θ, the resulting direction of wave inside the PC is shown in firm red arrows.

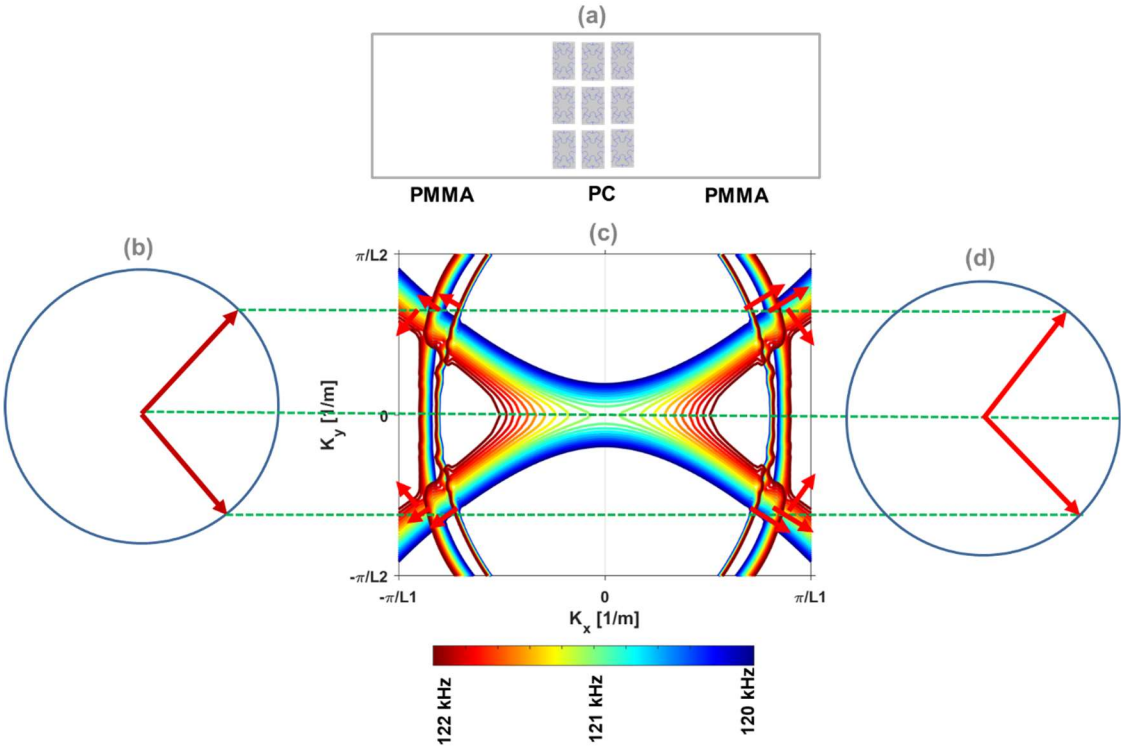

Figure 4.5: Wave propagation behavior using equifrequency contour of interlock phononic crystals and base PMMA.

It can be observed that at 121 kHz, each of the three bands has contribution in wave propagation. Therefore, each arrow corresponds to each band. After propagating

through the PC, wave come out of the PC and impinges on PMMA which is shown in Figure 4.5(d). The arrows in Figure 4.5(d) shows that the wave propagation has both converging and diverging behavior. This behavior is expected for wave focusing phenomenon. During investigation of equifrequency contours from 120kHz to 135 kHz, this converging and diverging phenomenon is evident until ~130 kHz. Beyond ~130 kHz, this phenomenon disappears. Therefore, a frequency domain study is required to investigate wave propagation behavior in a range of ~120kHz to ~130 kHz.

4.5 Frequency Domain Analysis of Wave Propagation

At this stage, using COMSOL Multiphysics, a frequency domain analysis is performed from 120 kHz to 130 kHz. The objective of this simulation is to determine and validate the wave propagation behavior as predicted from equifrequency analysis. The simulation results are shown in Figure 4.6. In these simulations, Figure 4.6(c) to 4.6(e), displacement amplitudes inside the PMMA geometry with PC are shown for ~121 kHz, ~123 kHz and ~130 kHz respectively. It can be observed that in each frequency, the propagating waves bifurcates as they enter into the PC, and clearly two beams of wave are observed at the interphase of right boundary of the PC and the base PMMA. This bifurcation phenomenon of wave is explained in previous paragraphs with the equi-frequency analysis. It can be noted that a negative refraction is observed as the wave came out of the PC to the base PMMA and as the frequency increases the negative refraction angle reduces. Thus, by increasing the frequency, the focal distance can be increased. Figure 4.6(b) shows the zoomed in image of PC where the mode shapes of the unit metastructures are observed. It can be seen that the displacement amplitudes inside the PC are very similar to the mode shape found for band 4 at point 6 which corresponds

to ~121 kHz. Figure 4.6(a) shows the mode shape of point 6 on band 4 to compare them to the displacement amplitudes inside the PC at ~121 kHz.

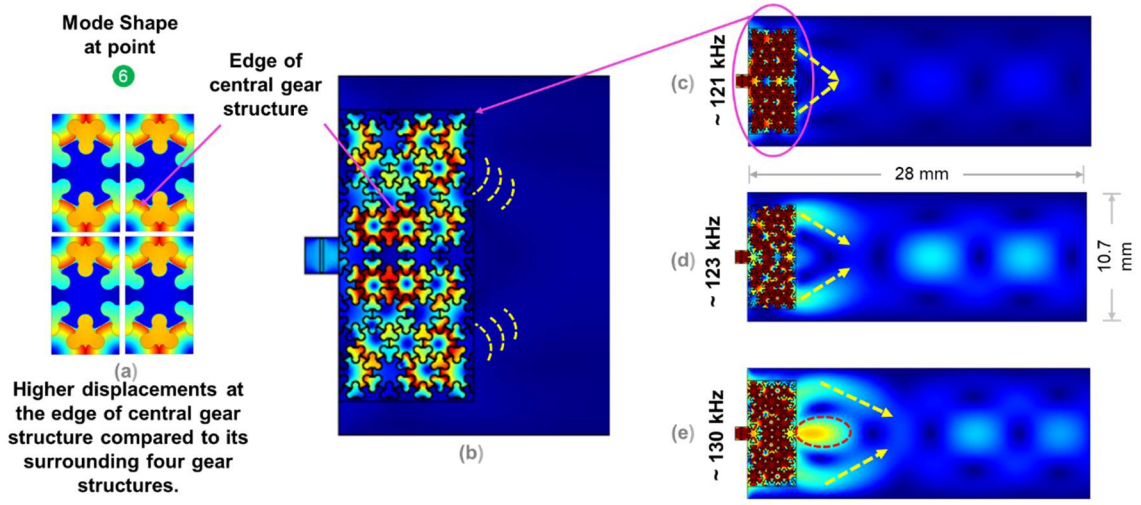

Figure 4.6: Simulation results of frequency domain analysis from 120 kHz to 130 kHz. (a) Mode shape at point 6 on band 4, (b) Zoomed in image of PC region at ~121 kHz, (c) – (d) show displacement amplitude at ~121 kHz, ~123 kHz and ~130 kHz.

From Figure 4.6(b), it is understandable that the wave energy can be focused at a distance from PC-PMMA interphase at ~121 kHz. To bolster this claim of wave propagation behavior, simulation results at ~123 kHz and ~130 kHz are also presented in Figure 4.6(d) and (e). The mode shape and wave propagation direction are also explored at ~130 kHz. The results are shown in Figure 4.7. Similar to the simulation results at ~121 kHz, at ~130 kHz, the wave focal point shifts rightward as seen in Figure 4.7(e). Figure 4.7(b) shows the zoomed in image of the PC at ~130 kHz and the mode shape found inside the PC is similar to the mode shape found at point 3 on band 3 which is shown in Figure 4.7(a). It can be seen that as the frequency increases, the intensity of displacement amplitude increases and at ~130 kHz, the displacement amplitude is larger compared to other two frequencies.

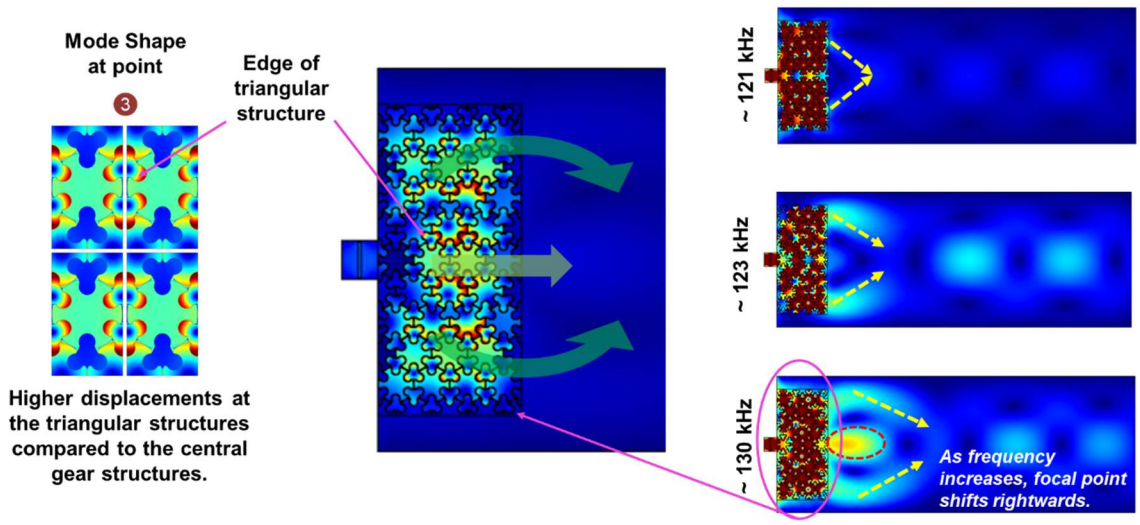

Figure 4.7:Simulation results of frequency domain analysis from 120 kHz to 130 kHz. (a) Mode shape at point 6 on band 4, (b) Zoomed in image of PC region at ~130 kHz, (c) – (d) show displacement amplitude at ~121 kHz, ~123 kHz and ~130 kHz.

4.6 Wave Focusing Inside A Composite Structure

The understanding of wave focusing can be utilized to focus wave energy inside a Carbon Fiber Reinforced Plastic (CFRP) composite material which is one of the primary objectives of this research. Therefore, a geometric configuration is designed utilizing interlock metastructure as a tool to focus wave energy. The geometric design is described in Figure 4.8. In these simulation configurations, a perfectly matched layer is assumed all around the geometry to create absorbing boundary conditions which is shown in Figure 4.8(a). The PC along with PMMA is placed on a 100 mm X 10 mm CFRP composite. The young's modulus and Poisson's ratio this CFRP composite are considered as E1 = 143.8 GPa, E2 = 13.3 GPa and $\upsilon = 0.3$. The configurations are differed from each other by the distance between the PC and the CFRP composite which is filled by base PMMA. The value of this distance in Figure 4.8(b), (c) and (d) are 2 mm, 4 mm and 8 mm

respectively. In each case, the width of the PC with PMMA is considered as 10 mm. All simulations are performed at ~130 kHz.

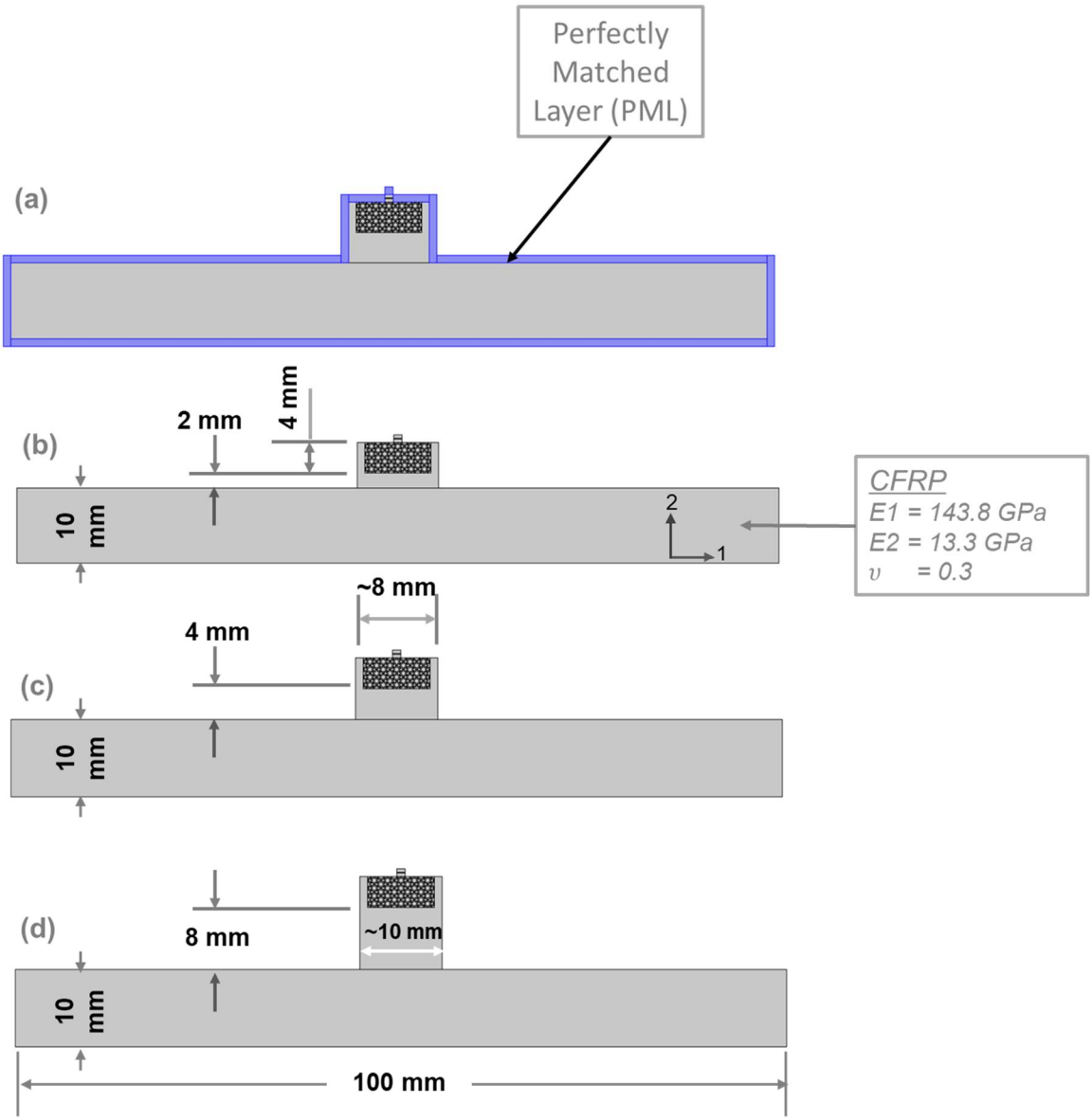

Figure 4.8: Simulation configurations for wave focusing. (a) Shows the location of perfectly matched layers, (b) to (d) indicates the varying distance starting from 2 mm to 8 mm.

The simulation results are shown in Figure 4.9 and 4.10. Wave propagation intensity is calculated with the help of strain energy density function along horizontal and

vertical lines shown in the figures. Since strain energy is the energy stored by a system undergoing deformation, it can be expressed for an elastic material as

$$U = \frac{1}{2} VE\epsilon^2$$ where, V = volume, E = Young's modulus and ϵ = strain.

In these simulations, using effective Young's modulus and strain at each point, the elastic strain energy density (ESED) is calculated for each of the configurations. In Figure 4.9, three horizontal lines are considered to calculate the ESED. Line H3 is considered at the bottom of the CFRP composite to identify whether the penetration of wave can reach to the bottom. It can be observed from the normalized ESED for each line that, at 4 mm distance between PC and the CFRP composite, ESED is highest at the bottom surface of the CFRP composite.

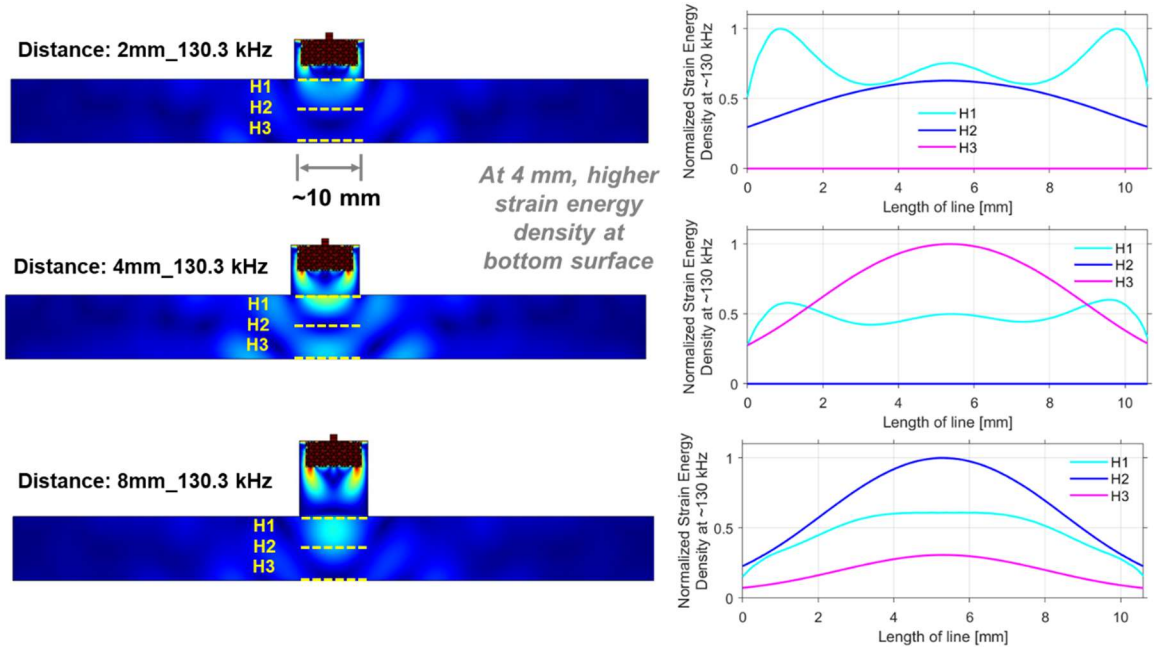

Figure 4.9: Simulation results at ~130 kHz for varying distance between PC and CFRP composite. Corresponding strain energy densities are shown along horizontal lines H1, H2 and H3. With 4mm distance between PC and CFRP composite, higher strain energy density is observed at the bottom surface of CFRP composite.

Similarly, the ESED is plotted for each of the vertical lines shown in Figure 4.10. From these plots, it is evident that at 4 mm distance between PC and the CFRP composite, the ESED is highest at ~7 mm distance from bottom of the CFRP composite. It indicates that the wave energy is focused at ~3 mm from the top surface of the CFRP composite when the distance between PC and CFRP composite is 4 mm. Therefore, ~130 kHz, this interlock structure can be utilized for wave focusing in CFRP composite materials.

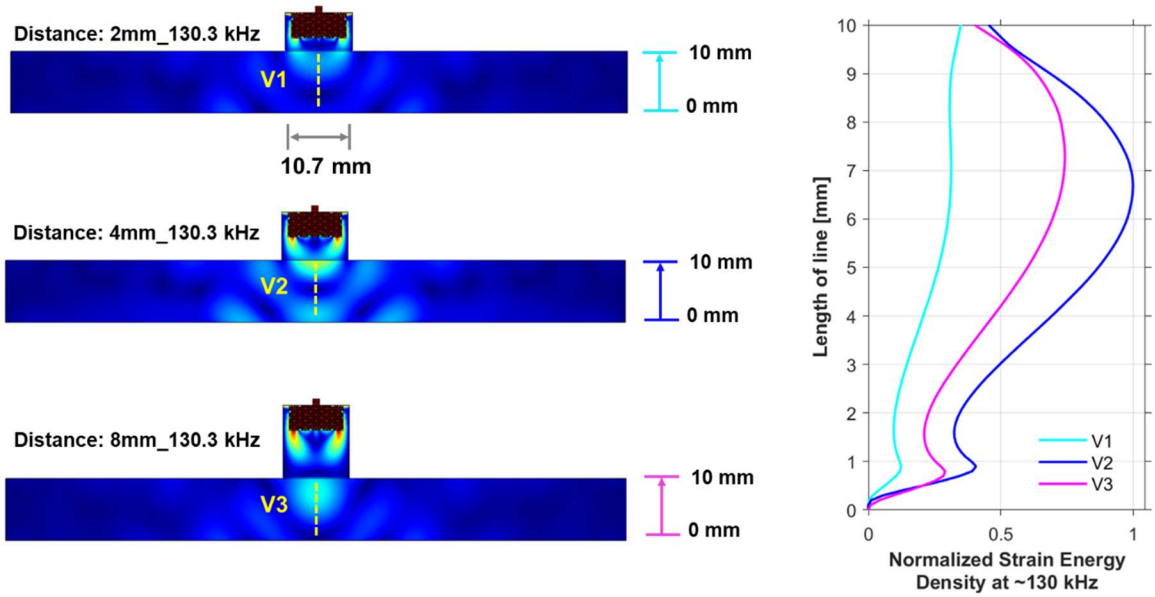

Figure 4.10: Simulation results at ~130 kHz for varying distance between PC and CFRP composite. Corresponding strain energy densities are shown along the vertical lines V1, V2 and V3. At 4mm distance between PC and CFRP composite, higher strain energy density is observed inside the CFRP composite compared to other two distances.

4.7 Identification of Mode Shape for Bessel Beam Generation

A Bessel beam is a wave whose amplitude is described by a Bessel function of the first kind [84, 85]. A true Bessel beam is non-diffractive. This means that as it propagates, it does not diffract and spread out. It has been established that the non-

diffracting [86] Bessel beam can be realized by applying two plane beams with opposite propagating angles, and the overlapping region is the Bessel formation zone [87, 88]. Bessel beam has been realized successfully in many photonic and imaging applications [88-91]. Therefore, it is intriguing to generate and utilize Bessel Beam in acoustic applications. The objective of generating BB is to remarkable utilize it to propagate wave through thick CFRP composite. Therefore, a rigorous investigation is performed to identify mode shape using interlock metastructure that can essentially generate BB. The mode shapes in a frequency range of 265 kHz to 272 kHz show promising result in respect to generate BB. Figure 4.11 shows the dispersion curve of the metastructure and mode shapes of four selected points on band 12 and 13. Points 1 and 2 are located on band 12 and points 3 and 4 are located on band 12. The mode shape of point 1 and point 3 are determined at ~271 kHz whereas the mode shape of point 4 is determined at ~267 kHz.

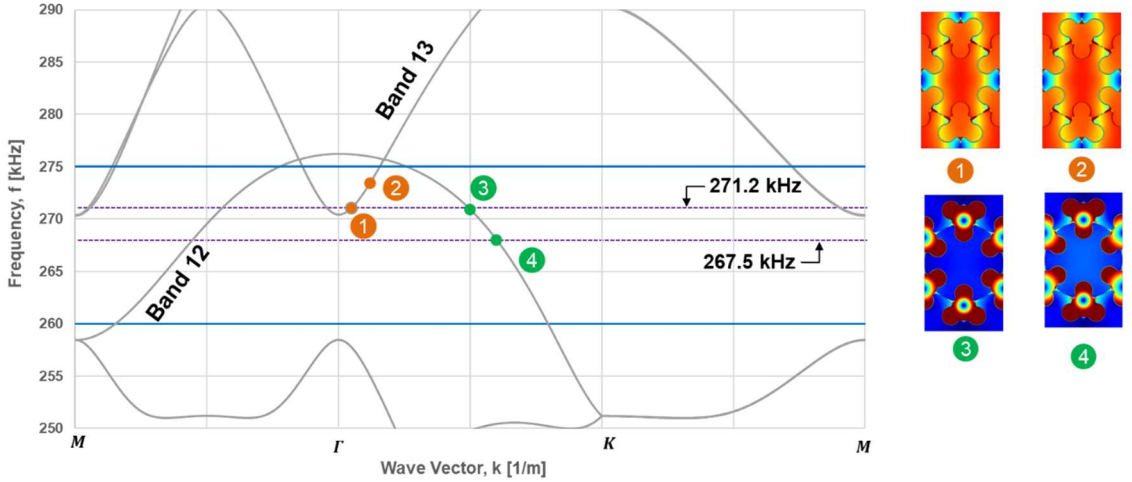

Figure 4.11: Frequency vs. k-space dispersion curve for a frequency range of 250 kHz to 290 kHz. Mode shapes of selected points on band 12 and 13.

By the observation of mode shapes at these two frequencies, the straight crested mode shapes are available at band 13, whereas a circular shaped mode is found at band 12. Therefore, it is logical to estimate a wave propagation which would have a circular crested propagation at 267.5 kHz, and a straight crested wave propagation at 271.2 kHz. However, at 271.2 kHz, the slope of the band 13 is lower than that of band 12, and this would contribute to a domination of straight crested wave propagation while the circular pattern of the mode shape would contribute to a oscillatory wave propagation. With this assumption, a mixture of straight crested wave to the circular wave pattern would provide us a Bessel beam of first kind is hypothesized herein at frequency 271.2 kHz.

4.8 Frequency Domain Simulation at ~267.5 kHz And ~271 kHz

Using the simulation configuration discussed above, a frequency domain simulation is performed at ~267.5 kHz and ~271 kHz. The simulation results are shown in Figure 4.12. As predicted converging-diverging wave propagation is found at ~267.5 kHz as shown in Figure 4.12(a). It can be noted that the displacement amplitudes in base PMMA do not spread out as the wave propagates towards right side which is an indication of Bessel beam behavior. Therefore, the length of the base PMMA is doubled and found consistent long-distance propagation of wave. This result is shown in Figure 4.12(b). The next set of simulations are performed at ~271 kHz with normal and doubled length base PMMA. As predicted the influence of straight crest mode shape is found effective and the simulation results show generation of BB in both configurations. These are evident from Figure 4.12 (c) and (d).

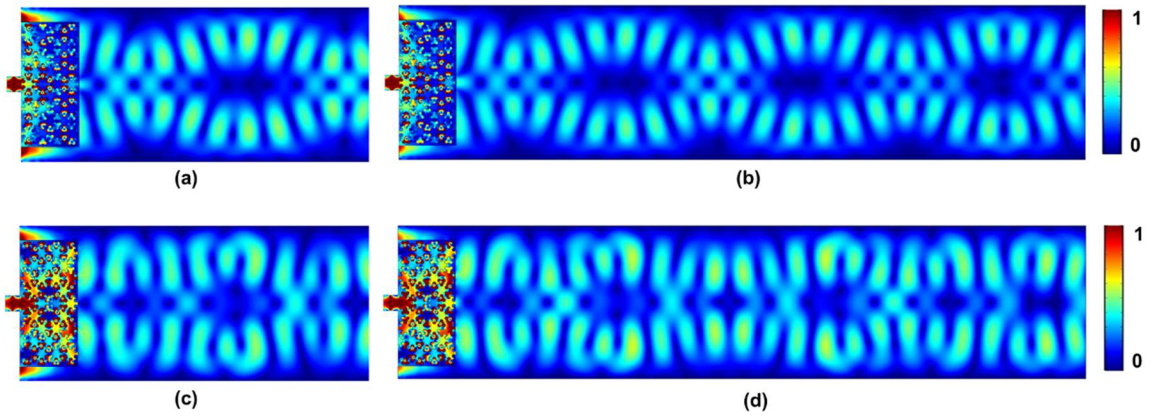

Figure 4.12: (a) and (b): Simulation results at ~267.5 kHz. (c) and (d): simulation results at ~271 kHz.

At this stage, an analysis is performed to measure the ESED at varying distance when the wave come out of the PC. Therefore, two vertical lines and two horizontal lines are chosen to calculate the ESED at ~271 kHz.

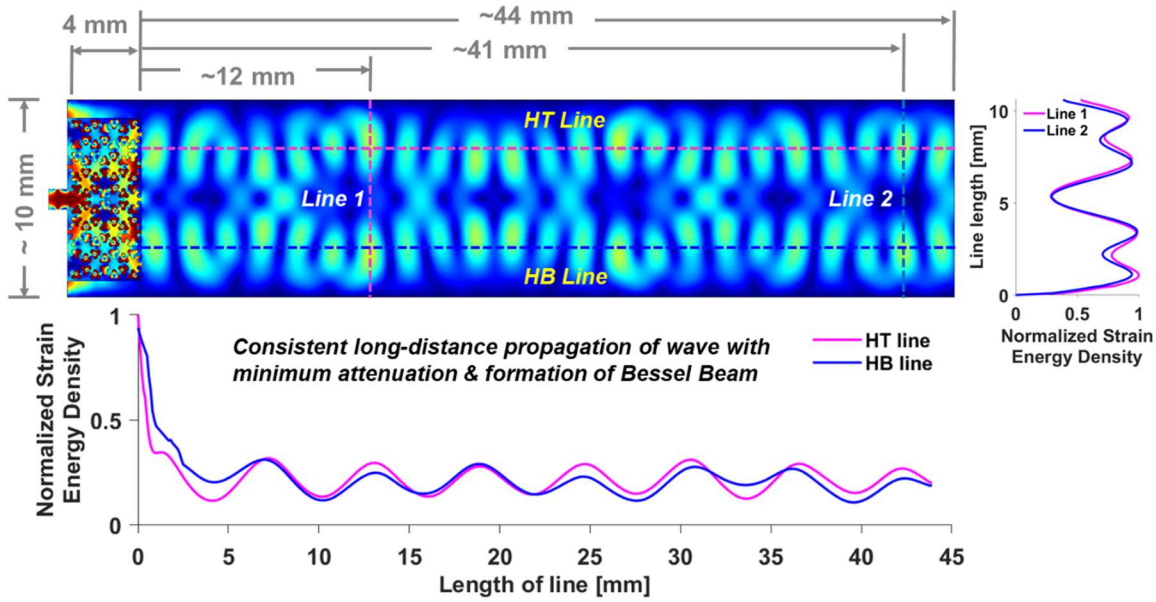

Figure 4.13: Generation of Bessel Beam at ~271 kHz. Elastic strain energy density along two horizontal and two vertical lines are shown at right and bottom of simulation result.

The results are shown in Figure 4.13. The ESED along two vertical lines, Line 1 and Line 2, are shown right side of this Figure. From this estimation, it is evident that the ESED at ~12 mm and at ~41 mm is almost same along these vertical lines. Moreover, ESED along two horizontal lines are shown at the bottom of Figure 4.13 and shows consistent long-distance propagation of wave with minimum attenuation. Thus, formation of BB is evident at ~271 kHz which can be effectively utilized to propagate ultrasonic wave through CFRP composite materials.

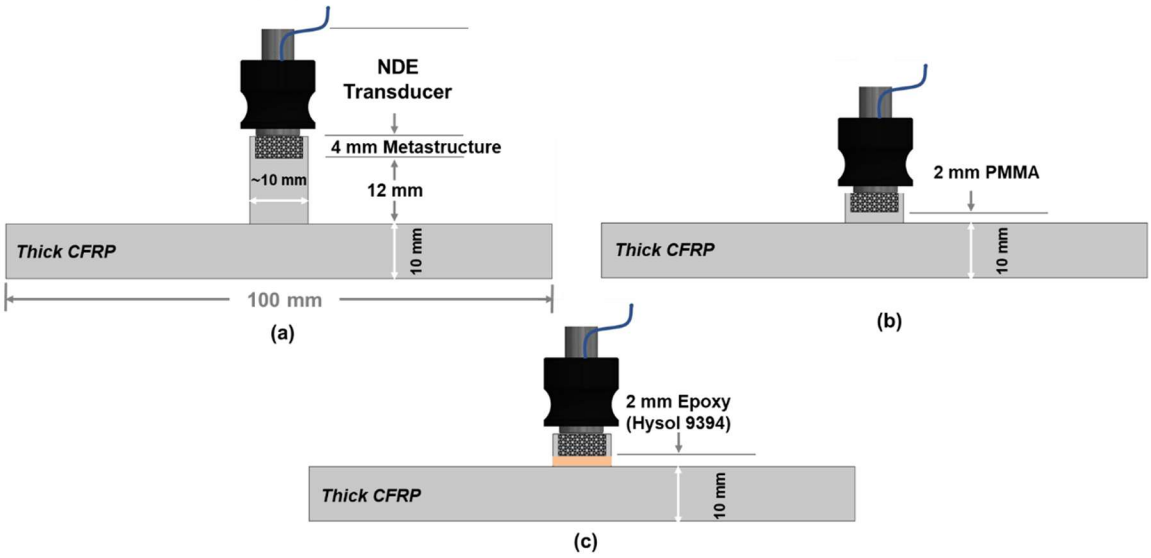

Figure 4.14: Geometric configurations to propagate Bessel Beam using ad-hoc metastructure.

4.9 Simulation of Ad-Hoc Metastructure with CFRP Composite

Three simulation configurations are designed to generate BB using ad-hoc metastructure. These configurations are shown in Figure 4.14. An image of NDE transducer is added to each configuration to resemble its position as plane wave exciter. In configuration (a), the distance between the metastructure and the 10 mm thick CFRP

composite is filled with 12 mm PMMA. In configuration (b), this distance is reduced to 2 mm and filled with PMMA. The last configuration has the same distance between metastructure and CFRP composite, however, it is filled with industry standard Epoxy (Hysol 9394). The material properties used for this Epoxy are as follows: Young's modulus, E = 4.23 GPa, Density, ρ = 1360 kg/m^3 and poisson's ratio, ν = 0.3. With these geometric configurations, simulations are performed at ~271 kHz and BB are generated. The simulation results are shown in Figure 4.15. Bessel beams are generated in each configurations and full penetration wave inside the thick composite is observed. The result of configuration (c) shows that even the presence of Hysol 9394 ultrasonic wave is capable to propagate through the CFRP composite.

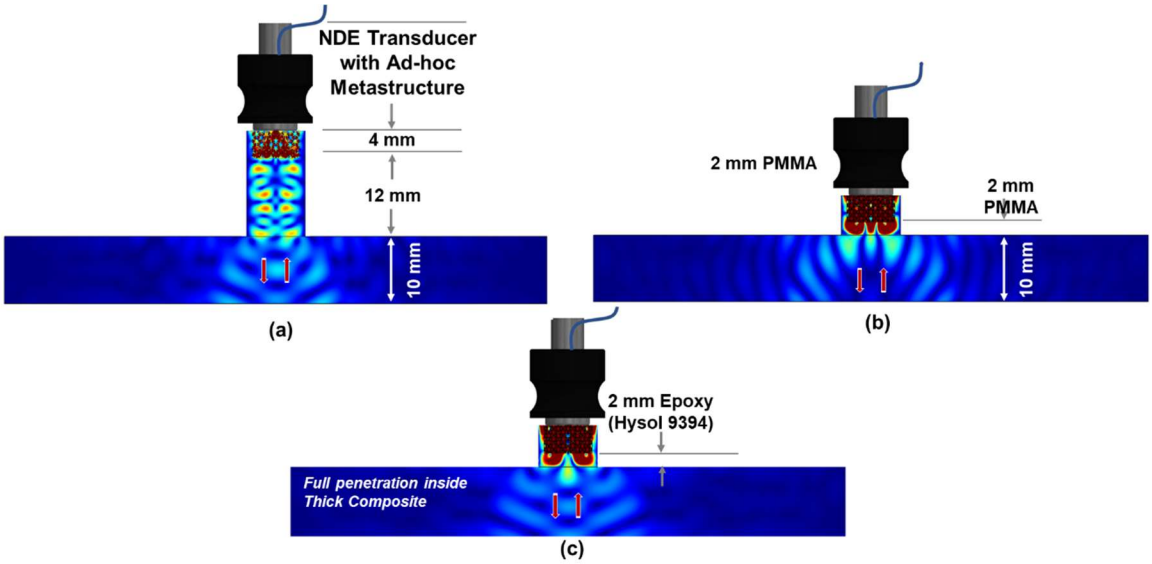

Figure 4.15: Simulation results at ~271 kHz where Bessel Beam are generated in three geometric configurations. (a) with 12 mm PMMA, (b) with 2 mm PMMA and (c) with 2 mm Epoxy (Hysol 9394).

4.10 CONCLUSION

In this chapter, an optimized design of interlock architecture is introduced and integrated with conventional NDE transducer as an ad-hoc metastructure. As an initial step, the band structure is determined and investigated for mode shapes for possible wave focusing phenomenon. Based on the mode shape analysis, a range of frequency is identified at which wave propagation phenomenon is calculated. Within this frequency range, three frequencies, ~120 kHz, ~ 123 kHz and ~130 kHz are identified, and frequency domain analysis is performed. These simulations effectively show wave focusing inside 10 mm thick composite plate. Further investigation of modal analysis yields mode shapes that have the capability of generating Bessel Beam. These mode shapes are determined at ~267.5 kHz and 271 kHz, and frequency domain analysis are performed. After post-processing, the simulation result it is evident that the wave propagation at ~271 kHz possesses elastic strain energy density which has negligible attenuation as it propagates through a long distance.

CHAPTER 5

ULTRASONIC ACOUSTIC WAVE FOCUSING IN LAMINATED COMPOSITE MATERIALS USING SPECTRAL ELEMENT METHOD

5.1 BACKGROUND

The advantages of Non-Destructive Evaluation (NDE) in determining material state awareness of operational structural components are the key motivating factors leading to develop numerous computational tools. As human knowledge on wave propagation behavior in solids and fluids evolved day by day, the role of NDE based computational tools became inevitable so far. Numerous researchers around the world developed multiple mathematical models on wave propagation and implemented them to analyze structural problems [91-95]. Rapid development of computer architecture and its computational power gave scientists and researchers an immense opportunity to boost up NDE computational tools to the academy and industry to design high efficiency structural elements.

Damage initiation and growth in structural elements is a very significant problem since in most cases it leads to catastrophic accidents. In case of structural elements made from composite materials, matrix cracking, delamination and fiber breaking are especially dangerous modes of failure. That is why in order to improve safety and

reliability of such structures, periodic inspections are necessary. For this reason, a variety of online structural health monitoring systems and strategies have been developed [96, 97].

The objective of this chapter is to focus acoustic ultrasonic energy with the help of Spectral Element Method. First, a comparative study on Fininte Element Method (FEM) and Spectral Element Method (SEM) has been presented. Then a mathematical formulation to solve the wave propagation problem in laminated composite materials has been derived, specifically to simulate wave interaction with composite structure using pulese-echo (PE) ultrasonic transducer (UT). The PE ultasonic signals have many features that are not known because actual intearaction of the wave with different ply and ply thickness is poorly understood. The anisotropy of composite material plays a critical role in affecting the signal pattern which is not apparent in isotropic materials. Many Finite Element Modeling (FEM) approaches have been propsoed to simulate the wave interactions without any satisfactory results at high frequencies in the Mega Hertx (MHz) range. Therefore, in this work, SEM is introduced and mathematiocal details are presented to solve a wave propagation problem numerically.

5.2 What Is SEM?

The spectral Element Method is relatively a new addition to the history of computational techniques. This technique basically combines the advantages of two different numerical techniques which is spectral methods and finite element methods. In structural analysis, these two techniques had been utilized widely for their accuracy and ease of use. Spectral element methods are high-order weighted-residual techniques for

partial differential equations that exploit both the common foundations and competitive advantages of h-type finite element methods and p-type spectral techniques [98-100]. Therefore, in short, it can be said that, the spectral element method is a high-order finite element technique that combines the geometric flexibility of finite elements with the high accuracy of spectral methods.

As proposed by Patera in 1984 [101], The SEM is capable to investigate material state damage with the propagation of elastic waves in structures of varying geometries. The basic idea and working principle of SEM is very similar to FEM with some exception in approximating specific functions. The very first difference is the location of interpolation nodes. In SEM, elemental interpolation nodes are chosen at points corresponding to the zeros of an appropriate family of orthogonal polynomials such as Lobatto or Legendre or Chebyshev polynomials [102, 103]. A set of local shape functions consisting of Lagrange polynomials are built and used which are spanned on these points. Due to this approximation and the use of Gauss-Lobatto - Legendre integration rule, a diagonal form of the mass matrix can be obtained. Adopting these techniques, the computational or numerical cost is much less expensive than in the case of classic finite element approach. The second difference with FE approach is the degree of approximating polynomials. Whereas in FE linear or quadratic shape functions are widely used in commercial applications, in SEM the use of higher order polynomials is a common practice. Introduction of diagonal mass matrix and higher order polynomial decreases the numerical errors faster than any power of 1/p where the p is the order of the applied polynomial. Problems often approached by the use of SEM are associated with the phenomena such as wave propagation, interference and diffraction in continuous

media of various types (solids, liquids and gasses), gas or liquid flows, diffusion and many others [104, 105].

5.3 A Comparative Analysis on FEM Vs. SEM

As a popular and widely used method, the FEM is employed to solve complex problems from multi-disciplinary physical sciences that can be expressed by partial differential equations or integral equations. Examples of such problems usually can be found in fluid mechanics, solid mechanics, thermodynamics, electro and magneto statistics and dynamics and many others. The working principle of FEM involves the discretization of the analyzed area into a finite number of smaller subdivisions normally termed as finite elements, within which solutions are determined by approximating suitable polynomials over evenly spaced nodal points [106, 107]. As the number of evenly spaced interpolation points or nodes increases, a so-called oscillation near the ends of the interpolation domain arises which can be described as Runge's phenomenon. Unless a low-order polynomial approximation is employed, an even distribution of interpolation nodes is detrimental to the accuracy of the interpolation. This reason leads to approximate linear or quadratic shape functions to be assumed in FEM. To demonstrate potential effect of the interpolation, let's approximate the Runge function as

$$f(\xi) = \frac{1}{1 + 25\xi^2}$$

in a normalized interval [-1, 1] with 6^{th} order interpolating polynomial that passes through 6+1 evenly distributed data points. As the number of data points and thus the polynomial order increases, the interpolation worsens near the two ends of the

interpolation domain which is referred as Runge effect. This is an obvious effect as the interpolated polynomial is reconstructed from the evenly spaced data values that contributes equal attention to the middle and to the two ends of the interpolation domain,

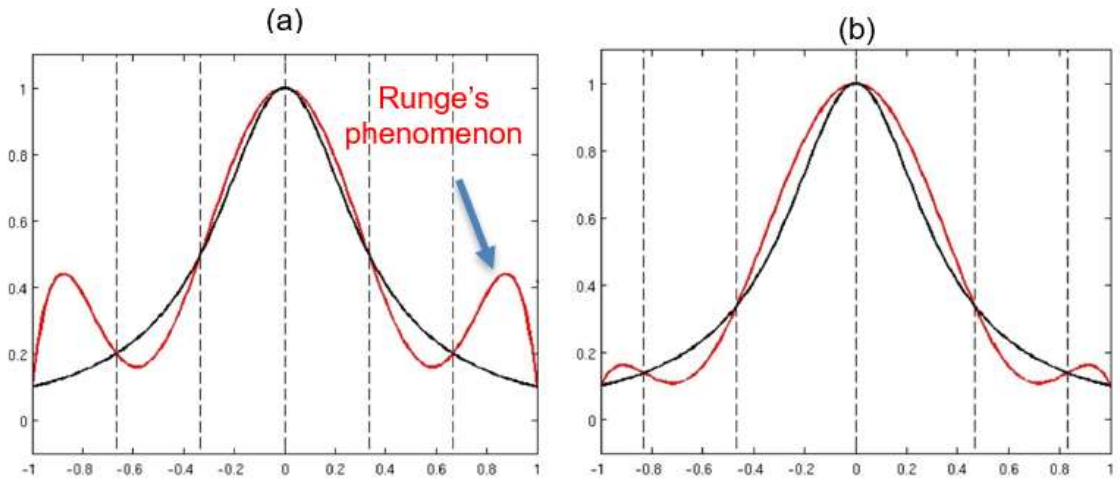

Figure 5.1: Plot of (a) 7-node interpolation functions corresponding to polynomial order 6 with evenly spaced nodal points, (b) 7-node interpolation functions corresponding to polynomial order 6 with nodal points at the roots of Gauss-Lobatto-Legendre polynomials.

insufficient information is provided beyond the boundaries of the interpolation domain. As a result, a much-deviated approximation is observed near the element boundaries as described in Figure 5.1(a). Therefore, as the polynomial order increases, results obtained from evenly spaced element interpolation nodes may significantly become sensitive to the numerical error of even fail, which is the case for FEM. In order to avoid the potential failure or incorrect assessment, a judicial placement of the interpolation nodes over each element to positions corresponding to the zeros of orthogonal polynomials can be utilized. In Figure 5.1(b), the nodes are located at the zeros of the Gauss-Lobatto-

Legendre polynomial. As the nodes are not evenly spaced, the Runge's effect is much lower at the two ends of the normalized element interval.

5.4 Types of SEM

The SEM method can be essentially of two types. Type I - SEM is a Frequency domain spectral element method [108] where the problem is solved at specific individual frequencies, we call FSEM. A loading function is essentially transformed (FFT) in to the frequency domain, and the problem of interest is solved in all discrete frequencies at specific frequency interval governed by the sampling rate of time in the Fourier domain. Next the response function from the problem of interest at all the frequencies are collected, and an inverse Fourier transform (IFFT) is conducted to retrieve the time domain signal. In Type I - SEM the wave functions obtained from the solution of the wave propagation equation are used as the element shape functions. Whereas, Type II SEM is a transient or direct time domain simulation method where the problem is solved in time domain utilizing the specific polynomial functions to express the quantity of interest inside the element and the nodal points are distributed at the zero points of that polynomial [109-112]. We call Type II – SEM a TSEM. Hence, the TSEM is essentially a type of FEM with specific element types that are designed based on the spectral wave mode shapes.

5.5 Problem Statement

An attenuative surface is required to simulate wave propagation and the solution of particle displacements need to be identified to prove the accuracy of the SEM. For this reason, a simple structural component made of 24-layer laminated composite plate has

been chosen to solve for wave propagation. Following Figure shows 24-ply laminated composite plate with fiber orientation of 24 layers are [0, 45, -45, 90, 90, -45, 45, 0]$_3$.

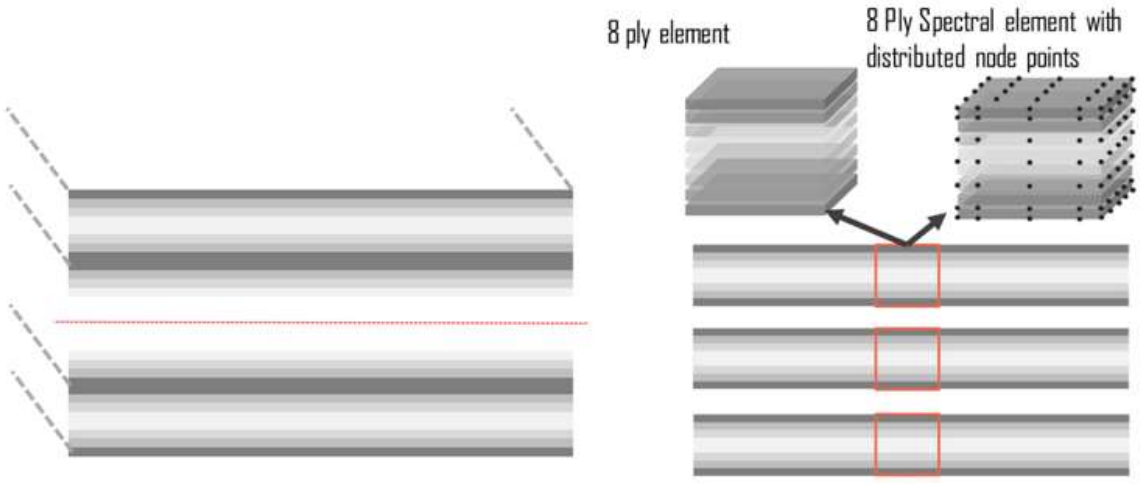

Figure 5.2: (Left) 24-ply composite structure. (right) 8-ply symmetric laminated part has been illustrated for simulation and discretization purpose.

For the implementation purpose, the symmetric 8-ply laminated part has been taken into consideration initially. A spectral discretization is performed to demonstrate its applicability. However, a mathematical formulation is required to proceed further.

5.6 Mathematical Formulation in 3D

In the case of wave propagation in 3D solids and structural mechanics problems, the fundamental objective is to find out an approximate solution as a form of displacement amplitudes at each material point. In both FEM and SEM, the material body is discretized into a finite number of elements. The profile of the displacements is assumed in a form to obtain approximate element displacements in the form of element equations. The equations obtained for each element are then assembled together with

adjoining elements to form the global finite or spectral element equation for the whole material domain. Equations thus created for the global material domain can be solved for the entire displacement field as a system of simultaneous linear algebraic equations.

The problem of interest herein is a wave propagation problem in laminated composite plate and the primary unknown variables in the governing differential equation are the displacement functions in three directions in the Cartesian coordinate system. The secondary variables subsequently are the strain and stress variables. The strong form of the problem equation requires a strong continuity on the unknown variables. Since obtaining the exact solution for a strong form of the system equation is usually difficult for this wave propagation problem, a weak form of the problem equation needs to be derived which is suitable for obtaining an approximate solution. The weak form can be derived using variational principles. For the type of our problem, following two forms of the variational principles are discussed:

A. Energy principles such as Hamiltonian principles: this can be categorized as a special form of the variational principle which is particularly suited for problems of the mechanics of solids and structures. While the principle of minimum potential energy is limited to static equilibrium of solids, Hamilton's principle is a generalization of the principle of virtual displacements to dynamics of solids.
B. Weighted residual methods such as Ritz method and Galerkin method: This is a more general mathematical tool applicable, in principle, for solving many kinds of partial differential equations.

5.7 Application of Hamiltonian Principle

Application of Hamilton's principle conveniently guarantee a combination of assumed set of displacements to produce the almost accurate solution for the system that is governed by the strong form of the system equations. The set of assumed displacements must satisfy the following three admissible displacement conditions:

1. The compatibility equations
2. The essential or the kinematic boundary conditions
3. The conditions at initial and final time

The equation of motion of the system discretized by spectral elements can be derived directly from the Lagrange equation. According to the Hamiltonian principle, the governing equation of a system can be written as

$$\frac{d}{dt}\left\{\frac{\partial L}{\partial \dot{q}}\right\} - \left\{\frac{\partial L}{\partial q}\right\} + \left\{\frac{\partial R}{\partial \dot{q}}\right\} = 0 \quad \text{.....(1)}$$

where, the L is the Lagrangian functional of a dynamic system which is the difference between the kinetic energy (T) and potential energy (Π_p), i.e., $L = T - \Pi_p$. Considering a most generic case where in NDE of a laminated composite plate, the plate will be subjected to the body and surface forces per unit volume. Hence, the kinetic energy (T), potential energy (Π_p) and the dissipation of energy (R) in the system can be written as

$$\begin{cases} T = \frac{1}{2}\int_V \rho \dot{\mathbf{U}}^T \dot{\mathbf{U}} dV \\ \Pi_p = \frac{1}{2}\int_V \boldsymbol{\varepsilon}^T \boldsymbol{\sigma} dV - \int_V \mathbf{U}^T \boldsymbol{\psi}_\Omega dV - \int_A \mathbf{U}^T \boldsymbol{\psi}_\Gamma dA \\ R = \frac{1}{2}\int_V \mu \dot{\mathbf{U}}^T \dot{\mathbf{U}} dV \end{cases} \quad \text{.....(2)}$$

Where ρ and μ represent the density and damping coefficient respectively. Also, $\boldsymbol{\psi}_{\Omega}$ and $\boldsymbol{\psi}_{\Gamma}$ denotes the volume and surface force vectors respectively. These force vectors are function of time. As discretized by the spectral elements, the unknown displacement function inside the element can be approximated by the shape functions and the nodal displacements, U_i^u, U_i^v, U_i^w, in the x, y and z mutually perpendicular direction at the i-th node point of the element. Hence, the displacements at any point (x,y,z) inside the element is the superposition of the shape function multiplied with the nodal displacements. The shape functions can be visualized as the basis functions and the nodal displacements as the contribution factor.

$$\begin{cases} u(x,y,z) = \sum_{i=1}^{m} N_i(x,y,z)U_i^u \\ v(x,y,z) = \sum_{i=1}^{m} N_i(x,y,z)U_i^v \\ w(x,y,z) = \sum_{i=1}^{m} N_i(x,y,z)U_i^w \end{cases} \quad \text{.....(3)}$$

In equation (3) the shape function used has m nodal points and thus there are m shape functions. As the shape functions are not the function of time, the time derivatives of the displacement functions, i.e. the velocity and accelerations will have same shape functions. The relationships could be written in the following simpler form if the

$$\mathbf{U}^e = [\mathbf{u}, \mathbf{v}, \mathbf{w}]^T, \mathbf{U}^e{}_i = [U_1^u, U_1^v, U_1^w, \ldots . U_m^u, U_m^v, U_m^w]^T$$

$$\begin{aligned} \mathbf{U}^e &= \mathbf{N}^e \mathbf{U}_i^e \\ \dot{\mathbf{U}}^e &= \mathbf{N}^e \dot{\mathbf{U}}_i^e \\ \ddot{\mathbf{U}}^e &= \mathbf{N}^e \ddot{\mathbf{U}}_i^e \end{aligned} \quad \text{.....(4)}$$

where, $\mathbf{N}^e$ is the shape function matrix. The superscript e in the equation (4) signifies the relation is valid in one element with designation e. Similarly, for that same element the strain (ε^e) and stress (σ^e) equations can be written as follows. The strain function inside

the element e will be divided in to two parts, linear and nonlinear. Considering both the linear and nonlinear part of the strain component the total strain inside the element will be

$$\boldsymbol{\varepsilon}^e = \boldsymbol{\Gamma}_l \mathbf{U}^e + \boldsymbol{\Gamma}_n \mathbf{U}^e \quad \text{.....(5)}$$

where,

$$\boldsymbol{\Gamma}_l = \begin{bmatrix} \frac{\partial}{\partial x} & 0 & 0 \\ 0 & \frac{\partial}{\partial y} & 0 \\ 0 & 0 & \frac{\partial}{\partial z} \\ \frac{\partial}{\partial y} & \frac{\partial}{\partial x} & 0 \\ 0 & \frac{\partial}{\partial z} & \frac{\partial}{\partial y} \\ \frac{\partial}{\partial z} & 0 & \frac{\partial}{\partial x} \end{bmatrix}, \quad \boldsymbol{\Gamma}_n = \boldsymbol{\Gamma}_n(U) = \frac{1}{2} \begin{bmatrix} (\partial_x \boldsymbol{U})^T \partial_x \\ (\partial_y \boldsymbol{U})^T \partial_y \\ (\partial_z \boldsymbol{U})^T \partial_z \\ (\partial_x \boldsymbol{U})^T \partial_y + (\partial_y \boldsymbol{U})^T \partial_x \\ (\partial_y \boldsymbol{U})^T \partial_z + (\partial_z \boldsymbol{U})^T \partial_y \\ (\partial_z \boldsymbol{U})^T \partial_x + (\partial_x \boldsymbol{U})^T \partial_z \end{bmatrix}$$

Substituting the equation (4) in the equation (5) we get

$$\boldsymbol{\varepsilon}^e = \boldsymbol{\Gamma}_l \mathbf{N}^e \boldsymbol{U}_i^e + \boldsymbol{\Gamma}_n \mathbf{N}^e \boldsymbol{U}_i^e = \mathbf{B}_l^e \boldsymbol{U}_i^e + \mathbf{B}_n^e \boldsymbol{U}_i^e = \mathbf{B}^e \boldsymbol{U}_i^e \quad \text{.....(6)}$$

The constitutive equation gives the relationship between the stress and strain in the material of a solid which is govern by the Hooke's law. Therefore, the stress equation for an element will be

$$\boldsymbol{\sigma}^e = \mathbb{C}^e \boldsymbol{\varepsilon}^e = \mathbb{C}^e \mathbf{B}^e \mathbf{U}_i^e \quad \text{.....(7)}$$

where, $\mathbb{C}^e$ is the representative constitutive property matrix of the element. Hence, it is apparent that it is not necessary to have same material properties for every element in the model. At every ply we could provide different material properties based on the fiber orientation. Similarly, degraded or damaged material properties could also be used for certain element to simulate the effect of material degradation on the ultrasonic wave signal obtained from the NDE of laminated composite material.

Once we have defined the stresses and strains in terms of displacements, putting (4) through (7) in (2), we get,

$$\begin{cases} T^e = \frac{1}{2}(\dot{\mathbf{U}}_n^e)^T \left[\int_{V^e} \rho(\mathbf{N}^e)^T \mathbf{N}^e dV^e\right] \dot{\mathbf{U}}_n^e \\ \Pi_p^e = \frac{1}{2}(\mathbf{U}_n^e)^T \left[\int_{V^e} (\mathbf{B}_l^e + \mathbf{B}_n^e)^T \mathbf{C}^e (\mathbf{B}_l^e + \mathbf{B}_n^e)^T dV^e\right] \mathbf{U}_n^e - (\mathbf{U}_n^e)^T \left[\int_{V^e} (\mathbf{N}^e)^T \boldsymbol{\psi}_\Omega dV^e + \int_{A^e} (\mathbf{N}^e)^T \boldsymbol{\psi}_\Gamma dA^e + \mathbf{f}_c^e\right] \\ R^e = \frac{1}{2}(\dot{\mathbf{U}}_n^e)^T \left[\int_{V^e} \mu(\mathbf{N}^e)^T \mathbf{N}^e dV^e\right] \dot{\mathbf{U}}_n^e \end{cases}$$

.....(8)

where, $\mathbf{f}_c^e$ in the potential energy term is the vector of point forces at the nodal points, if any. This force vector is also a function of time. The integral terms in (8), represents the characteristics matrices and vectors of spectral elements. Extracting the charecteristics mass matrix (**M**), stiffness matrix (**K**), damping matrix (**D**) and the force vectors (surface loads ($\mathbf{f}_A$) and body force or volume force ($\mathbf{f}_V$)) from the equation (8), we could write

$$\begin{cases} \mathbf{M}^e = \int_{V^e} \rho(\mathbf{N}^e)^T \mathbf{N}^e dV^e \\ \mathbf{K}^e = \int_{V^e} (\mathbf{B}_l^e + \mathbf{B}_n^e)^T \mathbb{C}^e (\mathbf{B}_l^e + \mathbf{B}_n^e)^T dV^e \\ \mathbf{D}^e = \int_{V^e} \mu(\mathbf{N}^e)^T \mathbf{N}^e dV^e \\ \mathbf{f}_\Omega^e = \int_{V^e} (\mathbf{N}^e)^T \boldsymbol{\psi}_\Omega dV^e \\ \mathbf{f}_\Gamma^e = \int_{A^e} (\mathbf{N}^e)^T \boldsymbol{\psi}_\Gamma dA^e \end{cases}$$

.....(9)

With the matrices in equation (9) we can write the kinetic energy, potential energy, and dissipation functions as follows. Please note that all the equations are written for a spectral element.

$$\begin{cases} T^e = \frac{1}{2}(\dot{\mathbf{U}}_n^e)^T \mathbf{M}^e \dot{\mathbf{U}}_n^e \\ \Pi_p^e = \frac{1}{2}(\mathbf{U}_n^e)^T \mathbf{K}^e \mathbf{U}_n^e - (\mathbf{U}_n^e)^T [\mathbf{f}_\Omega^e + \mathbf{f}_\Gamma^e + \mathbf{f}_c^e] \\ R^e = \frac{1}{2}(\dot{\mathbf{U}}_n^e)^T \mathbb{C}^e \dot{\mathbf{U}}_n^e \end{cases} \quad \text{.....(10)}$$

Now substituting the equation (10) into the equation (1), the governing dynamic equation for a spectral element can be written as

$$\mathbf{M}^e \ddot{\mathbf{q}}_n^e + \mathbf{D}^e \dot{\mathbf{q}}_n^e + \mathbf{K}^e \mathbf{q}_n^e = \mathbf{f}_{total}^e(t) \quad \text{.....(11)}$$

where, $\mathbf{f}_{total}^e(t) = \mathbf{f}_\Omega^e(t) + \mathbf{f}_\Gamma^e(t) + \mathbf{f}_c^e(t)$

After assembling the element terms for the global problem, we get the gobal governing equation interms of discretized problem with spectral elements.

$$\ddot{\mathbf{M}}\mathbf{q}_n + \mathbf{D}\dot{\mathbf{q}}_n + \mathbf{K}\mathbf{q}_n = \mathbf{f}_{total}(t) \quad \text{.....(12)}$$

The global mass matrix, damping matrix, stiffness matrix, the global displacement, global velocity and global acceleration functions, and the force functions in equation (12) can be further written as

$$\begin{cases} \mathbf{M} = \sum_{e=1}^{S} (\mathbf{P}^e)^T \mathbf{M}^e \mathbf{P}^e, \quad \mathbf{D} = \sum_{e=1}^{S} (\mathbf{P}^e)^T \mathbf{D}^e \mathbf{P}^e, \quad \mathbf{K} = \sum_{e=1}^{S} (\mathbf{P}^e)^T \mathbf{K}^e \mathbf{P}^e \\ \ddot{\mathbf{U}}_n = \sum_{e=1}^{S} (\mathbf{P}^e)^T \ddot{\mathbf{U}}_n^e, \quad \mathbf{U}_n = \sum_{e=1}^{S} (\mathbf{P}^e)^T \dot{\mathbf{U}}_n^e \\ \mathbf{U}_n = \sum_{e=1}^{S} (\mathbf{P}^e)^T \mathbf{U}_n^e, \quad \mathbf{f}_n = \sum_{e=1}^{S} (\mathbf{P}^e)^T \mathbf{f}_n^e \end{cases} \quad \text{.....(13)}$$

Where, S is the total number of spectral elements used in the formulation. The **P** matrix is composed of zeros and ones to assemble the elements for the global representation based on the topology of the element orientation. Further the boundary conditions are the necessary part to implement in the global model. Here in this problem the time domain displacement is provided on the top surface of the laminated composite plate. The

internal layers will have stress and displacement continuity conditions. The equation (12) can be solved using standard FEM explicit method.

5.8 Application of Weighted Residual Principle

The weighted residual principle does not require the knowledge of the principles of virtual displacements or total minimum potential energy but only needs the governing differential equations of the problem. For the plane elasticity problem of wave propagation in laminated composite plates, the three-dimensional equations of motion are the governing equations which are the strong form of the problem.

The equations of motion can be written as:

$$\frac{\partial \sigma_{11}}{\partial x_1} + \frac{\partial \sigma_{12}}{\partial x_2} + \frac{\partial \sigma_{13}}{\partial x_3} + f_1 = \rho \ddot{u} \quad \text{.....(14a)}$$

$$\frac{\partial \sigma_{21}}{\partial x_1} + \frac{\partial \sigma_{22}}{\partial x_2} + \frac{\partial \sigma_{23}}{\partial x_3} + f_2 = \rho \ddot{v} \quad \text{.....(14b)}$$

$$\frac{\partial \sigma_{31}}{\partial x_1} + \frac{\partial \sigma_{32}}{\partial x_2} + \frac{\partial \sigma_{33}}{\partial x_3} + f_3 = \rho \ddot{w} \quad \text{.....(14c)}$$

Due to stress symmetry, it can be stated that, $\sigma_{12} = \sigma_{21}$; $\sigma_{13} = \sigma_{31}$; $\sigma_{23} = \sigma_{32}$. Determining the stress parameters, generalized Hook's law can be utilized. From the generalized Hook's Law in 3D, we can write,

$$\begin{Bmatrix}\sigma_{11}\\ \sigma_{22}\\ \sigma_{33}\\ \sigma_{23}\\ \sigma_{31}\\ \sigma_{12}\end{Bmatrix} = \begin{bmatrix}\mathbb{C}_{11} & \mathbb{C}_{12} & \mathbb{C}_{13} & 0 & 0 & 0\\ \mathbb{C}_{21} & \mathbb{C}_{22} & \mathbb{C}_{23} & 0 & 0 & 0\\ \mathbb{C}_{31} & \mathbb{C}_{32} & \mathbb{C}_{33} & 0 & 0 & 0\\ 0 & 0 & 0 & \mathbb{C}_{44} & 0 & 0\\ 0 & 0 & 0 & 0 & \mathbb{C}_{55} & 0\\ 0 & 0 & 0 & 0 & 0 & \mathbb{C}_{66}\end{bmatrix} \begin{Bmatrix}\dfrac{\partial u}{\partial x_1}\\ \dfrac{\partial v}{\partial x_2}\\ \dfrac{\partial w}{\partial x_3}\\ \dfrac{1}{2}\left(\dfrac{\partial v}{\partial x_3}+\dfrac{\partial w}{\partial x_2}\right)\\ \dfrac{1}{2}\left(\dfrac{\partial w}{\partial x_1}+\dfrac{\partial u}{\partial x_3}\right)\\ \dfrac{1}{2}\left(\dfrac{\partial u}{\partial x_2}+\dfrac{\partial v}{\partial x_1}\right)\end{Bmatrix}$$

Now, determining each term of the stress parameters using Hook's laws, one can get,

$$\sigma_{11} = \mathbb{C}_{11}\frac{\partial u}{\partial x_1} + \mathbb{C}_{12}\frac{\partial v}{\partial x_2} + \mathbb{C}_{13}\frac{\partial w}{\partial x_3}$$

$$\sigma_{22} = \mathbb{C}_{21}\frac{\partial u}{\partial x_1} + \mathbb{C}_{22}\frac{\partial v}{\partial x_2} + \mathbb{C}_{23}\frac{\partial w}{\partial x_3}$$

$$\sigma_{33} = \mathbb{C}_{31}\frac{\partial u}{\partial x_1} + \mathbb{C}_{32}\frac{\partial v}{\partial x_2} + \mathbb{C}_{33}\frac{\partial w}{\partial x_3}$$

$$\sigma_{23} = \frac{1}{2}\mathbb{C}_{44}\left(\frac{\partial v}{\partial x_3}+\frac{\partial w}{\partial x_2}\right) = \sigma_{32}$$

$$\sigma_{31} = \frac{1}{2}\mathbb{C}_{55}\left(\frac{\partial w}{\partial x_1}+\frac{\partial u}{\partial x_3}\right) = \sigma_{13}$$

$$\sigma_{12} = \frac{1}{2}\mathbb{C}_{66}\left(\frac{\partial u}{\partial x_2}+\frac{\partial v}{\partial x_1}\right) = \sigma_{21}$$

Differentiating direct and shear stresses, it can be written,

$$\frac{\partial \sigma_{11}}{\partial x_1} = \frac{\partial}{\partial x_1}\left(\mathbb{C}_{11}\frac{\partial u}{\partial x_1} + \mathbb{C}_{12}\frac{\partial v}{\partial x_2} + \mathbb{C}_{13}\frac{\partial w}{\partial x_3}\right)$$

$$\frac{\partial \sigma_{22}}{\partial x_2} = \frac{\partial}{\partial x_2}\left(\mathbb{C}_{21}\frac{\partial u}{\partial x_1} + \mathbb{C}_{22}\frac{\partial v}{\partial x_2} + \mathbb{C}_{23}\frac{\partial w}{\partial x_3}\right)$$

$$\frac{\partial \sigma_{33}}{\partial x_3} = \frac{\partial}{\partial x_3}\left(\mathbb{C}_{31}\frac{\partial u}{\partial x_1} + \mathbb{C}_{32}\frac{\partial v}{\partial x_2} + \mathbb{C}_{33}\frac{\partial w}{\partial x_3}\right)$$

$$\frac{\partial \sigma_{12}}{\partial x_2} = \frac{1}{2}\frac{\partial}{\partial x_2}\mathbb{C}_{66}\left(\frac{\partial u}{\partial x_2} + \frac{\partial v}{\partial x_1}\right) \qquad \frac{\partial \sigma_{21}}{\partial x_1} = \frac{1}{2}\frac{\partial}{\partial x_1}\mathbb{C}_{66}\left(\frac{\partial u}{\partial x_2} + \frac{\partial v}{\partial x_1}\right)$$

$$\frac{\partial \sigma_{31}}{\partial x_1} = \frac{1}{2}\frac{\partial}{\partial x_1}\mathbb{C}_{55}\left(\frac{\partial w}{\partial x_1} + \frac{\partial u}{\partial x_3}\right) \qquad \frac{\partial \sigma_{13}}{\partial x_3} = \frac{1}{2}\frac{\partial}{\partial x_3}\mathbb{C}_{55}\left(\frac{\partial w}{\partial x_1} + \frac{\partial u}{\partial x_3}\right)$$

$$\frac{\partial \sigma_{23}}{\partial x_3} = \frac{1}{2}\frac{\partial}{\partial x_3}\mathbb{C}_{44}\left(\frac{\partial v}{\partial x_3} + \frac{\partial w}{\partial x_2}\right) \qquad \frac{\partial \sigma_{32}}{\partial x_2} = \frac{1}{2}\frac{\partial}{\partial x_2}\mathbb{C}\left(\frac{\partial v}{\partial x_3} + \frac{\partial w}{\partial x_2}\right)$$

Therefore, substituting these values in Eq 14, one can write,

$$-\frac{\partial}{\partial x_1}\left(\mathbb{C}_{11}\frac{\partial u}{\partial x_1} + \mathbb{C}_{12}\frac{\partial v}{\partial x_2} + \mathbb{C}_{13}\frac{\partial w}{\partial x_3}\right) - \frac{\partial}{\partial x_2}\mathbb{C}_{66}\left(\frac{\partial u}{\partial x_2} + \frac{\partial v}{\partial x_1}\right) - \frac{\partial}{\partial x_3}\mathbb{C}_{55}\left(\frac{\partial w}{\partial x_1} + \frac{\partial u}{\partial x_3}\right) =$$

$$f_1 - \rho\ddot{u} \quad \text{.....(15a)}$$

$$-\frac{\partial}{\partial x_1}\mathbb{C}_{66}\left(\frac{\partial u}{\partial x_2} + \frac{\partial v}{\partial x_1}\right) - \frac{\partial}{\partial x_2}\left(\mathbb{C}_{21}\frac{\partial u}{\partial x_1} + \mathbb{C}_{22}\frac{\partial v}{\partial x_2} + \mathbb{C}_{23}\frac{\partial w}{\partial x_3}\right) - \frac{\partial}{\partial x_3}\mathbb{C}_{44}\left(\frac{\partial v}{\partial x_3} + \frac{\partial w}{\partial x_2}\right) =$$

$$f_2 - \rho\ddot{v} \quad \text{.....(15b)}$$

$$-\frac{\partial}{\partial x_1}\mathbb{C}_{55}\left(\frac{\partial w}{\partial x_1} + \frac{\partial u}{\partial x_3}\right) - \frac{\partial}{\partial x_2}\mathbb{C}_{44}\left(\frac{\partial v}{\partial x_3} + \frac{\partial w}{\partial x_2}\right) - \frac{\partial}{\partial x_3}\left(\mathbb{C}_{31}\frac{\partial u}{\partial x_1} + \mathbb{C}_{32}\frac{\partial v}{\partial x_2} + \mathbb{C}_{33}\frac{\partial w}{\partial x_3}\right) =$$

$$f_3 - \rho\ddot{w} \quad \text{.....(15c)}$$

Which can be written as,

$$\mathbb{C}_{11}\frac{\partial^2 u}{\partial x^2} + \mathbb{C}_{12}\frac{\partial^2 v}{\partial x \partial y} + \mathbb{C}_{13}\frac{\partial^2 w}{\partial x \partial z} + \frac{1}{2}\mathbb{C}_{66}\left(\frac{\partial^2 u}{\partial y^2} + \frac{\partial^2 v}{\partial y \partial x}\right) + \frac{1}{2}\mathbb{C}_{55}\left(\frac{\partial^2 w}{\partial z \partial x} + \frac{\partial^2 u}{\partial z^2}\right)$$

$$+\rho\ddot{u} - f_1 = 0 \quad \text{.....(16a)}$$

$$\mathbb{C}_{21}\frac{\partial^2 u}{\partial y \partial x} + \mathbb{C}_{22}\frac{\partial^2 v}{\partial y^2} + \mathbb{C}_{23}\frac{\partial^2 w}{\partial y \partial z} + \frac{1}{2}\mathbb{C}_{66}\left(\frac{\partial^2 u}{\partial x \partial y} + \frac{\partial^2 v}{\partial x^2}\right) + \frac{1}{2}\mathbb{C}_{44}\left(\frac{\partial^2 v}{\partial z^2} + \frac{\partial^2 w}{\partial z \partial y}\right)$$

$$+\rho\ddot{v} - f_2 = 0 \quad \text{.....(16b)}$$

$$\mathbb{C}_{31}\frac{\partial^2 u}{\partial z \partial x} + \mathbb{C}_{32}\frac{\partial^2 v}{\partial z \partial y} + \mathbb{C}_{33}\frac{\partial^2 w}{\partial z^2} + \frac{1}{2}\mathbb{C}_{55}\left(\frac{\partial^2 w}{\partial x^2} + \frac{\partial^2 u}{\partial x \partial z}\right) + \frac{1}{2}\mathbb{C}_{44}\left(\frac{\partial^2 v}{\partial y \partial z} + \frac{\partial^2 w}{\partial y^2}\right)$$

$$+\rho\ddot{w} - f_3 = 0 \quad \text{.....(16c)}$$

Equation (15) or (16) are the strong form of the governing equations of a laminated composite plane elastic body undergoing small deformations. At this point, a weak formulation of these equations is determined. First, multiply equation (15a) with a weight function w_1, which is assumed to be differentiable once with respect to direction 1, 2 and 3, and then integrations over the element domain, Ω_e have been performed. This gives,

$$\int w_1 \left[-\frac{\partial}{\partial x_1}\left(\mathbb{C}_{11}\frac{\partial u}{\partial x_1} + \mathbb{C}_{12}\frac{\partial v}{\partial x_2} + \mathbb{C}_{13}\frac{\partial w}{\partial x_3}\right) - \frac{\partial}{\partial x_2}\mathbb{C}_{66}\left(\frac{\partial u}{\partial x_2} + \frac{\partial v}{\partial x_1}\right) - \frac{\partial}{\partial x_3}\mathbb{C}_{55}\left(\frac{\partial w}{\partial x_1} + \frac{\partial u}{\partial x_3}\right) + \rho\ddot{u} - f_1\right] d\mathbb{v} = 0 \quad \text{.....(17)}$$

Let's assume,

$$F_1 = \mathbb{C}_{11}\frac{\partial u}{\partial x_1} + \mathbb{C}_{12}\frac{\partial v}{\partial x_2} + \mathbb{C}_{13}\frac{\partial w}{\partial x_3}$$

$$F_2 = \mathbb{C}_{66}\frac{\partial u}{\partial x_2} + \mathbb{C}_{66}\frac{\partial v}{\partial x_1} \qquad \text{and}$$

$$F_3 = \mathbb{C}_{55}\frac{\partial w}{\partial x_1} + \mathbb{C}_{55}\frac{\partial u}{\partial x_3}$$

From (17a), it can be written as,

$$\int w_1 \left[-\frac{\partial}{\partial x_1}(F_1) - \frac{\partial}{\partial x_2}(F_2) - \frac{\partial}{\partial x_3}(F_3) + \rho\ddot{u} - f_1 \right] d\mathbb{v} = 0 \quad \text{.....(18a)}$$

Now, product of differentiation rule gives us,

$$\frac{\partial}{\partial x_1}(w_1 F_1) = \frac{\partial w_1}{\partial x_1} F_1 + w_1 \frac{\partial F_1}{\partial x_1} \quad \Rightarrow \quad -w_1 \frac{\partial F_1}{\partial x_1} = \frac{\partial w_1}{\partial x_1} F_1 - \frac{\partial}{\partial x_1}(w_1 F_1)$$

$$\frac{\partial}{\partial x_2}(w_1 F_2) = \frac{\partial w_1}{\partial x_2} F_2 + w_1 \frac{\partial F_2}{\partial x_2} \quad \Rightarrow \quad -w_1 \frac{\partial F_2}{\partial x_2} = \frac{\partial w_1}{\partial x_2} F_2 - \frac{\partial}{\partial x_2}(w_1 F_2)$$

$$\frac{\partial}{\partial x_3}(w_1 F_3) = \frac{\partial w_1}{\partial x_3} F_3 + w_1 \frac{\partial F_3}{\partial x_3} \quad \Rightarrow \quad -w_1 \frac{\partial F_3}{\partial x_3} = \frac{\partial w_1}{\partial x_3} F_3 - \frac{\partial}{\partial x_3}(w_1 F_3)$$

Using divergence theorem, one can get,

$$\int \frac{\partial}{\partial x_1}(w_1 F_1) dx dy dz = \oint w_1 F_1 n_1 d\mathcal{s}$$

$$\int \frac{\partial}{\partial x_2}(w_1 F_2) dx dy dz = \oint w_1 F_2 n_2 d\mathcal{s}$$

$$\int \frac{\partial}{\partial x_3}(w_1 F_3) dx dy dz = \oint w_1 F_3 n_3 d\mathcal{s}$$

Therefore,

$$-w_1 \frac{\partial F_1}{\partial x_1} = \frac{\partial w_1}{\partial x_1} F_1 - \oint w_1 F_1 n_1 d\mathcal{s}$$

$$-w_1 \frac{\partial F_2}{\partial x_2} = \frac{\partial w_1}{\partial x_2} F_2 - \oint w_1 F_2 n_2 d\mathcal{s}$$

$$-w_1 \frac{\partial F_3}{\partial x_3} = \frac{\partial w_1}{\partial x_3} F_3 - \oint w_1 F_3 n_3 d\mathcal{s}$$

Putting these values in Equation (18a), we get,

$$\frac{\partial w_1}{\partial x_1}F_1 d\mathbb{v} - \oint w_1 F_1 n_1 d\mathcal{s} + \frac{\partial w_1}{\partial x_2}F_2 d\mathbb{v} - \oint w_1 F_2 n_2 d\mathcal{s} + \frac{\partial w_1}{\partial x_3}F_3 d\mathbb{v} - \oint w_1 F_3 n_3 d\mathcal{s}$$

$$+ \int w_1 \rho \ddot{u}\ d\mathbb{v} - \int w_1 f_1\, d\mathbb{v} = 0$$

$$\Rightarrow \int [\frac{\partial w_1}{\partial x_1}\left(\mathbb{C}_{11}\frac{\partial u}{\partial x_1} + \mathbb{C}_{12}\frac{\partial v}{\partial x_2} + \mathbb{C}_{13}\frac{\partial w}{\partial x_3}\right) + \frac{\partial w_1}{\partial x_2}\left(\mathbb{C}_{66}\frac{\partial u}{\partial x_2} + \mathbb{C}_{66}\frac{\partial v}{\partial x_1}\right) + \frac{\partial w_1}{\partial x_3}\left(\mathbb{C}_{55}\frac{\partial w}{\partial x_1} + \mathbb{C}_{55}\frac{\partial u}{\partial x_3}\right) + w_1\rho\ddot{u} - w_1 f_1\,]\, d\mathbb{v} - \oint w_1 \left[n_1\left(\mathbb{C}_{11}\frac{\partial u}{\partial x_1} + \mathbb{C}_{12}\frac{\partial v}{\partial x_2} + \mathbb{C}_{13}\frac{\partial w}{\partial x_3}\right) + n_2\left(\mathbb{C}_{66}\frac{\partial u}{\partial x_2} + \mathbb{C}_{66}\frac{\partial v}{\partial x_1}\right) + n_3\left(\mathbb{C}_{55}\frac{\partial w}{\partial x_1} + \mathbb{C}_{55}\frac{\partial u}{\partial x_3}\right)\right] d\mathcal{s} = 0$$

$$\Rightarrow \int [\mathbb{C}_{11}\frac{\partial w_1}{\partial x_1}\frac{\partial u}{\partial x_1} + \mathbb{C}_{12}\frac{\partial w_1}{\partial x_1}\frac{\partial v}{\partial x_2} + \mathbb{C}_{13}\frac{\partial w_1}{\partial x_1}\frac{\partial w}{\partial x_3} + \mathbb{C}_{66}\frac{\partial w_1}{\partial x_2}\frac{\partial u}{\partial x_2} + \mathbb{C}_{66}\frac{\partial w_1}{\partial x_2}\frac{\partial v}{\partial x_1} + \mathbb{C}_{55}\frac{\partial w_1}{\partial x_3}\frac{\partial w}{\partial x_1} + \mathbb{C}_{55}\frac{\partial w_1}{\partial x_3}\frac{\partial u}{\partial x_3} + w_1\rho\ddot{u} - w_1 f_1\,]\, d\mathbb{v} - \oint w_1 \left[n_1\left(\mathbb{C}_{11}\frac{\partial u}{\partial x_1} + \mathbb{C}_{12}\frac{\partial v}{\partial x_2} + \mathbb{C}_{13}\frac{\partial w}{\partial x_3}\right) + n_2\left(\mathbb{C}_{66}\frac{\partial u}{\partial x_2} + \mathbb{C}_{66}\frac{\partial v}{\partial x_1}\right) + n_3\left(\mathbb{C}_{55}\frac{\partial w}{\partial x_1} + \mathbb{C}_{55}\frac{\partial u}{\partial x_3}\right)\right] d\mathcal{s} = 0$$

Which can be deduced as,

$$\Rightarrow \int \left[\mathbb{C}_{11}\frac{\partial w_1}{\partial x_1}\frac{\partial u}{\partial x_1} + \mathbb{C}_{12}\frac{\partial w_1}{\partial x_1}\frac{\partial v}{\partial x_2} + \mathbb{C}_{13}\frac{\partial w_1}{\partial x_1}\frac{\partial w}{\partial x_3} + \mathbb{C}_{66}\frac{\partial w_1}{\partial x_2}\frac{\partial u}{\partial x_2} + \mathbb{C}_{66}\frac{\partial w_1}{\partial x_2}\frac{\partial v}{\partial x_1} + \mathbb{C}_{55}\frac{\partial w_1}{\partial x_3}\frac{\partial w}{\partial x_1} + \mathbb{C}_{55}\frac{\partial w_1}{\partial x_3}\frac{\partial u}{\partial x_3} + w_1\rho\ddot{u} - w_1 f_1\,\right] d\mathbb{v} - \oint w_1 t_1 d\mathcal{s} = 0 \quad \text{.....(19a)}$$

Where,

$$t_1 = n_1\left(\mathbb{C}_{11}\frac{\partial u}{\partial x_1} + \mathbb{C}_{12}\frac{\partial v}{\partial x_2} + \mathbb{C}_{13}\frac{\partial w}{\partial x_3}\right) + n_2\left(\mathbb{C}_{66}\frac{\partial u}{\partial x_2} + \mathbb{C}_{66}\frac{\partial v}{\partial x_1}\right) + n_3\left(\mathbb{C}_{55}\frac{\partial w}{\partial x_1} + \mathbb{C}_{55}\frac{\partial u}{\partial x_3}\right)$$

Similarly, from equation (15b) and (15c), it can be written as,

$$\int \left[\mathbb{C}_{21}\frac{\partial w_2}{\partial x_2}\frac{\partial u}{\partial x_1} + \mathbb{C}_{22}\frac{\partial w_2}{\partial x_2}\frac{\partial v}{\partial x_2} + \mathbb{C}_{23}\frac{\partial w_2}{\partial x_2}\frac{\partial w}{\partial x_3} + \mathbb{C}_{66}\frac{\partial w_2}{\partial x_1}\frac{\partial u}{\partial x_2} + \mathbb{C}_{66}\frac{\partial w_2}{\partial x_1}\frac{\partial v}{\partial x_1} + \mathbb{C}_{44}\frac{\partial w_2}{\partial x_3}\frac{\partial v}{\partial x_3} + \mathbb{C}_{44}\frac{\partial w_2}{\partial x_3}\frac{\partial w}{\partial x_2} + w_2\rho\ddot{v} - w_2 f_2\right] d\mathbb{v} - \oint w_2 t_2 d\mathcal{s} = 0 \quad \text{.....(19b)}$$

and

$$\int \left[\mathbb{C}_{31}\frac{\partial w_3}{\partial x_3}\frac{\partial u}{\partial x_1} + \mathbb{C}_{32}\frac{\partial w_3}{\partial x_3}\frac{\partial v}{\partial x_2} + \mathbb{C}_{33}\frac{\partial w_3}{\partial x_3}\frac{\partial w}{\partial x_3} + \mathbb{C}_{55}\frac{\partial w_3}{\partial x_1}\frac{\partial w}{\partial x_1} + \mathbb{C}_{55}\frac{\partial w_3}{\partial x_1}\frac{\partial u}{\partial x_3} + \mathbb{C}_{44}\frac{\partial w_3}{\partial x_2}\frac{\partial v}{\partial x_3} + \mathbb{C}_{44}\frac{\partial w_3}{\partial x_2}\frac{\partial w}{\partial x_2} + w_3\rho\ddot{w} - w_3 f_3\right] d\mathbb{v} - \oint w_3 t_3 d\mathcal{s} = 0 \quad \text{.....(19c)}$$

Equation (19) gives the weak form of the governing equations. In this stage, a spectral element approximation is introduced which is a standard procedure similar to FEM. The displacement at the element level can be approximated as,

$$u = \sum u_j^e(t)\,\psi_j^e(1,2,3)$$

$$v = \sum v_j^e(t)\psi_j^e(1,2,3)$$

$$w = \sum w_j^e(t)\psi_j^e(1,2,3)$$

Or, it can be expressed as,

$$U = \begin{Bmatrix} u^e \\ v^e \\ w^e \end{Bmatrix} = \begin{bmatrix} \psi_1^e & 0 & 0 & \psi_2^e & .. & .. & \psi_n^e & 0 & 0 \\ 0 & \psi_1^e & 0 & 0 & \psi_2^e & 0 & .... & \psi_n^e & 0 \\ 0 & 0 & \psi_1^e & 0 & 0 & \psi_2^e & .. & .. & \psi_n^e \end{bmatrix} \begin{Bmatrix} u_1^e \\ v_1^e \\ w_1^e \\ u_2^e \\ v_2^e \\ w_2^e \\ \vdots \\ \vdots \\ u_n^e \\ v_n^e \\ w_n^e \end{Bmatrix}$$

Using Galekin approximation, one can set $w_1 = \psi_i$, $w_2 = \psi_i$ and $w_3 = \psi_i$ in equation 19, and thus the i^{th} equation over an element (therefore, superscript 'e' has been omitted) can be written as follows:

$$\int[\left(\mathbb{C}_{11}\frac{\partial\psi_i}{\partial x_1}\frac{\partial\psi_j}{\partial x_1}+\ \mathbb{C}_{66}\frac{\partial\psi_i}{\partial x_2}\frac{\partial\psi_j}{\partial x_2}\ +\ \mathbb{C}_{55}\frac{\partial\psi_i}{\partial x_3}\frac{\partial\psi_j}{\partial x_3}\right)u_j+\ \left(\mathbb{C}_{12}\frac{\partial\psi_i}{\partial x_1}\frac{\partial\psi_j}{\partial x_2}+\mathbb{C}_{66}\frac{\partial\psi_i}{\partial x_2}\frac{\partial\psi_j}{\partial x_1}\right)v_j+$$

$$\left(\mathbb{C}_{13}\frac{\partial\psi_i}{\partial x_1}\frac{\partial\psi_j}{\partial x_3}+\mathbb{C}_{55}\frac{\partial\psi_i}{\partial x_3}\frac{\partial\psi_j}{\partial x_1}\right)w_j+\ \ \psi_i\rho\ddot{u}-\psi_i f_1\ ]\,d\mathbb{v}-\oint\psi_i t_1 d\mathcal{s}=0$$

$$\int[\left(\ \mathbb{C}_{21}\frac{\partial\psi_i}{\partial x_2}\frac{\partial\psi_j}{\partial x_1}+\ \mathbb{C}_{66}\frac{\partial\psi_i}{\partial x_1}\frac{\partial\psi_j}{\partial x_2}\right)u_j+\ \left(\mathbb{C}_{66}\frac{\partial\psi_i}{\partial x_1}\frac{\partial\psi_j}{\partial x_1}+\ \mathbb{C}_{22}\frac{\partial\psi_i}{\partial x_2}\frac{\partial\psi_j}{\partial x_2}\ +\ \mathbb{C}_{44}\frac{\partial\psi_i}{\partial z}\frac{\partial\psi_j}{\partial x_3}\right)v_j+$$

$$\left(\ \mathbb{C}_{23}\frac{\partial\psi_i}{\partial x_2}\frac{\partial\psi_j}{\partial x_3}+\ \mathbb{C}_{44}\frac{\partial\psi_i}{\partial x_3}\frac{\partial\psi_j}{\partial x_2}\right)w_j+\psi_i\rho\ddot{v}-\psi_i f_2\ ]\,d\mathbb{v}-\oint\psi_i t_2 d\mathcal{s}=0$$

And,

$$\int[\left(\ \mathbb{C}_{31}\frac{\partial\psi_i}{\partial x_3}\frac{\partial\psi_j}{\partial x_1}+\ \mathbb{C}_{55}\frac{\partial\psi_i}{\partial x_1}\frac{\partial\psi_j}{\partial x_3}\right)u_j+\left(\ \mathbb{C}_{32}\frac{\partial\psi_i}{\partial x_3}\frac{\partial\psi_j}{\partial x_2}+\ \mathbb{C}_{44}\frac{\partial\psi_i}{\partial x_2}\frac{\partial\psi_j}{\partial x_3}\right)v_j+\ \left(\mathbb{C}_{55}\frac{\partial\psi_i}{\partial x_1}\frac{\partial\psi_j}{\partial x_1}\ +\right.$$

$$\left.\mathbb{C}_{44}\frac{\partial\psi_i}{\partial x_2}\frac{\partial\psi_j}{\partial x_2}+\mathbb{C}_{33}\frac{\partial\psi_i}{\partial x_3}\frac{\partial\psi_j}{\partial x_3}\right)w_j+\psi_i\rho\ddot{w}-\psi_i f_3\ ]\,d\mathbb{v}-\oint\psi_i t_3 d\mathcal{s}=0$$

In these three equations, let's assume,

$$K_{ij}^{11}=\ \mathbb{C}_{11}\frac{\partial\psi_i}{\partial x_1}\frac{\partial\psi_j}{\partial x_1}+\ \mathbb{C}_{66}\frac{\partial\psi_i}{\partial x_2}\frac{\partial\psi_j}{\partial x_2}\ +\ \mathbb{C}_{55}\frac{\partial\psi_i}{\partial x_3}\frac{\partial\psi_j}{\partial x_3}$$

$$K_{ij}^{12}=\ \mathbb{C}_{12}\frac{\partial\psi_i}{\partial x_1}\frac{\partial\psi_j}{\partial x_2}+\mathbb{C}_{66}\frac{\partial\psi_i}{\partial x_2}\frac{\partial\psi_j}{\partial x_1}$$

$$K_{ij}^{13}=\mathbb{C}_{13}\frac{\partial\psi_i}{\partial x_1}\frac{\partial\psi_j}{\partial x_3}+\mathbb{C}_{55}\frac{\partial\psi_i}{\partial x_3}\frac{\partial\psi_j}{\partial x_1}$$

$$K_{ij}^{21}=\ \mathbb{C}_{21}\frac{\partial\psi_i}{\partial x_2}\frac{\partial\psi_j}{\partial x_1}+\ \mathbb{C}_{66}\frac{\partial\psi_i}{\partial x_1}\frac{\partial\psi_j}{\partial x_2};$$

$$K_{ij}^{22}=\mathbb{C}_{66}\frac{\partial\psi_i}{\partial x_1}\frac{\partial\psi_j}{\partial x_1}+\ \mathbb{C}_{22}\frac{\partial\psi_i}{\partial x_2}\frac{\partial\psi_j}{\partial x_2}\ +\ \mathbb{C}_{44}\frac{\partial\psi_i}{\partial z}\frac{\partial\psi_j}{\partial x_3}$$

$$K_{ij}^{23}=\ \mathbb{C}_{23}\frac{\partial\psi_i}{\partial x_2}\frac{\partial\psi_j}{\partial x_3}+\ \mathbb{C}_{44}\frac{\partial\psi_i}{\partial x_3}\frac{\partial\psi_j}{\partial x_2}$$

$$K_{ij}^{31} = \mathbb{C}\frac{\partial\psi_i}{\partial x_3}\frac{\partial\psi_j}{\partial x_1} + \mathbb{C}_{55}\frac{\partial\psi_i}{\partial x_1}\frac{\partial\psi_j}{\partial x_3};$$

$$K_{ij}^{32} = \mathbb{C}_{32}\frac{\partial\psi_i}{\partial x_3}\frac{\partial\psi_j}{\partial x_2} + \mathbb{C}_{44}\frac{\partial\psi_i}{\partial x_2}\frac{\partial\psi_j}{\partial x_3};$$

$$K_{ij}^{33} = \mathbb{C}_{55}\frac{\partial\psi_i}{\partial x_1}\frac{\partial\psi_j}{\partial x_1} + \mathbb{C}_{44}\frac{\partial\psi_i}{\partial x_2}\frac{\partial\psi_j}{\partial x_2} + \mathbb{C}_{33}\frac{\partial\psi_i}{\partial x_3}\frac{\partial\psi_j}{\partial x_3}$$

$$M_{ij} = \int \rho\,\psi_i\psi_j\,d\mathbb{v} \qquad F_i = \int \psi_i\,d\mathbb{v} \qquad Q_i = \oint \psi_i d\mathbb{s}$$

Therefore, by substituting them, it can be written as,

$$\begin{bmatrix} K_{ij}^{11} & K_{ij}^{12} & K_{ij}^{13} \\ K_{ij}^{21} & K_{ij}^{22} & K_{ij}^{23} \\ K_{ij}^{31} & K_{ij}^{32} & K_{ij}^{33} \end{bmatrix} \begin{Bmatrix} \{u\} \\ \{v\} \\ \{w\} \end{Bmatrix} + \begin{bmatrix} M_{ij} & 0 & 0 \\ 0 & M_{ij} & 0 \\ 0 & 0 & M_{ij} \end{bmatrix} \begin{Bmatrix} \{\ddot{u}\} \\ \{\ddot{v}\} \\ \{\ddot{w}\} \end{Bmatrix} = F_i \begin{Bmatrix} f_1 \\ f_2 \\ f_3 \end{Bmatrix} + Q_i \begin{Bmatrix} t_1 \\ t_2 \\ t_3 \end{Bmatrix}$$

In matrix form,

$$[K^e]\{U^e\} + [M^e]\{\ddot{U}^e\} = \{F^e\} + \{Q^e\} \quad \text{.....(20)}$$

Once the element equations are formulated, a standard FE explicit solution method can be utilized after assembling them into global equations.

5.9 Spectral Shape Function

Assumption of shape function with appropriate order of the polynomial makes SEM different from FEM. As a generic comment, it can be said that in all numerical methods the dependent variables in the governing differential equations are always unknown. But it is necessary to assume the pattern of the solution and plug or enforce the solution into the governing equation to solve for the unknown coefficients by satisfying the boundary and interface conditions. In FEM, the solution pattern is enforced in the

element level. When the solution of an unknown function say $f(x)$ is assumed, then the function is expressed in terms of superposition of few basis functions with specific properties when the basis functions contributes to the solution with their respective contribution factors. The specific property of the basis function is their orthogonality with respect to a suitable weight function. As an example, the function $f(x)$ can be written as a superposition of n basis functions (b_i) and their respective contribution factors (f_i).

$$f(x) = b_1 f_1 + b_2 f_2 + b_2 f_2 + b_3 f_3 \ldots\ldots + b_n f_n \text{ ....(21)}$$

Using a Taylor series expansion of n-th order of the same function within a certain zone in the neighborhood of a, one can write,

$$f(x) = f(a) + \frac{x-a}{1!} f^{(1)}(a) + \frac{(f-a)^2}{2!} f^2(a) + \cdots + \frac{(x-a)^n}{n!} f^{(n)}(a) \text{..................(22)}$$

Comparing the equation (8) and the equation (9), it can be visualized that they are spin off from the similar concept. Taylor series expansion helps any unknown function to expand into a polynomial function and thus the polynomial orders can be assumed to be the basis functions and the derivatives of the unknown function at the pivotal point ‘a’ can be assumed to be the contribution factors. The n-th basis function and Lagrange residual in the Taylor series expansion can be written as,

$$b_n = \frac{(x-a)^n}{(n)!};$$

$$\frac{\mathrm{d}b_n}{\mathrm{dx}} = \frac{(x-a)^{n+1}}{(n+1)!} f^{(n+1)}(a) \text{ ....(23)}$$

The basis functions can also be the trigonometric functions and if the sin and cos functions are used as basis functions, the expansion of the series will be called the Fourier

series expansion. Irrespective of the method the polynomial expansions are imposed at the element level in FEM and unknown functions inside the element are approximated. In most of the polynomial expansions, the nodal points where the unknown function values are zero at the element boundaries are always equally spaced. However, as per the discussion in the previous section to avoid the Runge phenomenon it is necessary to use polynomial functions where the nodal points are not uniformly distributed at the element boundary. Hence, the basis function has to be defined such a way that the above requirements are satisfied. In this work, orthogonal Lobatto polynomials are utilized.

5.10 LOBATTO POLYNOMIALS

The basis functions in the Lobatto polynomial is described as the first order derivative of the Legendre polynomial. Using Rodrigues's formula, the Legendre polynomial can be written as:

$$P_n(\xi) = \frac{1}{2^n n!}\frac{d^n}{d\xi^n}(\xi^2 - 1)^n \text{ , n= 0, 1, 2, …k…. n} \quad \text{.....(24)}$$

Hence the Lobatto polynomial can be written as,

$$L_n(\xi) = \frac{d}{d\xi}P_{n+1}(\xi) \quad \text{n=0,1, 2, ….k …. N} \quad \text{.....(25)}$$

The k-th order Lobatto polynomial will be

$$L_k(\xi) = \frac{1}{2^{k+1}(k+1)!}\frac{d^{k+2}}{d\xi^{k+2}}(\xi^2 - 1)^{k+1} \quad \text{.....(26)}$$

As discussed in the previous section that the specific property of the basis functions is the orthogonality of the function with suitable weight function. Hence, it was found that the

Lobatto polynomials are orthogonal with respect to the weight function $(1-\xi^2)$ in the domain [-1,+1].

$$\int_{-1}^{1} L_i(\xi)L_j(\xi)(1-\xi^2)d\xi = \frac{2(i+1)(i+2)}{(2i+3)}\delta_{ij}\ ,\ \text{i, j = 0, 1, 2.....(27)}$$

where, δ_{ij} is the well-known Kronecker delta function.

In an n-th order spectral element the internal node points are distributed at the roots of the $(n-2)$-th order of Lobatto polynomial $(L_{n-2}(\xi))$ because other two end points are placed at -1 and at +1, respectively. The coordinates of the spectral element nodes are solved from the following equation,

$$(1-\xi^2)L_{n-2}(\xi) = 0 \quad n = 2,3, \ldots$$

5.11 Lobatto Integration Quadrature

In practice, the integration terms stated in the mass matrix and stiffness matrix of either equation (11) or (20) are computed by numerical methods. An appropriate quadrature rule is important to get the most effective results from the integration and overall solution of the problem. If Lobatto polynomial is used, the Lobatto quadrature should be used. Whereas for Chebyshev and Laguerre polynomials the Gauss quadrature rule and Gauss-Laguerre quadrature rules are to be used, respectively. Here in this problem we will use Lobatto polynomial and will used the Lobatto quadrature rule. Since numerical implementations are performed in element level before assembling them in global equations, an element co-ordinate system is preferable to implement any of the integration quadrature. Hence, the shape function matrices are mapped to the normalized coordinate system and the Jacobian matrix is introduced. Say for example the integral of

any function $\mathbf{H}(x, y, z)$ over the element volume can be transformed to a non-dimensional coordinate system of ξ, η, β each defined between [-1,+1] and the result of the integral will be identical. We can write this case as follows

$$I^e = \int_\Omega \mathbf{H}(x, y, z) dV^e = \int_{-1}^{+1} \int_{-1}^{+1} \int_{-1}^{+1} \mathbf{H}(\xi, \eta, \beta) \det(\mathbf{J})\, d\xi\, d\eta\, d\beta \quad \text{.....(28)}$$

Where, $\mathbf{J}$ is the Jacobi matrix calculated as follows

$$\mathbf{J} = \begin{bmatrix} \frac{\partial x}{\partial \xi} & \frac{\partial y}{\partial \xi} & \frac{\partial z}{\partial \xi} \\ \frac{\partial x}{\partial \eta} & \frac{\partial y}{\partial \eta} & \frac{\partial z}{\partial \eta} \\ \frac{\partial x}{\partial \beta} & \frac{\partial y}{\partial \beta} & \frac{\partial z}{\partial \beta} \end{bmatrix} \quad \text{.....(29)}$$

The derivative of the spectral shape functions of an m-noded spectral element can be calculated as follows

$$\begin{Bmatrix} \frac{\partial N_i}{\partial x} \\ \frac{\partial N_i}{\partial y} \\ \frac{\partial N_i}{\partial z} \end{Bmatrix} = \mathbf{J}^{-1} \begin{Bmatrix} \frac{\partial N_i}{\partial \xi} \\ \frac{\partial N_i}{\partial \eta} \\ \frac{\partial N_i}{\partial \beta} \end{Bmatrix} \quad i = 1, \dots\dots, m \quad \text{.....(30)}$$

The quadrature rule to calculate the integral in equation (28) can be written in a generalized form as follows

$$I^e = \int_{-1}^{+1} \int_{-1}^{+1} \int_{-1}^{+1} \mathbf{H}(\xi, \eta, \beta) \det(\mathbf{J})\, d\xi\, d\eta\, d\beta$$

$$= \sum_{i=1}^{n_1} \sum_{j=1}^{n_2} \sum_{k=1}^{n_3} \omega_i \omega_j \omega_k \mathbf{H}(\phi_i, \phi_j, \phi_k) \det(\mathbf{J}) \quad \text{.....(31)}$$

Where, $\omega_i, \omega_j, \omega_k$ are the weight factor and ϕ_i, ϕ_j, ϕ_k are the abscissae where the function values are obtained. The values depend on the number of quadrature points

(n_1, n_2, n_3) used in the quadrature rule. The numerical integration in Lobatto quadrature use the following formula

$$\int_{-1}^{+1} H(\xi)d\xi = \frac{2}{n(n-1)}[H(-1) + H(+1)] + \sum_{i=1}^{n-2} \omega_i H(\phi_i) + E_r \quad \text{.....(32)}$$

where, n is the number of quadrature points. Weight factors can be calculated as follows

$$\omega_i = \frac{2}{q(q-1)P_{q-1}(a_i)^2}, \; i = 1,2, \dots \dots, n \quad \text{.....(33)}$$

The coordinate of the abscissae can be calculated from the root of the equation

$$(1 - \phi_i^2)\frac{d}{d\xi}P_{n-1}(\phi_i) = 0, \; i = 1,2, \dots \dots \dots, n \quad \text{.....(34)}$$

Where, $P_{n-1}(\xi)$ is the Legendre polynomial of order $n-1$. The error in the equation (32) is

$$E_r = \frac{n(n-1)^2 2^{2n-1}\left((n-2)!\right)^4}{(2n-1)\left((2n-2)!\right)^3} H^{(2n-2)}(\eta), \quad \eta \epsilon [-1, +1] \quad \text{.....(35)}$$

CHAPTER 6

COMPUTER IMPLEMENTATION OF SPECTRAL ELEMENT METHOD

6.1 INTRODUCTION

A computer code has been developed using MATLAB to solve wave propagation problem using the formulation presented above by translating the mathematical language into computer programming language. The algorithm and the list of variables are described below in figure 6.1.

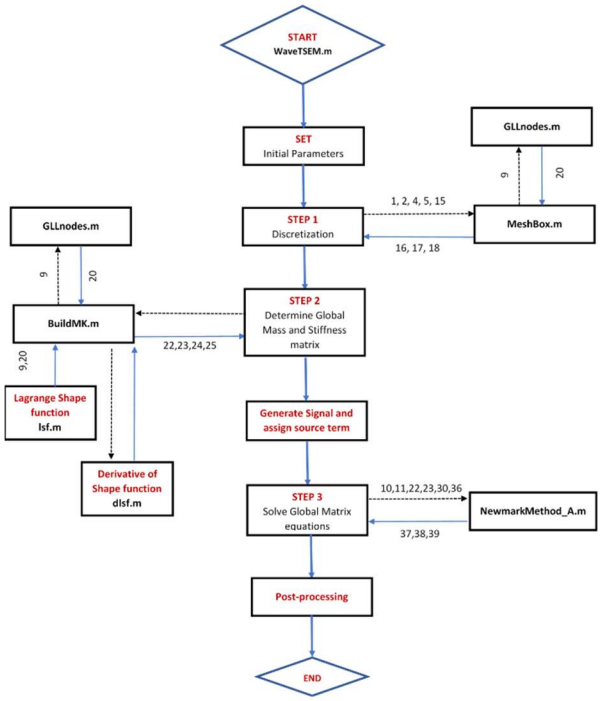

Figure 6.1: Algorithm for solving wave propagation problem using SEM.

The Table 6.1 shows the list of variables and their number used in the flow chart.

Table 6.1: List of variables used to write SEM code.

Parameters / Variables Description	**Name**	**Identifier**
Geometry Length in x-direction (in m)	LX	1
Geometry Length in y-direction (in m)	LY	2
Geometry Length in z-direction (in m)	LZ	3
Number of elements in x-direction	NELX	4
Number of elements in y-direction	NELY	5
Density (kg/m^3)	rho	6
Denity x z-direction length	mu	7
Stiffness (GPa)	C	8
Degree of polynomial	P	9
Time step (nano-second)	dt	10
Total number of time step	NT	11
STEP 1: Spectral Element Mesh Generation		
Length per element in x-direction	dxe	12
Length per element in y-direction	dye	13
Total Number of Element	NEL	14
Number of GLL nodes per element	NGLL	15
X coordinate of Global geometry	x	16
Y coordinate of Global geometry	y	17
Local to Global node map	iglob	18

Number of global nodes	nglob	19
Node location in normalized coordinate	xgll	20
Integration weights using Lobatto quadrature	wgll	21
STEP 2: Determination of Global Mass and Stiffness matrix		
Global Mass matrix	M	22
Global Stiffness matrix	K	23
Global x-coordinates in ascending order	x1	24
Global y-coordinates in ascending order	y1	25
Values of shape function in xi-coordinate	Sx	26
Values of shape function in eta-coordinate	Sy	27
Derivative of shape function in xi-coordinate	DSx	28
Derivative of shape function in eta-coordinate	DSy	29
Damping matrix in the system	Damping	30
Central frequency	CentFreq	31
Number of tones burst cycle	NumCycles	32
Total time	TotTim	33
X-coordinate of force location	Fx	34
Y-coordinate of force location	Fy	35
Applied force	F	36
STEP 3: Implicit Solver – Newmark Beta Method		
Displacement	disp	37
Velocity	vel	38
Acceleration	accl	39

6.2 Initial Simulation Parameters

The purpose of computer implementation is to demonstrate the effectiveness of SEM to evaluate wave propagation in multilayer composite structure. Therefore, a suitable type of elements is chosen as the building block in formulating SEM algorithm. All initial parameters are computed in three-dimensional space. The geometry and the material properties of the composite structure are declared in this section. In addition, the number of elements in three-dimensional space are optimized based on available computational resources. To facilitate master spectral element, the code is formulated based on Nth order approximate polynomials in each of the available dimensions. For example, 3rd, 5th and 7th order polynomial can be approximated in direction 1, 2 and 3 respectively. This information is required to discretize the domain, determining shape functions and formulating stiffness and mass matrix.

6.3 Discretization of Problem Domain

The first step of the Spectral element method is to discretize the problem domain into three-dimensional elements. Each of these elements are composed of group of geometrical nodes. The combination of these element nodes constitutes a larger set of unique global nodes. In SEM, several types of elements can be assumed. The element types can be Tetrahedral, Pyramidal, Prismatic and Hexahedral (brick). In this study, Hexahedral brick elements are chosen considering simple geometry of the problem domain. As stated earlier, in SEM, the node points are located at the roots of Gauss-Lobatto-Legendre (GLL) polynomials, unlike FEM, these node points are not spaced equally as shown in Figure 6.2.

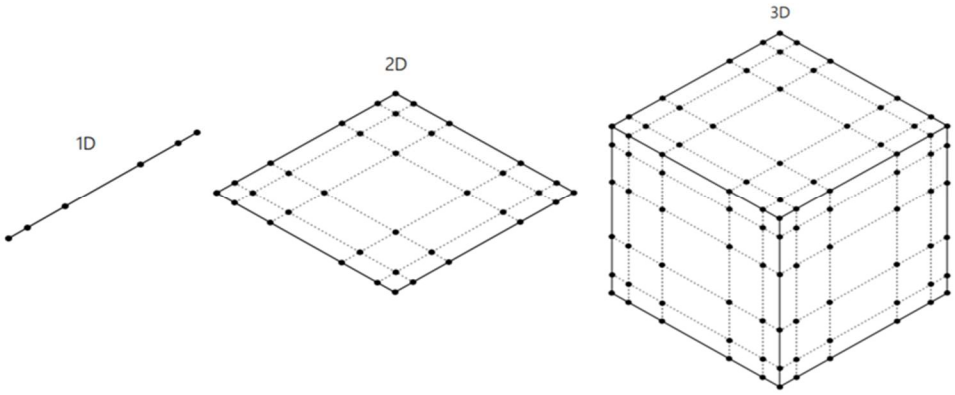

Figure 6.2: Node distribution in Spectral Element methods which are roots of 5th order GLL polynomials for 1D, 2D and 3D cases.

A master brick element is mapped to a parent domain (ξ, η, ζ) with standard interval, [-1, 1], [-1, 1] and [-1, 1]. A subroutine is used to generate the element mapping and the discretization points. The global co-ordinates of the node points are calculated based on the master element local node points. While calculating the global node points, the overlapping faces of the adjoining faces are assigned to the sharing elements and thus C0 continuity is ensured. A typical example of a discretized domain with 2 x 2 x 2 elements having 4 x 3 x 2 GLL points in each element is shown in Figure 6.3. It can be observed that a total of eight elements are present in the problem domain. Out of these eight elements, four elements are located on the front row (two in front top and two in front bottom) and rest fours are located on the back row (two in back top and two in back bottom). The origin of this domain is considered at node 1 of element 1. To maintain C0 continuity, during discretization, specific node points of each elements are designated to be shared by the node points of adjoining elements. For example, in Figure 6.3, YZ face of element 1 that contains nodes 4, 8, 12, 16, 20 and 24 are shared by YZ face of element 2. Similarly, XZ face of element 2 (blue) is shared by XZ face (blue) of element 6. Thus,

element 1 is connected with elements 2, 3, 4, 5 and 6 either by face or by edge. Therefore, it can be seen that a pair of elements shares a face to each other. In a global sense, all the green rectangles are in one YZ plane and similarly blue rectangles of each element of Figure 6.3 are in other YZ plane. While discretizing, a variable is formulated that maps the local numbering of the computational nodes to their global (non-redundant) numbering. Based on this map, the three-dimensional coordinates of global node points are determined. Formulation of this map is helpful to identify each points of the global domain and assign any properties as required by the problem statement.

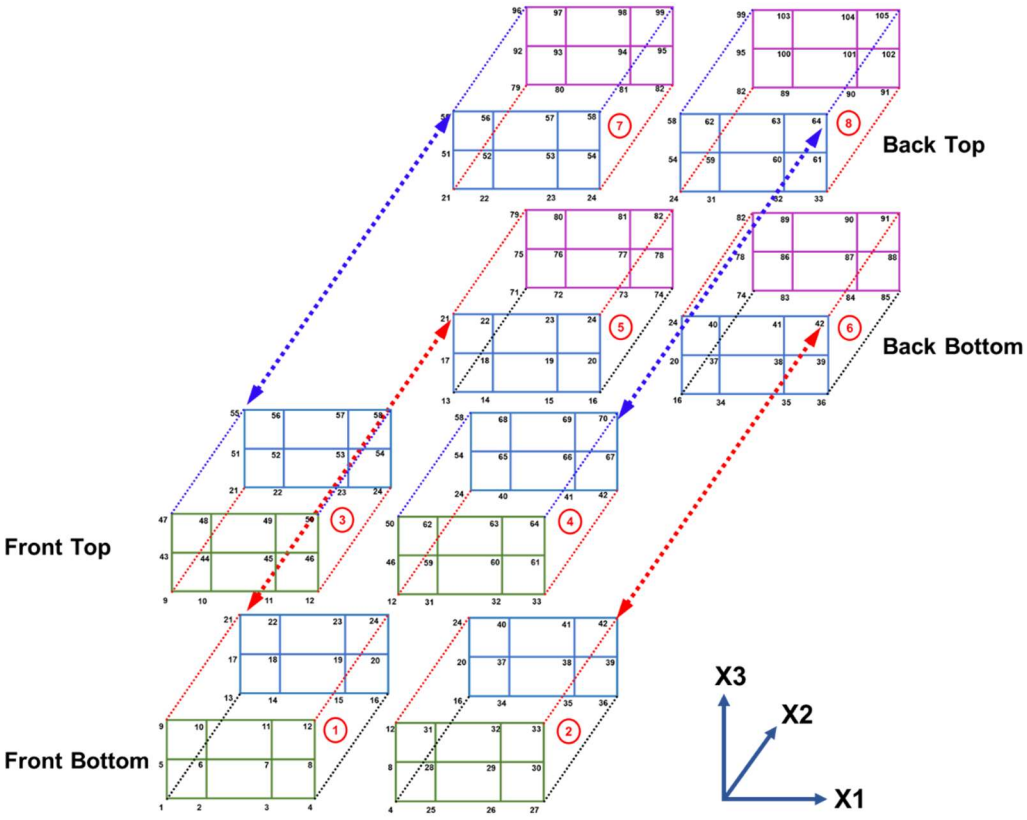

Figure 6.3: Example of 2 x 2 x 2 elements having 4 x 3 x 2 GLL points in each element.

6.4 Determination Global Mass And Stiffness Matrix

This is relatively a long step where local components of the element stiffness and mass matrices are determined. Determination of local mass and stiffness matrices allows us to formulate element equation applicable to each type of elements used in discretization process. In this study, the implementation of computer application is based on the element equation formulated for master hexahedral element which is described in section 6.2. The concluding equation, eq. 20, of this section describes the general element equation. Each of the components of this equation is required to determined and formulated for computer application.

Local Stiffness matrix: The element stiffness matrix is denoted by $[K^e]$ which has nine components. For brevity, evaluation of one component is described in this article. The first component is

$$K_{ij}^{11} = \int \left[\mathbb{C}_{11} \frac{\partial \psi_i}{\partial x_1} \frac{\partial \psi_j}{\partial x_1} + \mathbb{C}_{66} \frac{\partial \psi_i}{\partial x_2} \frac{\partial \psi_j}{\partial x_2} + \mathbb{C}_{55} \frac{\partial \psi_i}{\partial x_3} \frac{\partial \psi_j}{\partial x_3} \right] d\mathbb{v}$$

Which has an integral form on its right-hand side. This integral is computed by numerical methods using Lobatto integration quadrature. Therefore, in numerical method, the value of K_{ij}^{11} can be calculated as,

$$\int \left[\mathbb{C}_{11} \frac{\partial \psi_i}{\partial x_1} \frac{\partial \psi_j}{\partial x_1} + \mathbb{C}_{66} \frac{\partial \psi_i}{\partial x_2} \frac{\partial \psi_j}{\partial x_2} + \mathbb{C}_{55} \frac{\partial \psi_i}{\partial x_3} \frac{\partial \psi_j}{\partial x_3} \right] d\mathbb{v}$$

$$= \iiint_{-1}^{1} \left[\mathbb{C}_{11} \frac{\partial \psi_i}{\partial x_1} \frac{\partial \psi_j}{\partial x_1} + \mathbb{C}_{66} \frac{\partial \psi_i}{\partial x_2} \frac{\partial \psi_j}{\partial x_2} + \mathbb{C}_{55} \frac{\partial \psi_i}{\partial x_3} \frac{\partial \psi_j}{\partial x_3} \right] dx_1 dx_2 dx_3$$

$$= \sum_{p=1}^{m}\sum_{p=1}^{n}\sum_{p=1}^{k}\left[\mathbb{C}_{11}\frac{\partial\psi_i}{\partial\xi}\frac{\partial\psi_j}{\partial\xi}\omega_{\xi p}\omega_{\eta p}\omega_{\zeta p}J_{x_1x_1} + \mathbb{C}_{66}\frac{\partial\psi_i}{\partial\eta}\frac{\partial\psi_j}{\partial\eta}\omega_{\xi p}\omega_{\eta p}\omega_{\zeta p}J_{x_2x_2} + \mathbb{C}_{55}\frac{\partial\psi_i}{\partial\zeta}\frac{\partial\psi_j}{\partial\zeta}\omega_{\xi p}\omega_{\eta p}\omega_{\zeta p}J_{x_3x_3}\right]$$

And M_{ij}^{11} can be calculated as,

$$M_{ij}^{11} = \int \rho\,\psi_i\psi_j\,d\mathbb{v}$$

$$= \iiint_{-1}^{1} \rho\,\psi_i\psi_j dx_1 dx_2 dx_3$$

$$= \sum_{p=1}^{m}\sum_{p=1}^{n}\sum_{p=1}^{k}\rho\psi_i\psi_j\omega_{\xi p}\omega_{\eta p}\omega_{\zeta p}J_{x_1x_1}$$

Where,

$\mathbb{C}_{11}, \mathbb{C}_{66}$ and $\mathbb{C}_{55}$ are components of the elastic properties and ρ is the density of the material properties defined in initial parameter steps.

ψ_i and ψ_j are the three-dimensional shape function.

$\frac{\partial\psi_i}{\partial x_1}$ and $\frac{\partial\psi_j}{\partial x_1}$ are the first derivative of the three-dimensional shape function calculated at each of the node points on the each of the elements.

$\omega_{\xi p}$, $\omega_{\eta p}$ and $\omega_{\zeta p}$ are the integration weights at each of the normalized axis.

$J_{x_1x_1}$ is the determinant of the Jacobian matrix to transfer coordinates.

In next paragraphs, calculation of above parameters is discussed.

Material properties: The components of the elasticity matrix are calculated at each element nodes. Since the material properties of an anisotropic material depend on the direction of the coordinate axis, an element wise evaluation of the elasticity matrix is a

pivotal approach to determine its components. Therefore, the nodal map determined in discretization step is used to determine the material properties at each node point. Before evaluating local stiffness matrix, a local variable is created by collecting the node points that have similar material properties. In this study, multilayer composite specimen is assumed to solve the wave propagation problem. Therefore, a transversely isotropic material properties is utilized in each layer. As these layers are stacked in X_3 direction, layer thickness is used as the distance where material properties remain same. Similarly, the density of the material can be determined at each node points following the same approach. In this study, invariant density is assumed in entire problem domain.

Shape functions: The shape functions are determined using the Lagrange interpolation functions of appropriate order. The Lagrange interpolation functions associated with hexahedral elements can be obtained from the corresponding one-dimensional Lagrange interpolation functions by taking the tensor products of the X_1 direction interpolation functions with the tensor product of the X_2 and X_3 directional interpolation functions. The N^{th} order Lagrange interpolation functions can be associated with the given abscissas, ξ. The Lagrange interpolation functions associated with the i^{th} abscissa can be defined in terms of the abscissas of the data points, ξ, where j = 1, 2, 3, ... …, N+1 and denoted as $L_{N,i}(\xi)$. In line with the properties of shape functions, $L_{N,i}(\xi)$ is equal to zero at all data points except at the i^{th} data point where it becomes to one which is same as Kronecker's delta, δ_{ij}. Therefore, the Lagrange interpolation functions is as follows,

$$L_{N,i}(\xi) = \frac{(\xi-\xi_1)(\xi-\xi_2)\dots\dots(\xi-\xi_{i-1})(\xi-\xi_{i+1})\dots\dots(\xi-\xi_N)(\xi-\xi_{N+1})}{(\xi_i-\xi_1)(\xi_i-\xi_2)\dots\dots(\xi_i-\xi_{i-1})(\xi_i-\xi_{i+1})\dots\dots(\xi_i-\xi_N)(\xi_i-\xi_{N+1})}$$

If one-dimensional shape functions in three coordinate axes are denoted as $\psi_{\xi,m}$, $\psi_{\eta,n}$ and $\psi_{\zeta,k}$, the tensor product of three vectors can be performed as follows,

$\psi_{2d,(m,n)} = \psi_{\xi,m} \otimes \psi_{\eta,n}{}^{T}$ which is a matrix and $\otimes$ denotes tensor product.

This needs to be reshaped as a vector before performing next tensor product which will yield three-dimensional shape functions.

$$\psi_{2d,(mn,1)} = reshape\ (\psi_{2d,mxn})$$

$$\psi_{3d} = \psi_{2d,(mn,1)} \otimes \psi_{\zeta,k}{}^{T}$$

First derivative of the shape functions: The first derivative of the one-dimensional shape functions can be determined using the following expressions [113],

$$\frac{d\psi_{1d,ij}}{d\xi} = \frac{1}{\xi_j - \xi_i} \frac{(\xi_j - \xi_1)(\xi_j - \xi_2) \dots\dots (\xi_j - \xi_{j-1})(\xi_j - \xi_{j+1}) \dots\dots (\xi_j - \xi_{m+1})}{(\xi_i - \xi_1)(\xi_i - \xi_2) \dots\dots (\xi_i - \xi_{i-1})(\xi_j - \xi_{i+1}) \dots\dots (\xi_i - \xi_{m+1})}$$

For $i \neq j$, and

$$\frac{d\psi_{1d,ii}}{d\xi} = \frac{1}{\xi_i - \xi_1} + \cdots + \frac{1}{\xi_i - \xi_{i-1}} + \frac{1}{\xi_i - \xi_{i+1}} + \cdots + \frac{1}{\xi_i - \xi_{m+1}}$$

In case of first derivative of three-dimensional shape functions, it can be calculated as,

$$\frac{d\psi(\xi,\eta,\zeta)}{d\xi} = \frac{d\psi(\xi)}{d\xi} \otimes \psi(\eta)^{T} \otimes \psi(\zeta)^{T}$$

Similarly, first derivative of other two three-dimensional shape functions can be determined as follows,

$$\frac{d\psi(\xi,\eta,\zeta)}{d\eta} = \psi(\xi) \otimes \frac{d\psi(\eta)^{T}}{d\eta} \otimes \psi(\zeta)^{T}$$

$$\frac{d\psi(\xi,\eta,\zeta)}{d\zeta} = \psi(\xi) \otimes \psi(\eta)^T \otimes \frac{d\psi(\zeta)^T}{d\zeta}$$

Integration weights: Integration weights are determined to perform Lobatto integration quadrature. Therefore, following relationships are utilized to calculate the integration weights for an mth order one-dimensional shape functions.

$\omega_m = \frac{2}{k(k+1)} \frac{1}{L_k^2(\xi)}$ where, m = 2, … …., k and L_k is a Legendre polynomial.

Coordinate transfer: The node points of a hexahedral element are expressed in normalized (ξ, η, ζ) coordinates. The sole objective of utilizing these coordinates is to evaluate the integrands of equation 20 numerically. This helps to evaluate this integrand for an arbitrary master element which can be adjusted based on the location of any element in the entire domain in global coordinates. However, evaluation of the integrand for a master element should be such that there exist no spurious gaps between elements and no element overlaps persists.

The three-dimensional shape function, $\psi_i^e(\xi, \eta, \zeta)$ can be expressed can be expressed in terms of local coordinates ξ, η and ζ and by the chain rule of differentiation it can be written as,

$$\frac{d\psi_i^e}{d\xi} = \frac{d\psi_i^e}{dx_1}\frac{dx_1}{d\xi} + \frac{d\psi_i^e}{dx_2}\frac{dx_2}{d\xi} + \frac{d\psi_i^e}{dx_3}\frac{dx_3}{d\xi}$$

$$\frac{d\psi_i^e}{d\eta} = \frac{d\psi_i^e}{dx_1}\frac{dx_1}{d\eta} + \frac{d\psi_i^e}{dx_2}\frac{dx_2}{d\eta} + \frac{d\psi_i^e}{dx_3}\frac{dx_3}{d\eta}$$

$$\frac{d\psi_i^e}{d\zeta} = \frac{d\psi_i^e}{dx_1}\frac{dx_1}{d\zeta} + \frac{d\psi_i^e}{dx_2}\frac{dx_2}{d\zeta} + \frac{d\psi_i^e}{dx_3}\frac{dx_3}{d\zeta}$$

In matrix form,

$$\begin{Bmatrix} \frac{d\psi_i^e}{d\xi} \\ \frac{d\psi_i^e}{d\eta} \\ \frac{d\psi_i^e}{d\zeta} \end{Bmatrix} = \begin{bmatrix} \frac{dx_1}{d\xi} & \frac{dx_2}{d\xi} & \frac{dx_3}{d\xi} \\ \frac{dx_1}{d\eta} & \frac{dx_2}{d\eta} & \frac{dx_3}{d\eta} \\ \frac{dx_1}{d\zeta} & \frac{dx_2}{d\zeta} & \frac{dx_3}{d\zeta} \end{bmatrix} \begin{Bmatrix} \frac{d\psi_i^e}{dx_1} \\ \frac{d\psi_i^e}{dx_2} \\ \frac{d\psi_i^e}{dx_3} \end{Bmatrix}$$

This gives the relationship between the derivatives of three-dimensional shape function ψ_i^e with respect to the global and local coordinates. Here, the matrix can be defned as the Jacobian matrix of the transformation,

$$[J] = \begin{bmatrix} \frac{dx_1}{d\xi} & \frac{dx_2}{d\xi} & \frac{dx_3}{d\xi} \\ \frac{dx_1}{d\eta} & \frac{dx_2}{d\eta} & \frac{dx_3}{d\eta} \\ \frac{dx_1}{d\zeta} & \frac{dx_2}{d\zeta} & \frac{dx_3}{d\zeta} \end{bmatrix}$$

Determinant of the Jacobian matrix can be calculated as,

$$\text{Det } [J] = \frac{dx_1}{d\xi} \ \frac{dx_2}{d\eta} \ \frac{dx_3}{d\zeta} \text{ as} \qquad \frac{dx_2}{d\xi} = 0, \frac{dx_3}{d\xi} = 0, \frac{dx_1}{d\eta} = 0, \text{ etc.}$$

An example of determining, $J_{x_1x_1}$ which transforms first derivative of three-dimensional shape functions with respect to x_1, x_2 and x_3 is as follows,

$$\frac{\partial\psi_i}{\partial x_1}\frac{\partial\psi_j}{\partial x_1}dx_1dx_2dx_3 = \frac{\partial\psi_i}{\partial\xi}\frac{\partial\xi}{\partial x_1}\frac{\partial\psi_j}{\partial\xi}\frac{\partial\xi}{\partial x_1} \ \frac{\partial x_1}{\partial\xi}\,\partial\xi\frac{\partial x_2}{\partial\eta}\,\partial\eta\frac{\partial x_3}{\partial\zeta}\,\partial\zeta$$

$$= \frac{\partial\psi_i}{\partial\xi}\frac{\partial\psi_j}{\partial\xi}\,\partial\xi\partial\eta\partial\zeta \ \frac{\partial\xi}{\partial x_1}\frac{\partial\xi}{\partial x_1} \ \frac{\partial x_1}{\partial\xi}\frac{\partial x_2}{\partial\eta}\frac{\partial x_3}{\partial\zeta}$$

$$= \frac{\partial \psi_i}{\partial \xi}\frac{\partial \psi_j}{\partial \xi}\,\partial\xi\partial\eta\partial\zeta \quad \frac{\left(\frac{\partial x_1 \partial x_2 \partial x_3}{\partial \xi \;\partial \eta \;\partial \zeta}\right)}{\frac{\partial x_1}{\partial \xi}\frac{\partial x_1}{\partial \xi}}$$

$$= \frac{\partial \psi_i}{\partial \xi}\frac{\partial \psi_j}{\partial \xi}\,\partial\xi\partial\eta\partial\zeta \quad J_{x_1x_1}$$

Therefore, $J_{x_1x_1} = \frac{\left(\frac{\partial x_1 \partial x_2 \partial x_3}{\partial \xi \;\partial \eta \;\partial \zeta}\right)}{\frac{\partial x_1}{\partial \xi}\frac{\partial x_1}{\partial \xi}}$

Similarly, $J_{x_1x_2}$ can be calculated as, $J_{x_1x_2} = \frac{\left(\frac{\partial x_1 \partial x_2 \partial x_3}{\partial \xi \;\partial \eta \;\partial \zeta}\right)}{\frac{\partial x_1}{\partial \xi}\frac{\partial x_2}{\partial \eta}}$

Assembly of local stiffness matrix into global stiffness matrix:

Assembly of local stiffness matrix to global stiffness matrix is similar to Finite Element Method. In this article, assembly of local stiffness matrix with two hexahedral elements are described. Once the local stiffness matrix is determined, each component of the local stiffness matrix is assembled in the global stiffness matrix following two basic principles,

A. Continuity of primary variables

B. Balance of secondary variables.

As, in next step, the global equations are solved using a suitable solution method, the global equation takes the form of

$$[K]\{U\} + [M]\{\ddot{U}\} = \{F\} \quad \text{.....(36)}$$

Where,

$[K]$ = Global Stiffness matrix

$[M]$ = Global mass matrix

$\{U\}$ = Primary variable which is displacement in wave propagation problem

$\{\ddot{U}\}$ = Second derivative of primary variable with respect to time

$\{F\}$ = Secondary variable which is applied force with frequency range.

In three-dimensional problem, the primary variable has three degree of freedom which, therefore, consists of three mutually perpendicular values at each geometric node points. It means that, for each nodal point, three equations are needed to determine the primary variable. Therefore, at each node point,

$$U = f(u, v, w)$$

where, u, v, w are the displacements along X_1, X_2 and X_3 directions, respectively.

In this study, the global displacement vector, which contains displacements of all nodes, is arranged in following fashion,

$$\{U\} = \begin{Bmatrix} u_1^1 \\ v_1^1 \\ w_1^1 \\ \vdots \\ u_n^1 \\ v_n^1 \\ w_n^1 \\ \cdot \\ \cdot \\ u_1^e \\ \vdots \\ w_n^e \end{Bmatrix} \quad \text{.....(37)}$$

Where, u_1^e,.., w_n^e denotes the displacements of e[th] elements for all of its node points. It can be noted that the nodal map contains element wise nodal positions while the global displacement vector assumed in equation 37 contains the displacements in global sequence. Fulfilment of global displacement requirements necessitates the global stiffness and mass matrices to be assembled in global nodal sequence. An example of this assembly method is described as follows.

Consider two hexahedral elements having two node points in each axis direction. Therefore, each of the elements has eight (8) node points as shown in Figure 6.4.

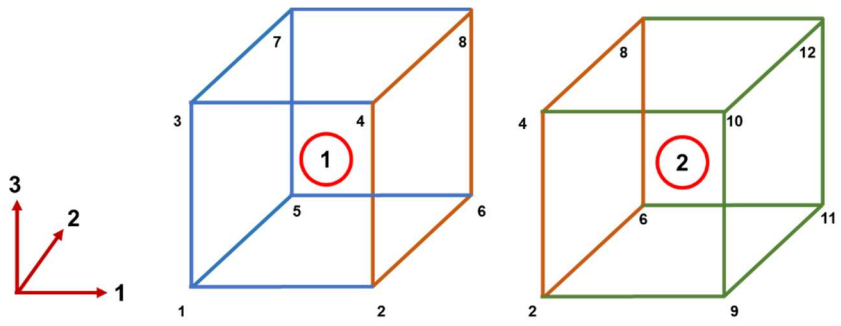

Figure 6.4: Global node points of two adjoining elements having two nodes at each axis direction.

Since each of the node point has three degree of freedom, the global displacement vector consists of 12 x 3 = 24 displacement values. Therefore, the global stiffness matrix should consist of 24 rows and 24 columns. This 24 x 24 square matrix gets its data values from its local counterparts. The local stiffness matrix of element 1 can be computed using the method described in 'Local Stiffness matrix' section.

As observed in Figure 6.4, the element 1 has 8 nodes labeled 1, 2, 3, 4, 5, 6, 7, 8 and element 2 has 8 nodes labeled 2, 9, 4, 10, 6, 11, 8, 12. In global SEM equations, there exists 3x12 or 36 values of the displacement vectors. The assigned indexes of the global displacement vector are described in Figure 6.5. Note that, first, second and third indexes of each node are assigned as direction 1, 2 and 3 respectively.

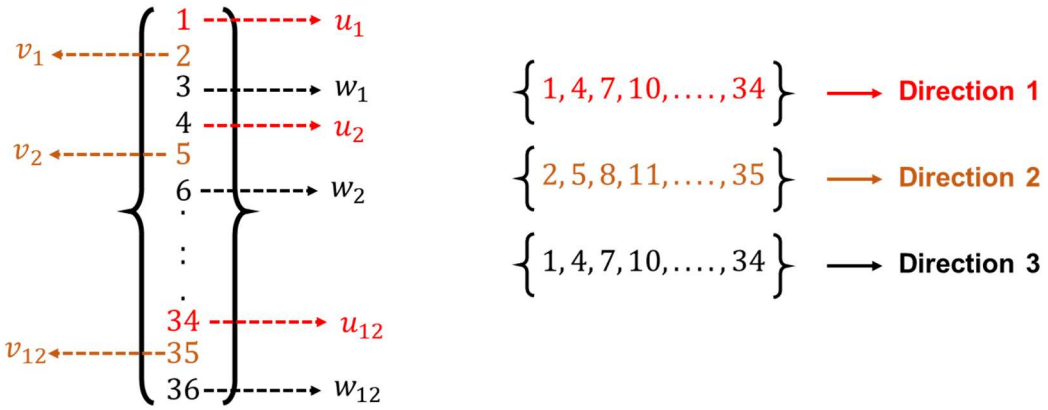

Figure 6.5: Global displacement vector having values in direction 1, 2 and 3.

Therefore, the global stiffness matrix contains 36 rows and 36 columns which need to be filled in by the local stiffness matrices of the elements. Since each element has 8 nodes, the local stiffness matrix contains 24 rows and 24 columns due to three degree of freedom in each node.

Therefore, the components of the local stiffness matrix for element 1,

$$[K_{11}^{1}] = \begin{bmatrix} K_{11}^{1,11} & K_{11}^{1,12} & K_{11}^{1,13} & K_{11}^{1,14} & K_{11}^{1,15} & K_{11}^{1,16} & K_{11}^{1,17} & K_{11}^{1,18} \\ K_{11}^{1,21} & K_{11}^{1,22} & K_{11}^{1,23} & K_{11}^{1,24} & K_{11}^{1,25} & K_{11}^{1,26} & K_{11}^{1,27} & K_{11}^{1,28} \\ \vdots & \vdots & \vdots & \vdots & \vdots & \vdots & \vdots & \vdots \\ \vdots & \vdots & \vdots & \vdots & \vdots & \vdots & \vdots & \vdots \\ K_{11}^{1,81} & K_{11}^{1,82} & K_{11}^{1,83} & K_{11}^{1,84} & K_{11}^{1,85} & K_{11}^{1,86} & K_{11}^{1,87} & K_{11}^{1,88} \end{bmatrix}$$

$$[K_{12}^{1}] = \begin{bmatrix} K_{12}^{1,11} & K_{12}^{1,12} & K_{12}^{1,13} & K_{12}^{1,14} & K_{12}^{1,15} & K_{12}^{1,16} & K_{12}^{1,17} & K_{12}^{1,18} \\ K_{12}^{1,21} & K_{12}^{1,22} & K_{12}^{1,23} & K_{12}^{1,24} & K_{12}^{1,25} & K_{12}^{1,26} & K_{12}^{1,27} & K_{12}^{1,28} \\ \vdots & \vdots & \vdots & \vdots & \vdots & \vdots & \vdots & \vdots \\ \vdots & \vdots & \vdots & \vdots & \vdots & \vdots & \vdots & \vdots \\ K_{12}^{1,81} & K_{12}^{1,82} & K_{12}^{1,83} & K_{12}^{1,84} & K_{12}^{1,85} & K_{12}^{1,86} & K_{12}^{1,87} & K_{12}^{1,88} \end{bmatrix}$$

$$\cdots \quad \cdots$$

$$[K_{33}^{1}] = \begin{bmatrix} K_{33}^{1,11} & K_{33}^{1,12} & K_{33}^{1,13} & K_{33}^{1,14} & K_{33}^{1,15} & K_{33}^{1,16} & K_{33}^{1,17} & K_{33}^{1,18} \\ K_{33}^{1,21} & K_{33}^{1,22} & K_{33}^{1,23} & K_{33}^{1,24} & K_{33}^{1,25} & K_{33}^{1,26} & K_{33}^{1,27} & K_{33}^{1,28} \\ \vdots & \vdots & \vdots & \vdots & \vdots & \vdots & \vdots & \vdots \\ \vdots & \vdots & \vdots & \vdots & \vdots & \vdots & \vdots & \vdots \\ K_{33}^{1,81} & K_{33}^{1,82} & K_{33}^{1,83} & K_{33}^{1,84} & K_{33}^{1,85} & K_{33}^{1,86} & K_{33}^{1,87} & K_{33}^{1,88} \end{bmatrix}$$

Similarly, components of the local stiffness matrix of element 2 can be derived. At this stage, the components of the local stiffness matrix need to be assembled in a matrix that contains 24 rows and 24 columns where local contributions of the components are evaluated. Following Figure 6.6 shows the location convention of the local stiffness matrix.

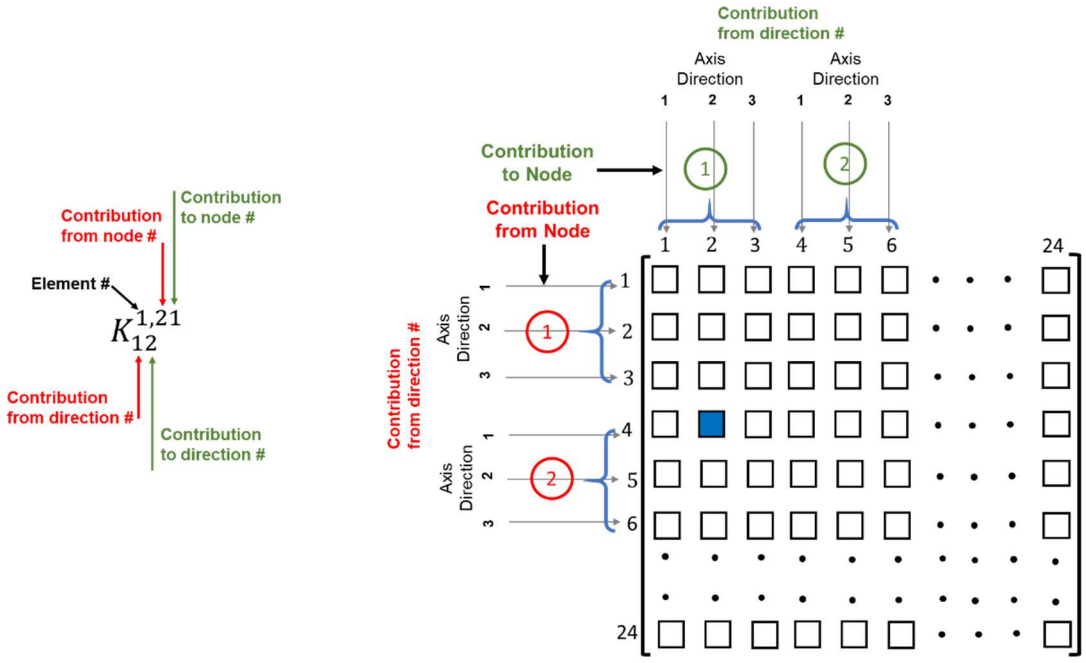

Figure 6.6: Formation of local stiffness matrix of element 1. Left: Number convention of a member of a component matrix. Right: Location convention of a local stiffness matrix.

While assembling the local stiffness matrix from its components, the contributions of a node to itself and other nodes of the element need to be accounted for. Moreover, the contribution This concept is illustrated in Figure 8 and implementation examples are described in Table 6.2. Based on this contribution, each member of each components is placed in the local stiffness matrix. The notation $K_{12}^{1,21}$ in Figure 6.6 indicates that it has a contribution from node 2 and it is contributing to node 1. Therefore, it can be located any at nine positions local stiffness matrix which are [4, 1], [4, 2], [4, 3], [5, 1], [5, 2], [5, 3], [6, 1], [6, 2] and [6, 3]. Now, the contribution from direction 1 and contribution to direction 2 determines the exact location in local stiffness matrix which is [4, 2].

Table 6.2: Assembly of element local stiffness matrix from its components.

Component	Contribution from node	Contribution to node	Contribution from direction	Contribution to direction	Placement in local matrix
$K_{11}^{1,11}$	1	1	1	1	[1, 1]
$K_{11}^{1,12}$	1	2	1	1	[1, 4]
$K_{11}^{1,13}$	1	3	1	1	[1, 7]
$K_{11}^{1,18}$	1	8	1	1	[1, 22]
$K_{12}^{1,11}$	1	1	1	2	[1, 2]
$K_{32}^{1,11}$	1	1	3	2	[3, 2]
$K_{32}^{1,17}$	1	7	3	2	[3, 20]

Similarly, the local stiffness matrix of element 2 can be derived from its stiffness components. Once the local stiffness matrices are determined, the global stiffness matrix can be evaluated its local stiffness parts. The nodes which are not shared by any element, the local stiffness values of those nodes are directly placed in the global stiffness matrix using the placement convention stated above. Moreover, if there is no contribution from one node to another node, the stiffness value is considered to be zero. However, nodes that are shared by the elements, values of global stiffness matrix are evaluated by adding the local stiffness components of shared nodes. In this example, global nodes [2, 4, 6, 8] are shared by both elements. Therefore, respective components of nodes [2, 4, 6, 8] need to be summed up. For example, first component of node 2 (which is a global node 2) of element 1 is located at [1, 4] of local stiffness matrix of element 1. On the other hand, first local node of element 2 is global node 2. Therefore, first nodal component of local stiffness matrix of element 2 needs to be added with the first component of node 2 of element 1 in global stiffness matrix.

$$K\,[1,4] = K_{11}^{1,12} + K_{11}^{2,11}$$

Similarly,

$$K\,[1,5] = K_{11}^{1,13} + K_{11}^{2,12}$$

And so on. Evaluation and assembly of global stiffness matrix is illustrated in Figure 6.7.

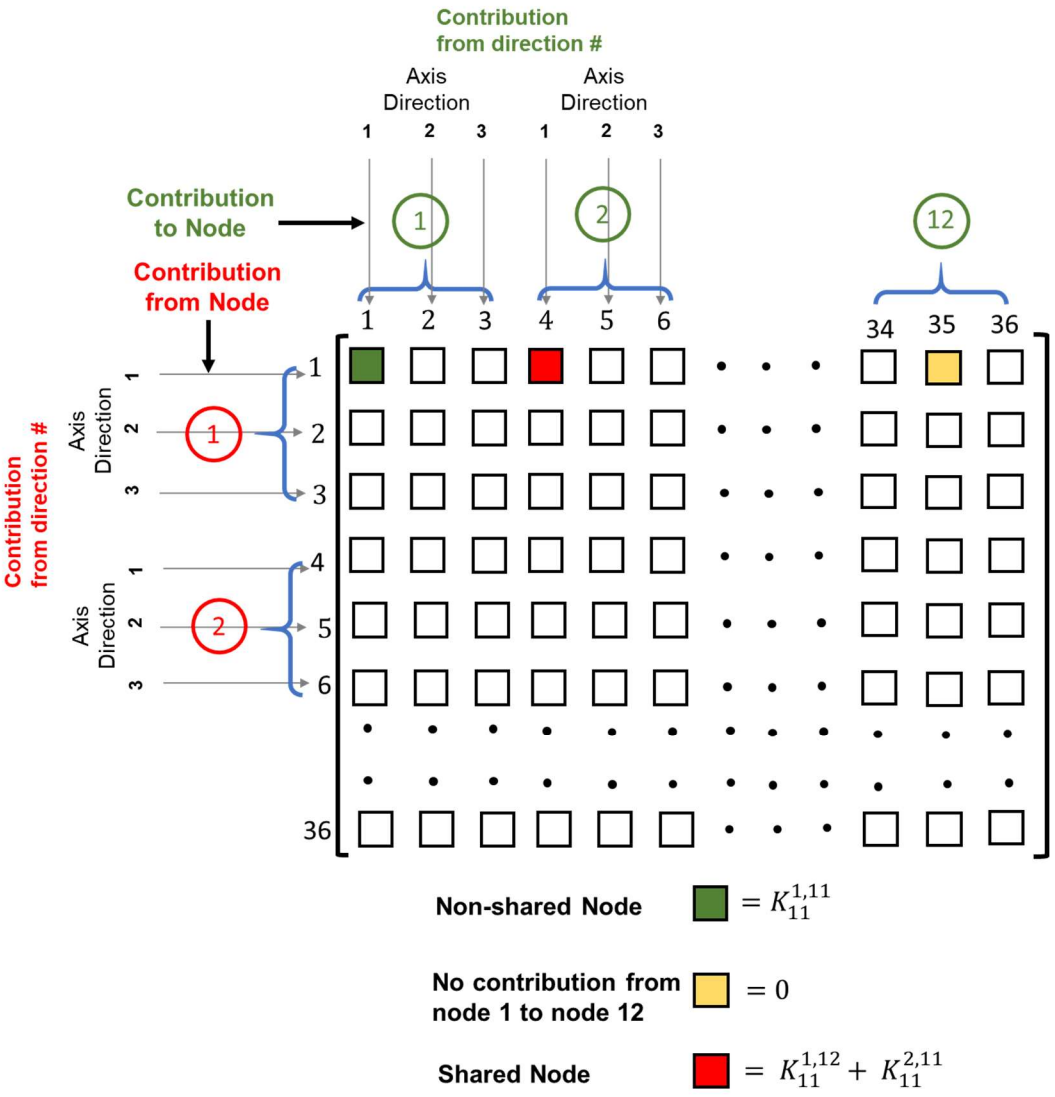

Figure 6.7: Evaluation and assembly of global stiffness matrix from its local stiffness matrix.

6.5 Simulation Setup

Implementation of SEM to solve wave propagation problem requires setting up initial parameters based on the material properties and applied force with specific frequency range. In this study, the geometric dimension of the problem is assumed as 24-

ply composite structure having a dimension of 50 mm X 20 mm X 10 mm. The material properties are assumed as follows,

Density: 1560 kg /m^3

Elasticity matrix: $\mathbb{C} = \begin{bmatrix} 143.8 & 6.2 & 6.2 & 0 & 0 & 0 \\ 6.2 & 13.3 & 6.5 & 0 & 0 & 0 \\ 6.2 & 6.5 & 13.3 & 0 & 0 & 0 \\ 0 & 0 & 0 & 3.4 & 0 & 0 \\ 0 & 0 & 0 & 0 & 5.7 & 0 \\ 0 & 0 & 0 & 0 & 0 & 5.7 \end{bmatrix} GPa$

Order of the Lobatto polynomial: 5 in all directions

Order of the shape function: 5 in all directions

Location of point source: 25 mm X 10 mm X 10 mm

Type of loading: 1 MHz or 5 MHz or 7.5 MHz 5 count tone burst signal with unit amplitude. Example of 1 MHz 5 count tone burst signal is shown in figure 6.8,

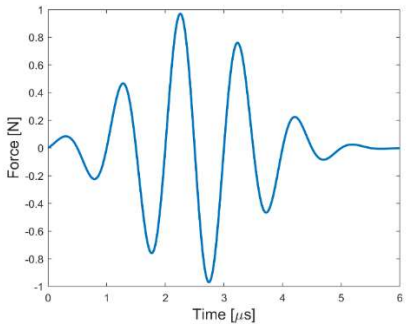

Figure 6.8: 5 count tone burst with central frequency of 1 MHz

6.6 Simulation Results

Discretized area using SEM mesh and the point of time signal application are shown in following figure,

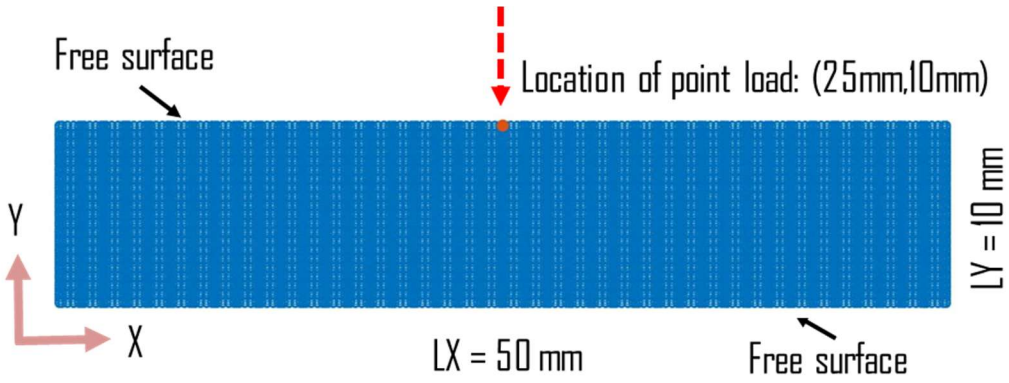

Figure 6.9: Discretized SEM domain with the location of applied point force.

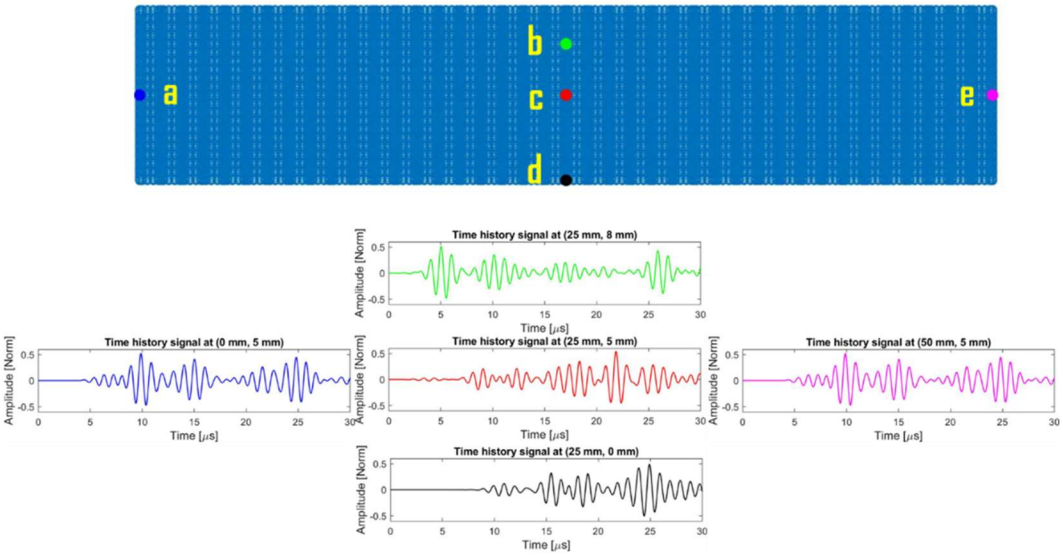

Figure 6.10: (top) Discretized domain of two-layered [0, 90] composite plate with five sensing point distinguished by colors. (bottom five) Time history signals of respective sensing points identified by the colors.

After successful translation of SEM concept into computer codes, various simulations were performed by changing the geometric and simulation parameters. Time history signals are collected at multiple configurations and presented in this work. First, simulation results of a two-layered composite plate while excited with a 1 MHz tone

burst signal are presented. Afterwards, layers are added to the composite plate. Therefore, results with four-layered and eight-layered composite plates are presented.

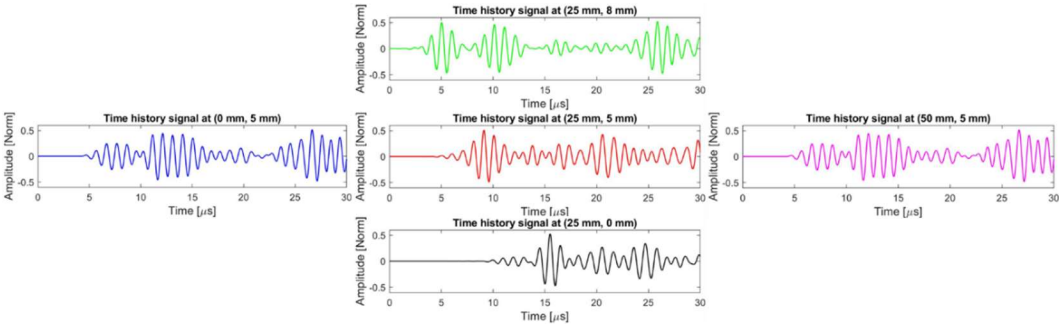

Figure 6.11: Time history signals at the sensing points of a four-layered [0, 90, 0, 90] composite specimen marked by the colors.

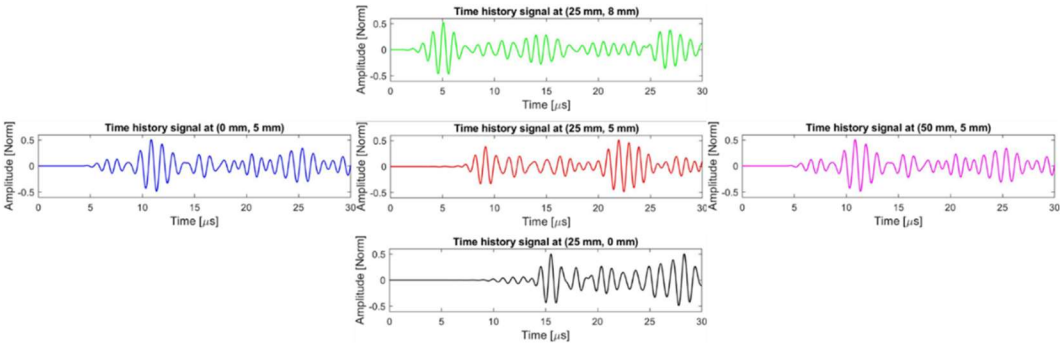

Figure 6.12: Time history signals at the sensing points of eight-layered [0, 90]4 composite specimen marked by the colors.

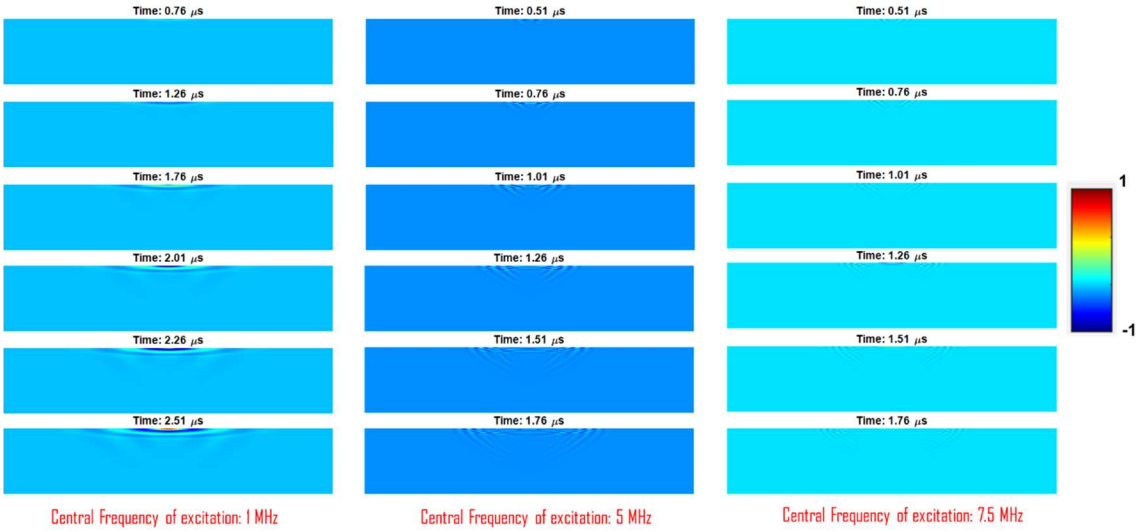

Figure 6.13: Snapshots of wave propagation in 0-deg carbon fiber plates.

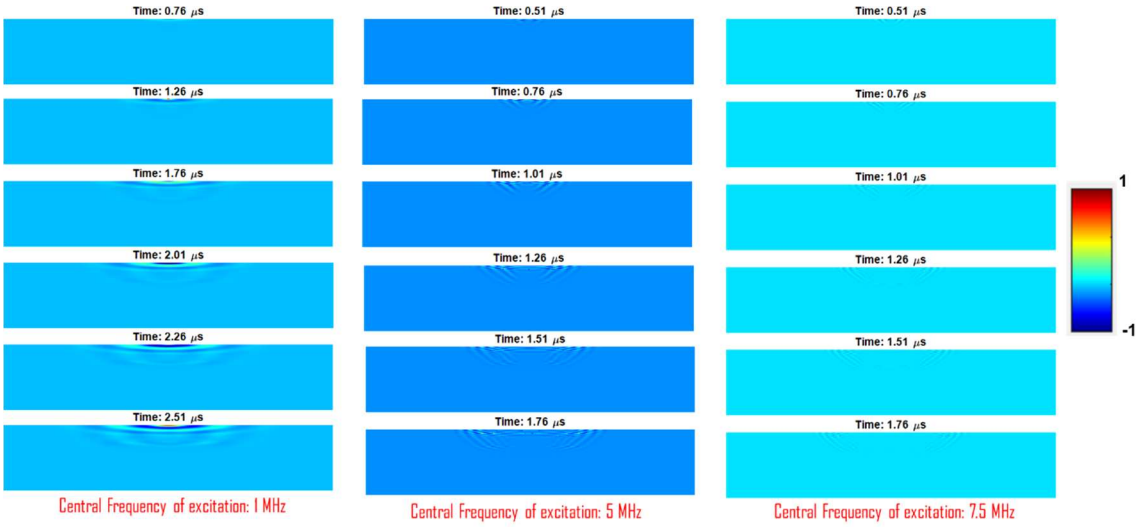

Figure 6.14: Snapshots of wave propagation in [0 90]2 carbon fiber plates.

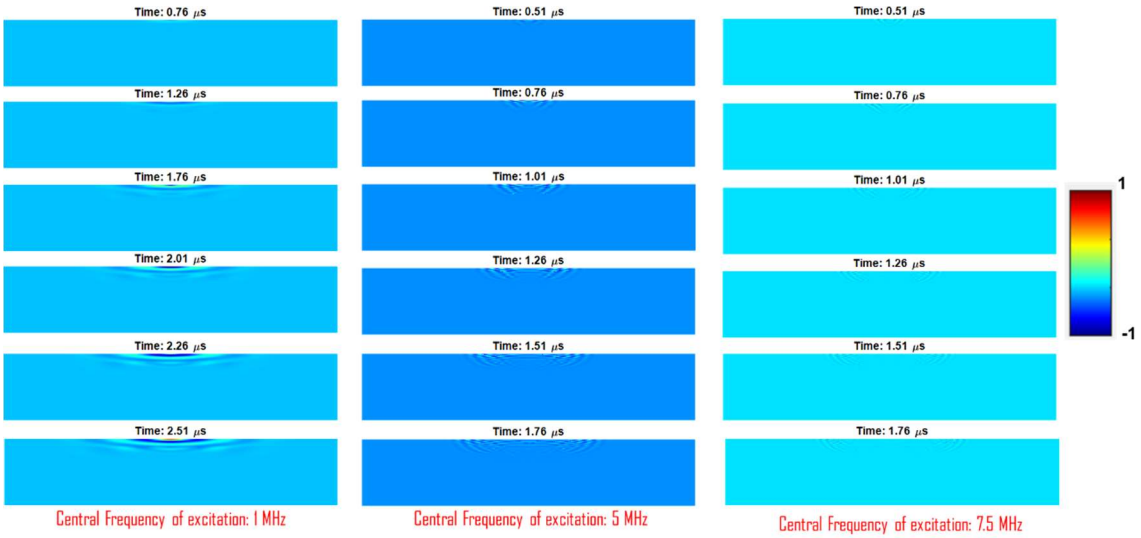

Figure 6.15: Snapshots of wave propagation in $[0\ 90]_4$ carbon fiber plates.

6.7 Experimental Validation

The results obtained by SEM requires experimental validation to prove its effectiveness. However, due to unavailability of 24-layer thick composite plate, an experiment was performed with 1.7 mm plate. The orientation of the carbon fibers was $[0, 90]_4$. This plate was manufactured from Prepreg using hot-press machine available at McNair center of USC. The dimension of this plate was 12 in x 12 in. A center point was identified which was excited by a 5-count tone burst signal with a central frequency of 1 MHz. The experimental setup is shown in Figure 6.16.

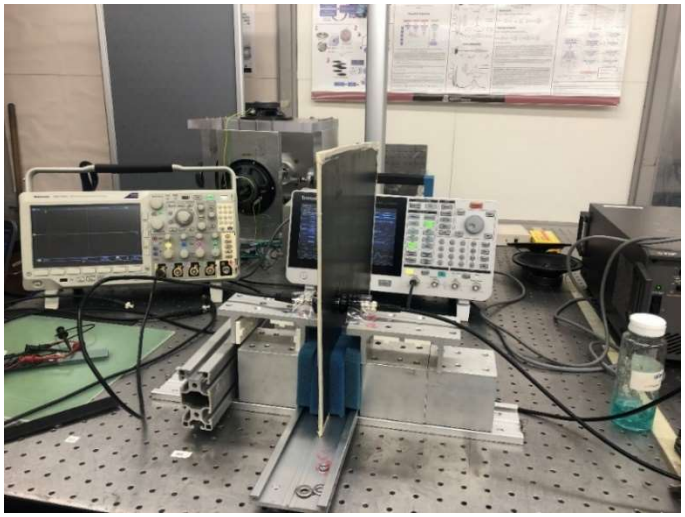

Figure 6.16: Experimental setup to acquire wave propagation signal through a 1.7 mm thick composite plate.

The input amplitude of the tone burst signal was set to 100 VPP. The obtained signal from the 1 MHz contact transducer is shown in Figure 6.17. The input and sensing transducers have 25 mm element diameter.

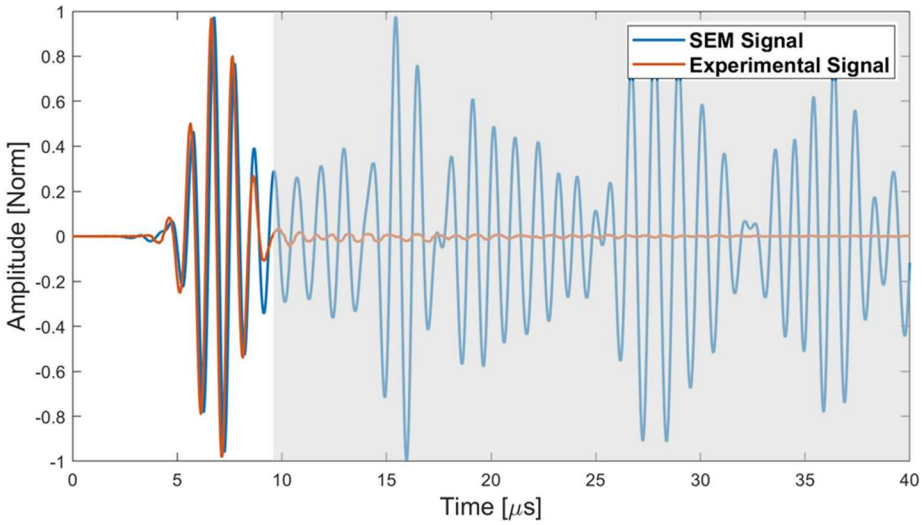

Figure 6.17: Comparison of experimental and SEM simulation results excited with a 5-count tone burst signal with a central frequency of 1 MHz.

In order to validate the effectivity of SEM formulation, a simulation was performed in line with the specification followed for experimental setup. In this simulation the dimension of the plate was considered as 50mm X 1.7mm X 10 mm. The excitation signal of 5 count tone burst with a central frequency of 1 MHz was applied at seven points which were spread at 12.5 mm following a straight line. The output or sensing signal was collected from a single point from the bottom of the plate. The simulation and experimental signal were then superimposed to each other which is shown in Figure 6.17. It can be noted that the SEM simulation result partially followed the experimental results. The possible reasons for the partial matching are as follows:

i. SEM simulation does not consider damping in it which is evident form the SEM results and multiple vibrations of the sensing point is observed. On the other hand, the experimental signal contains damping in it which damped out the later part of the signal. The part of the signal which has large damping effect are colored gray in Figure 6.17.
ii. In SEM simulation, reflecting boundary conditions are not assumed. For this reason, the reflections from the boundary are evident form the SEM signal. However, the experimental plate was large enough to avoid the boundary reflections.
iii. The finite excitation regions in SEM simulations were half of the experimental length of the simulation. Moreover, in experimental setup the excitation was of a circular shape which was absent in SEM configurations. All these contributions could be the reasons for the partial mismatch of the SEM results with the experimental data.

Currently, the SEM code is being developed to adopt the experimental configurations which will simulate the composite structures with considerable accuracy. An adequate extension of the project would be key to develop this code for highly accurate predictions of real time environment.

6.8 Conclusion

The SEM simulation environment has been developed to simulate wave propagation in composite structures. The capability of this software is to simulate high frequency (up to 7.5 MHz) ultrasonic wave. To validate the SEM results, an experiment was performed in a through transmission configuration with a plate of 1.7 mm thick. With a similar configuration, the SEM simulation was also carried out. In both cases, the excitation was applied with a 5-count tone burst signal with a central frequency of 1 MHz. A good agreement of the signal pattern was found for the first part of the signal. Due to the absence of damping coefficients, non-reflecting boundary conditions and similar finite length of the excitation transducers, in the later part of the signal a partial mismatched was observed. A further development on multiple parameters will enhance the capability of the code to match with experimental outcome.

CHAPTER 7

CONCLUSION AND RECOMMENDATIONS

7.1 CONCLUSIONS

One of the limitations of the current ultrasonic NDE technology is the inability to inspect composite substrates with inherent curvature located below attenuative topcoats with thicknesses ranging from 0.15-0.30 inches. Despite the presence of attenuative and aberrative surfaces, many industries such as aerospace, oil and gas, civil, construction etc. rely on ultrasonic NDE to assess structural integrity and evaluate structural health. In this dissertation, a technique is proposed to propagate ultrasound waves through a combination of attenuative and/or aberrative surface and CFRP composite structure. In this technique, two approaches are developed.

In the first approach, two metamaterials are proposed for wave focusing inside thick composite plate. The first metamaterial is proposed to understand and achieve acoustic beam focusing at ultrasonic frequency and keep the structure transparent to the sonic frequencies (<20 kHz). In designing this acoustic metamaterial, a butterfly shaped engineered metamaterial consists of an array of stainless-steel split ring resonators of different sizes embedded in epoxy matrix are explored. It has been shown that this metamaterial is capable of focusing ultrasonic wave at ~37 kHz while remains acoustically transparent below ~20 kHz. By virtue of negative refraction phenomenon, this butterfly metastructure can be utilized as an acoustic lens.

The second metamaterial, a bio-inspired optimized interlock micro-structure, is proposed as an ad-hoc metastructure in-front of conventional NDE transducers. The modal analysis demonstrates that at ~121 kHz, ~123 kHz and ~130 kHz, this metastructure can focus ultrasonic wave inside a 10 mm thick CFRP composite structure. By varying the distance between the metastructure and the CFRP composite plate, the focal point can be adjusted. Further modal analysis at ~267.5 kHz and ~271 kHz reveals that the metastructure is capable of generating Bessel Beam and frequency domain analysis clearly demonstrates long distance wave propagation with negligible attenuation of wave amplitude. Utilizing this capability, an ad-hoc interlock metastructure is placed infront of conventional NDE transducer and found that ultrasonic wave propagates through a combination of attenuative epoxy (Hysol 9394) and 10 mm thick CFRP composite plate.

In the second approach, a computational tool is developed to visualize wave propagation inside a multi-layered (24-ply) 3D composite plate. This tool is developed from scratch utilizing Spectral Element Method due to its higher accuracy and fast convergence. The unique ability of this tool is to simulate wave propagation at a frequency range of 1 MHz to 7.5 MHz, which is not currently available in literature. The mathematical formulation and requirements to implement this concept in computer applications are demonstrated. A computer code is developed to simulate wave propagation. Displacement wave field and time dependent signals are collected at various time stamps. An experimental setup is designed to propagate ultrasonic wave at 1 MHz. A 8-layer 1.7 mm thick composite plate is tested and through transmission wave signals

are collected. The first part of the simulation results has a good agreement with similar part of the experimental result.

7.2 Major Contributions

A. Development of multifunctional butterfly structured metamaterials to focus ultrasonic wave beam at 37k kHz utilizing negative refraction phenomenon
B. Investigation of interlock microstructure metamaterial and determination of of its material properties to achieve wide bandgap and demonstrate near isotropic behavior. Wave trapping and attenuation have been demonstrated using this metastructure.
C. Design of optimized interlock structure to utilize it as an ad-hoc metastructure in front of conventional NDE transducer to focus ultrasonic wave inside thick composite materials.
D. Generation of Bessel Beam using optimized interlock metastructure to achieve long distance wave propagation and utilize this phenomenon to propagate wave through a combination of attenuative Epoxy (Hysol 9394) and CFRP composite material.
E. Development of an NDE computational method from scratch using Spectral Element Method to simulate wave propagation in 3D multilayered composite materials.

7.3 FUTURE RECOMMENDATIONS:

Development of Metastructure

A. Butterfly structured metamaterial cab be further studied to determine suitable constituent materials with the aim of achieving wave focusing and practical realization.
B. Optimized interlock metastructure can be realized using locally available materials. Experimental validation of this PC could implement the idea proposed in this dissertation.

Development of SEM code

A. Application of damping co-efficient and absorbing boundary conditions will improve this code significantly.
B. During temporal solution module, there is a suitable scope of parallel computing which will significantly improve the solution duration.
C. Damage modeling can be introduced in this code with high frequency actuation.

REFERENCES

1. Haar, G.T. and C. Coussios, *High intensity focused ultrasound: physical principles and devices.* (0265-6736 (Print)).
2. Escoffre, J.-M. and A. Bouakaz, *Therapeutic ultrasound*. Vol. 880. 2015: Springer.
3. Szabo, T.L., *Diagnostic ultrasound imaging: inside out*. 2004: Academic Press.
4. Gélat, P., G.t. Haar, and N. Saffari, *A comparison of methods for focusing the field of a HIFU array transducer through human ribs.* Physics in Medicine & Biology, 2014. **59**(12): p. 3139.
5. Fry, F. and J. Barger, *Acoustical properties of the human skull.* The Journal of the Acoustical Society of America, 1978. **63**(5): p. 1576-1590.
6. Eric F. Herzberg, et al., *Estimated Impact of Corrosion on Cost and Availability of DoD Weapon Systems, FY18 Update*. March, 2018.
7. Grendahl, S. and B. Hardisky, *FPI and MPI of Cracks Under Coatings*. 2007, Army Research Laboratory, Aberdeen Proving Ground, MD.
8. Cooney, A. and J.L. Blackshire, *Advanced imaging of hidden damage under aircraft coatings*. Nondestructive Evaluation for Health Monitoring and Diagnostics. Vol. 6179. 2006: SPIE.
9. Ospald, F., et al., *Aeronautics composite material inspection with a terahertz time-domain spectroscopy system.* Optical Engineering, 2013. **53**(3): p. 1-15, 15.
10. Ahmed, R. and S. Banerjee, *Wave Propagation in Metamaterial Using Multiscale Resonators by Creating Local Aniosotropy.* International Journal of Modern Engineering, 2013. **13**(2): p. 51-59.
11. Climente, A., D. Torrent, and J. Sánchez-Dehesa, *Sound focusing by gradient index sonic lenses.* Applied Physics Letters, 2010. **97**(10): p. 104103.
12. Li, Y., et al., *Reflected wavefront manipulation based on ultrathin planar acoustic metasurfaces.* Sci Rep, 2013. **3**: p. 2546.
13. Lin, S.-C.S. and T.J. Huang, *Acoustic mirage in two-dimensional gradient-index phononic crystals.* Journal of Applied Physics, 2009. **106**(5): p. 053529.
14. Torrent, D. and J. Sánchez-Dehesa, *Acoustic metamaterials for new two-dimensional sonic devices.* New Journal of Physics, 2007. **9**(9): p. 323-323.
15. Xie, Y., et al., *Wavefront modulation and subwavelength diffractive acoustics with an acoustic metasurface.* Nat Commun, 2014. **5**: p. 5553.

16. Zhao, J., et al., *Manipulating acoustic wavefront by inhomogeneous impedance and steerable extraordinary reflection.* Sci Rep, 2013. **3**: p. 2537.

17. Zhao, J., et al., *Redirection of sound waves using acoustic metasurface.* Applied Physics Letters, 2013. **103**(15): p. 151604.

18. Zhu, Y.-F., et al., *Dispersionless Manipulation of Reflected Acoustic Wavefront by Subwavelength Corrugated Surface.* Sci Rep, 2015. **5**: p. 10966.

19. Zigoneanu, L.P., Bogdan-Ioan; Starr, Anthony F. ; Cummer, Steven A., *Design and measurements of a broadband two-dimensional acoustic metamaterial with anisotropic effective mass density.* Journal of Applied Physics, 2011. **109**: p. 054906.

20. Srivastava, A., *Negative Refraction, Beam Steering, Mode Switching, and High-pass Filtering in a 1-D Periodic Laminate.* cond-mat.mtrl-sci, 2016. **1**: p. 1-13.

21. Islam, A.B.M.I. and A.D. Kelkar, *Prospects and challenges of nanomaterial engineered prepregs for improving interlaminar properties of laminated composites—a review.* MRS Communications, 2017. **7**(2): p. 102-108.

22. Fietz, C., Y. Urzhumov, and G. Shvets, *Complex k band diagrams of 3D metamaterial/photonic crystals.* Optics express, 2011. **19**(20): p. 19027-19041.

23. Park, G., et al., *Tunable Multifunctional Thermal Metamaterials: Manipulation of Local Heat Flux via Assembly of Unit-Cell Thermal Shifters.* Scientific Reports, 2017. **7**(1): p. 41000.

24. Xu, Z., et al., *A flat acoustic lens to generate a Bessel-like beam.* Ultrasonics, 2017. **80**: p. 66-71.

25. Kaina, N., et al., *Negative refractive index and acoustic superlens from multiple scattering in single negative metamaterials.* Nature, 2015. **525**(7567): p. 77-81.

26. Sukhovich, A., et al., *Experimental and theoretical evidence for subwavelength imaging in phononic crystals.* Phys Rev Lett, 2009. **102**(15): p. 154301.

27. Tsukioka, S., et al., *Development of an Acoustic Lens for an Imaging Sonar for Autonomous Underwater Vehicle "Urashima" and Experimentation in a Water Tank.* Japanese Journal of Applied Physics, 2002. **41**(1): p. 3970–3973.

28. SATO, Y., et al., *Design of an Absolutely Aplanatic Acoustic Lens.* Japanese Journal of Applied Physics, 2007. **46**(7B): p. 4982-4989.

29. Li, J. and C.T. Chan, *Double-negative acoustic metamaterial.* Phys Rev E Stat Nonlin Soft Matter Phys, 2004. **70**(5 Pt 2): p. 055602.

30. Lan, J., et al., *Manipulation of acoustic wavefront by gradient metasurface based on Helmholtz Resonators.* Scientific Reports, 2017. **7**: p. 10587.

31. Tran, Q.D., et al., *Shape and topology optimization of acoustic lens system using phase field method.* Structural and Multidisciplinary Optimization, 2017. **56**(3): p. 713-729.

32. Jahdali , R.A. and Y. Wu, *High transmission acoustic focusing by impedance-matched acoustic meta surface.* APPLIED PHYSICS LETTERS, 2016. **108**(3): p. 031902.

33. Park, J.J., et al., *Acoustic superlens using membrane-based metamaterials.* Applied Physics Letters, 2015. **106**(5): p. 051901.

34. Taubner, T., et al., *Near-field microscopy through a SiC superlens.* Science, 2006. **313**(5793): p. 1595.

35. Chadi, D.J. and M.L. Cohen, *Special Points in the Brillouin Zone.* Physical Review B, 1973. **8**(12): p. 5747-5753.

36. Khelif, A., et al., *Complete band gaps in two-dimensional phononic crystal slabs.* Phys Rev E Stat Nonlin Soft Matter Phys, 2006. **74**(4 Pt 2): p. 046610.

37. Wu, T.-T., Z.-G. Huang, and S. Lin, *Surface and bulk acoustic waves in two-dimensional phononic crystal consisting of materials with general anisotropy.* Physical Review B, 2004. **69**(9): p. 094301.

38. Giurgiutiu, V., *Structural Health Monitoring*. 2nd Ed. ed. July 2014: Elsevier AP.

39. Fleck, N., V. Deshpande, and M. Ashby, *Micro-architectured materials: past, present and future.* Proceedings of the Royal Society A: Mathematical, Physical and Engineering Sciences, 2010. **466**(2121): p. 2495-2516.

40. Tavaf, V., et al. *Effect of multiscale precursor damage on wave propagation through modulated constitutive properties of composite materials*. in *Health Monitoring of Structural and Biological Systems XII*. 2018. International Society for Optics and Photonics.

41. Tavaf, V., et al., *Quantification of material degradation and its behavior of elastodynamic Green's function for computational wave field modeling in composites.* Materials Today Communications, 2018. **17**: p. 402-412.

42. Ashby, M., *On the engineering properties of materials, Overview No. 80.* Acta Metall, 1989. **37**(5): p. 1273-1293.

43. Kooistra, G.W., V.S. Deshpande, and H.N. Wadley, *Compressive behavior of age hardenable tetrahedral lattice truss structures made from aluminium.* Acta Materialia, 2004. **52**(14): p. 4229-4237.

44. Tavaf, V., M. Saadatzi, and S. Banerjee, *Quantification of degraded constitutive coefficients of composites in the presence of distributed defects.* Journal of Composite Materials, 2019. **53**.

45. AHMED, H., et al., *Entropy-Based Damage Evaluation of Composite Structure and Its Application to Structural Health Management.* Structural Health Monitoring 2019, 2019.

46. Ahmed, R., F. Mir, and S. Banerjee, *A review on energy harvesting approaches for renewable energies from ambient vibrations and acoustic waves using piezoelectricity.* Smart Materials and Structures, 2017. **26**(8): p. 085031.

47. Fariha, M., et al. *The possibility of harvesting electrical energy from industrial noise barriers using meta-wall bricks*. in *Proc.SPIE*. 2018.

48. Mohammadsadegh, S., et al. *Modeling of a 3D acoustoelastic metamaterial energy harvester*. in *Proc.SPIE*. 2018.

49. Saadatzi, M., et al., *Modeling and Fabrication of a Multi-Axial Piezoelectric Energy Harvester Based on a Metamaterial-Inspired Structure.* IEEE Sensors Journal, 2018. **18**(22): p. 9410-9419.

50. Mir, F., et al., *Study of split ring metamaterial with simultaneous wave guiding and energy harvesting capability*. SPIE Smart Structures + Nondestructive Evaluation. Vol. 10967. 2019: SPIE.

51. Saadatzi, M., et al., *AEVE 3D: Acousto Electrodynamic 3-Dimensional Vibration Exciter for Engineering Testing.* IEEE/ASME Transactions on Mechatronics, 2018.

52. Saadatzi, M., et al. *An electro-dynamic 3-dimensional vibration test bed for engineering testing*. in *Industrial and Commercial Applications of Smart Structures Technologies 2017*. 2017. International Society for Optics and Photonics.

53. Mir, F., et al. *The possibility of harvesting electrical energy from industrial noise barriers using meta-wall bricks*. in *Sensors and Smart Structures Technologies for Civil, Mechanical, and Aerospace Systems 2018*. 2018. International Society for Optics and Photonics.

54. Whitmore, N., et al. *Full wavefield modeling with vector reflectivity*. in *82nd EAGE Annual Conference & Exhibition*. 2020. European Association of Geoscientists & Engineers.

55. Sun, Y. and E. Verschuur, *Full wavefield modeling using rigorous one-way propagation, reflection and transmission operators*, in *SEG Technical Program Expanded Abstracts 2020*. 2020, Society of Exploration Geophysicists. p. 2694-2698.

56. Murray, G.J. and F. Gandhi, *Auxetic honeycombs with lossy polymeric infills for high damping structural materials.* Journal of Intelligent Material Systems and Structures, 2013. **24**(9): p. 1090-1104.

57. Estrin, Y., A.V. Dyskin, and E. Pasternak, *Topological interlocking as a material design concept.* Materials Science and Engineering: C, 2011. **31**(6): p. 1189-1194.

58. Kushwaha, M.S., et al., *Acoustic band structure of periodic elastic composites.* Physical Review Letters, 1993. **71**(13): p. 2022-2025.

59. Fugen, W., L. Zhengyou, and L. Youyan, *Acoustic band gaps in 2D liquid phononic crystals of rectangular structure.* Journal of Physics D: Applied Physics, 2002. **35**(2): p. 162.

60. Khelif, A., et al., *Trapping and guiding of acoustic waves by defect modes in a full-band-gap ultrasonic crystal.* Physical Review B, 2003. **68**(21): p. 214301.

61. Ahmed, H., et al., *Multifunction acoustic modulation by a multi-mode acoustic metamaterial architecture.* Journal of Physics Communications, 2018. **2**(11): p. 115001.

62. Indaleeb, M.M., et al., *Deaf band based engineered Dirac cone in a periodic acoustic metamaterial: A numerical and experimental study.* Physical Review B, 2019. **99**(2).

63. Iorsh, I.V., et al., *Hyperbolic metamaterials based on multilayer graphene structures.* Physical Review B, 2013. **87**(7): p. 075416.

64. Indaleeb, M., et al., *Dirac-like cone modulation for phononic crystals using deaf band*. SPIE Smart Structures + Nondestructive Evaluation. Vol. 10972. 2019: SPIE.

65. Park, J., et al., *Determination of effective mass density and modulus for resonant metamaterials.* The Journal of the Acoustical Society of America, 2012. **132**(4): p. 2793-2799.

66. Chen, L.-S., C.-H. Kuo, and Z. Ye, *Acoustic imaging and collimating by slabs of sonic crystalsmade from arrays of rigid cylinders in air.* Applied Physics Letters, 2004. **85**(6): p. 1072-1074.

67. Ahmed, H., R. Ahmed, and S. Banerjee, *Butterfly metamaterial for acoustic holographic imaging through superlensing capability (Conference Presentation)*. SPIE Smart Structures and Materials + Nondestructive Evaluation and Health Monitoring. Vol. 10600. 2018: SPIE.

68. Sukhovich, A., L. Jing, and J.H. Page, *Negative refraction and focusing of ultrasound in two-dimensional phononic crystals.* Physical Review B, 2008. **77**(1): p. 014301.

69. Mustahseen, I., A. Hossain, and B. Sourav. *Investigation on multi-occurrence of Dirac cone and exceptional ring (Conference Presentation)*. in *Proc.SPIE*. 2018.

70. García-Chocano, V.M., J. Christensen, and J. Sánchez-Dehesa, *Negative refraction and energy funneling by hyperbolic materials: An experimental demonstration in acoustics.* Physical review letters, 2014. **112**(14): p. 144301.

71. Mills-Dadson, B., et al., *Monitoring friction related surface degradation using acoustic emission technique*. SPIE Smart Structures and Materials + Nondestructive Evaluation and Health Monitoring. Vol. 8694. 2013: SPIE. 7.

72. Saadatzi, M., et al. *Development of a PVDF Based Artificial Basilar Membrane*. in *Bioinspiration, Biomimetics, and Bioreplication VIII*. 2018. International Society for Optics and Photonics.

73. Saadatzi, M., et al., *Modeling and Fabrication of a Multi-axial Piezoelectric Energy Harvester based on a Metamaterial-inspired Structure.* IEEE Sensors Journal, 2018.

74. Saadatzi, M., et al. *Modeling of a 3D acoustoelastic metamaterial energy harvester*. in *Active and Passive Smart Structures and Integrated Systems XII*. 2018. International Society for Optics and Photonics.

75. Fatima, et al., *First-principles study of electron dynamics with explicit treatment of momentum dispersion on Si nanowires along different directions.* Molecular Physics, 2018: p. 1-10.

76. Fatima, u., et al., *Time-resolved Optical Properties of SiNW Oriented in <211> Crystallographic Direction.* MRS Advances, 2019: p. 1-6.

77. McCall, S., et al., *Microwave propagation in two-dimensional dielectric lattices.* Physical review letters, 1991. **67**(15): p. 2017.

78. Khelif, A., et al., *Guiding and bending of acoustic waves in highly confined phononic crystal waveguides.* Applied Physics Letters, 2004. **84**(22): p. 4400-4402.

79. Li, X. and Z. Liu, *Coupling of cavity modes and guiding modes in two-dimensional phononic crystals.* Solid state communications, 2005. **133**(6): p. 397-402.

80. Haldar, S., T. Sain, and S. Ghosh, *A novel high symmetry interlocking micro-architecture design for polymer composites with improved mechanical properties.* International Journal of Solids and Structures, 2017. **124**: p. 161-175.

81. Balabadhruni, M., *STRENGTH OPTIMIZATION OF A HIGH SYMMETRY INTERLOCKING MICRO-ARCHITECTURE POLYMER COMPOSITE*. 2019, MS Report, Michigan Technological University.

82. Prather, D.W., et al., *Photonic crystals.* Theory, Aplications and Fabrication, 2009.

83. Ahmed, H., et al., *Investigation of wave trapping and attenuation phenomenon for a high symmetry interlocking micro-structure composite metamaterial*. SPIE Smart Structures + Nondestructive Evaluation. Vol. 10973. 2019: SPIE.

84. Garcés-Chávez, V., et al., *Simultaneous micromanipulation in multiple planes using a self-reconstructing light beam.* Nature, 2002. **419**(6903): p. 145-147.

85. McGloin, D. and K. Dholakia, *Bessel beams: Diffraction in a new light.* Contemporary Physics, 2005. **46**(1): p. 15-28.

86. Durnin, J., J.J. Miceli, and J.H. Eberly, *Diffraction-free beams.* Physical Review Letters, 1987. **58**(15): p. 1499-1501.

87. Durnin, J., *Exact solutions for nondiffracting beams. I. The scalar theory.* Journal of the Optical Society of America A, 1987. **4**(4): p. 651-654.

88. Li, X., et al., *Catenary nanostructures as compact Bessel beam generators.* Scientific Reports, 2016. **6**(1): p. 20524.

89. Knyazev, B.A., et al., *Generation of Terahertz Surface Plasmon Polaritons Using Nondiffractive Bessel Beams with Orbital Angular Momentum.* Physical Review Letters, 2015. **115**(16): p. 163901.

90. Chen, J., et al., *Indefinite Plasmonic Beam Engineering by In-plane Holography.* Scientific Reports, 2016. **6**(1): p. 28926.

91. Bhuyan, M.K., et al., *High aspect ratio taper-free microchannel fabrication using femtosecond Bessel beams.* Opt. Express. **18**(2): p. 566--574.

92. Kim, J.-Y., *Models for wave propagation in two-dimensional random composites: A comparative study.* The Journal of the Acoustical Society of America, 2010. **127**(4): p. 2201-2209.

93. Soares, D. and L. Godinho, *An Overview of Recent Advances in the Iterative Analysis of Coupled Models for Wave Propagation.* Journal of Applied Mathematics, 2014. **2014**: p. 1-21.

94. Ahmed, H., et al., *Investigation and development of friction stir welding process for unreinforced polyphenylene sulfide and reinforced polyetheretherketone.* Journal of Thermoplastic Composite Materials, 2018: p. 089270571878567.

95. Mohammad Sadegh, S., et al. *RUSH: Realtime ultrasonic scanning using submergible hydraulic robotic arms for mechanical properties testing*. in *Proc.SPIE*. 2019.

96. Li, Z.X., T.H.T. Chan, and J.M. Ko, *Fatigue analysis and life prediction of bridges with structural health monitoring data — Part I: methodology and strategy.* International Journal of Fatigue, 2001. **23**(1): p. 45-53.

97. Tanner, N.A., et al., *Structural Health Monitoring Using Modular Wireless Sensors.* Journal of Intelligent Material Systems and Structures, 2003. **14**(1): p. 43-56.

98. Vos, P.E.J., S.J. Sherwin, and R.M. Kirby, *From h to p efficiently: Implementing finite and spectral/hp element methods to achieve optimal performance for low- and high-order discretisations.* Journal of Computational Physics, 2010. **229**(13): p. 5161-5181.

99. Biswas, R., K.D. Devine, and J.E. Flaherty, *Parallel, adaptive finite element methods for conservation laws.* Applied Numerical Mathematics, 1994. **14**(1): p. 255-283.

100. Rønquist, E.M. and A.T. Patera, *Spectral element multigrid. I. Formulation and numerical results.* Journal of Scientific Computing, 1987. **2**(4): p. 389-406.

101. Patera, A.T., *A Spectral Element Method for Fluid Dynamics: Laminar Flow in a Channel Expansion.* Journal of Computational Physics, 1984. **54**: p. 468-488.

102. Seriani, G. and S.P. Oliveira, *Dispersion analysis of spectral element methods for elastic wave propagation.* Wave Motion, 2008. **45**(6): p. 729-744.

103. Proot, M.M.J. and M.I. Gerritsma, *Application of the least-squares spectral element method using Chebyshev polynomials to solve the incompressible Navier-Stokes equations.* Numerical Algorithms, 2005. **38**(1): p. 155-172.

104. Ostachowicz, W., et al., *Guided Waves in Structures for SHM The time domain Spectral Element Method*. 2012, A John Wiley & Sons. p. 46-92.

105. Tromp, J., D. Komatitsch, and Q. Liu, *Spectral-element and adjoint methods in seismology.* Communications in Computational Physics, 2008. **3**(1): p. 1-32.

106. Prakash, C. and S. Patankar, *A control volume-based finite-element method for solving the Navier-Stokes equations using equal-order velocity-pressure interpolation.* Numerical Heat Transfer, 1985. **8**(3): p. 259-280.

107. Żak, A. and M. Krawczuk, *Certain numerical issues of wave propagation modelling in rods by the Spectral Finite Element Method.* Finite Elements in Analysis and Design, 2011. **47**(9): p. 1036-1046.

108. Park, I. and U. Lee, *Dynamic analysis of smart composite beams by using the frequency-domain spectral element method.* Journal of Mechanical Science and Technology, 2012. **26**(8): p. 2511-2521.

109. Kudela, P., et al., *Modelling of wave propagation in composite plates using the time domain spectral element method.* Journal of Sound and Vibration, 2007. **302**(4-5): p. 728-745.

110. Kim, Y., S. Ha, and F.-K. Chang, *Time-domain spectral element method for built-in piezoelectric-actuator-induced lamb wave propagation analysis.* AIAA journal, 2008. **46**(3): p. 591-600.

111. Bottero, A., et al., *An axisymmetric time-domain spectral-element method for full-wave simulations: Application to ocean acoustics.* The Journal of the Acoustical Society of America, 2016. **140**(5): p. 3520-3530.

112. Konovalov, D., et al., *The Implementation of Spectral Element Method in a CAE System for the Solution of Elasticity Problems on Hybrid Curvilinear Meshes.* Modelling and Simulation in Engineering, 2017. **2017**: p. 1797561.

113. Pozrikidis, C., *Introduction to finite and spectral element methods using MATLAB*. 2005: CRC Press.